Unveiling the Roles of Defects in Photovoltaic Materials through Multiscale Modeling

Yijun Tong

A dissertation
submitted in partial fulfillment of the
requirements for the degree of

Doctor of Philosophy

University of Washington

2025

Reading Committee:

Scott T. Dunham, Chair

M.P. Anantram

Karl Böhringer

Program Authorized to Offer Degree:
Electrical and Computer Engineering

University of Washington

Abstract

Unveiling the Roles of Defects in Photovoltaic Materials through Multiscale Modeling

Yijun Tong

Chair of the Supervisory Committee:
Scott T. Dunham
Electrical and Computer Engineering

This dissertation develops an integrated multiscale modeling framework for photovoltaic systems, encompassing halide perovskites, cadmium telluride (CdTe), and cadmium selenide (CdSe)–based absorbers. By coupling first-principles density functional theory (DFT) with continuum-scale device simulations, the approach enables quantitative prediction of key electronic and optical properties, as well as the performance limits of complete solar cell architectures. Atomistic DFT calculations provide accurate defect energetics, charge transition levels, and carrier capture coefficients, which are seamlessly incorporated into drift–diffusion device models to resolve carrier transport, recombination, and light–matter interactions under realistic operating conditions. This multiscale methodology allows for systematic evaluation of performance bottlenecks—such as radiative vs. nonradiative loss pathways and loss of open-circuit voltage due to potential fluctuations—and supports the targeted optimization of materials and device structures. The resulting predictive capability offers a transferable framework for guiding experimental design and accelerating the development of next-generation high-efficiency, stable photovoltaic technologies.

TABLE OF CONTENTS

Page

LIST OF FIGURES

LIST OF TABLES

ACKNOWLEDGMENTS

I am deeply grateful to my research advisor and committee chair, Prof. Scott Dunham, for his invaluable patience, insightful feedback, and steadfast guidance throughout this journey. I also extend my sincere thanks to my reading committee members, Prof. M.P. Anantram and Prof. Karl Böhringer, for generously sharing their expertise and providing thoughtful perspectives that strengthened this work.

This research was made possible through the generous support of the U.S. Department of Energy, NSF MRSEC, and the Hyak supercomputer system at the University of Washington. Their resources and funding provided the foundation for the computational and analytical efforts undertaken in this dissertation.

I wish to express my heartfelt appreciation to my office mates, whose research assistance, editing help, and moral support have been invaluable both in and beyond the laboratory. Their encouragement and camaraderie have been an essential part of this experience.

Finally, I am most indebted to my family—especially my parents—for their unwavering belief in me. Their constant love, patience, and encouragement have been my greatest source of strength, sustaining both my spirit and motivation through every stage of this process.

Chapter 1

INTRODUCTION

The solar cell market has expanded rapidly in recent years, driven by projected energy demands and global efforts to achieve net-zero carbon emissions. While conventional photovoltaic technologies such as silicon (Si) and gallium arsenide (GaAs) solar cells achieve high power conversion efficiencies, they require high-quality crystalline materials, which substantially increase production costs. In contrast, thin-film solar cells offer higher defect tolerance, a lower temperature coefficient, tunable bandgaps, a high absorption coefficient, and reduced material costs. Among thin-film photovoltaic technologies, halide perovskites and cadmium telluride (CdTe) have emerged as two of the most promising absorber materials, owing to their high power conversion efficiencies, tunable optoelectronic properties, and compatibility with low-cost, scalable manufacturing processes.

Despite significant advances in thin-film photovoltaic research, device performance remains well below the theoretical Shockley–Queisser limit. Carrier lifetimes are frequently constrained by defect-assisted Shockley–Read–Hall (SRH) recombination, as well as recombination at grain boundaries and interfaces, all of which degrade overall efficiency. Establishing a detailed understanding of how manufacturing processes influence these recombination pathways requires rigorous understanding of materials and device modeling. Multiscale simulations provide critical insights into the coupling between material properties, device architecture, and operational performance, thereby enabling the systematic optimization of thin-film solar cell technologies.

For the systems examined in this work—namely halide perovskites and cadmium telluride (CdTe)—the understanding of material properties, particularly defect physics, and the availability of comprehensive device models remain incomplete. This gap arises in part

from the complexity of intrinsic point defects and extrinsic dopants in compound semiconductors. As a result, many existing device models rely on simplified parameters such as effective carrier lifetime and equilibrium carrier density, which fail to capture the detailed links between material properties and device behavior. In this dissertation, multiscale modeling is employed by coupling first-principles *ab initio* quantum-mechanical calculations with device-level simulations. This integrated approach enables quantitative evaluation of how specific material characteristics and alternative device architectures influence photovoltaic performance, thereby guiding strategies for device optimization.

In Chapter 2, the background on selected photovoltaic materials is presented, followed by the methodology employed in this work, including density functional theory (DFT), defect modeling, finite-size charged cell correction and device simulation. Advanced semiconductor concepts including defect chemical reaction and detailed balance of multilevel defect recombination are also introduced.

In Chapter 3, intrinsic defects in inorganic halide perovskites are systematically investigated using first-principles calculations. Defect formation energies and thermodynamic transition levels are evaluated to identify potential deep-level traps. Nonradiative recombination rates are then computed using a theoretical framework based on Fermi's golden rule, enabling verification of whether these deep-level defects act as strong carrier capture centers. The self-doping phenomenon is also examined using information extracted from the calculated profiles of defect formation energy as a function of the Fermi level. Futhermore, the role of interface passivation is investigated in 3D-2D structured perovskite.

In Chapter 4, density functional theory (DFT) calculations are integrated with device simulations to develop a predictive TCAD model for CdTe/CdSeTe solar cells. First, DFT is employed to determine the formation energies and diffusion barriers of dominant defects in CdTe/CdSeTe. Using a first-principles–based approach, defect capture cross sections are estimated and combined with calculated defect profiles and trap energy levels to parameterize a Shockley–Read–Hall (SRH) recombination model. This parameterized SRH model

is then implemented into a device simulator to predict carrier lifetimes and overall device performance. Through this coupling of atomistic and continuum modeling, a robust TCAD framework is established to guide performance optimization of CdTe/CdSeTe solar cells. Furthermore, the impact of potential fluctuation on the open-circuit voltage deficiency in this system is investigated through the built and well-calibrated TCAD model.

In Chapter 5, selenium vacancies in CdSe are investigated using the developed theoretical framework, providing insights into experimental observations obtained by our collaborators. DFT is employed to identify the metastable configuration of the neutral selenium vacancy through a constructed configuration–coordinate diagram. The relevant parameters extracted from this diagram are then incorporated into continuum simulations based on a multilevel trap model, enabling quantitative analysis of the impact of selenium vacancies on carrier dynamics.

Chapter 2

BACKGROUND

2.1 Photovoltaic Materials in this Study

2.1.1 CdTe/CdSeTe

CdTe is a direct bandgap semiconductor characterized by its high absorption coefficient, capable of absorbing approximately 92% of visible light within a film thickness of merely 1μm [57]. Recent advancements have pushed the power conversion efficiency of CdTe-based devices to 22.3% [60]. Following decades of research and development, p-type polycrystalline CdTe systems treated with $CdCl_2$ have become the industry standard. Additionally, alloying CdTe with selenium (Se) forms the ternary compound cadmium selenium telluride (CdSeTe), which possesses a reduced and compositionally tunable direct bandgap [65]. By varying the Se content, the optical bandgap of CdSeTe can be engineered to optimize device performance. Notably, introducing a front-side graded CdSeTe region in CdTe solar cells has been shown to enhance the short-circuit current density (J_{sc}) by improving the absorption of long-wavelength photons.

P-type doping of CdTe and CdSeTe can be realized using Group V elements such as phosphorus (P), arsenic (As), and antimony (Sb) and copper doping, which substitute on Te/Se sites and contribute to increased hole concentrations and enhanced photovoltaic efficiency [37, 62]. However, the interaction between these extrinsic dopants and intrinsic point defects remains insufficiently understood, particularly as the selenium content varies in CdSeTe alloys. First-principles calculations based on density functional theory (DFT) provide a powerful framework for elucidating these complex defect–dopant interactions at the atomic scale [10]. In parallel, the development of a robust TCAD (Technology Computer-Aided Design) model is essential for simulating and optimizing device-level performance. This

thesis integrates both DFT and TCAD approaches to investigate the material properties and device behavior of CdTe/CdSeTe systems in a comprehensive manner.

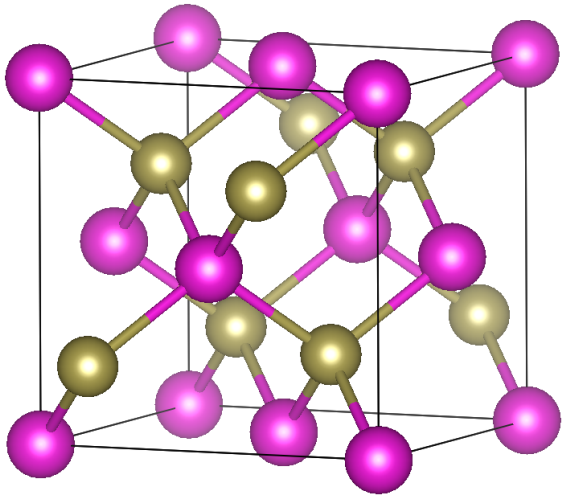

Figure 2.1: Unit cell of zinc blende CdTe

2.1.2 CdSe

With a bandgap of approximately 1.7 eV, CdSe is a near-ideal candidate for the high-bandgap top junction in tandem solar cell architectures. However, despite its favorable optical properties, CdSe-based solar cells have not yet achieved the performance levels required for tandem integration, largely due to limitations in minority carrier lifetime and elevated recombination losses [52, 101]. In photovoltaic applications, CdSe typically crystallizes in the hexagonal wurtzite phase when synthesized under moderate-temperature and low-pressure conditions, distinct from the cubic zincblende phase commonly stabilized in epitaxial or nanocrystalline forms. This differentiates it both structurally and electronically from the zincblende-phase CdTe used in mainstream thin-film solar cells. Renewed interest in CdSe has emerged in the context of all-thin-film tandems, where understanding and optimizing defect properties remain critical barriers to practical deployment.

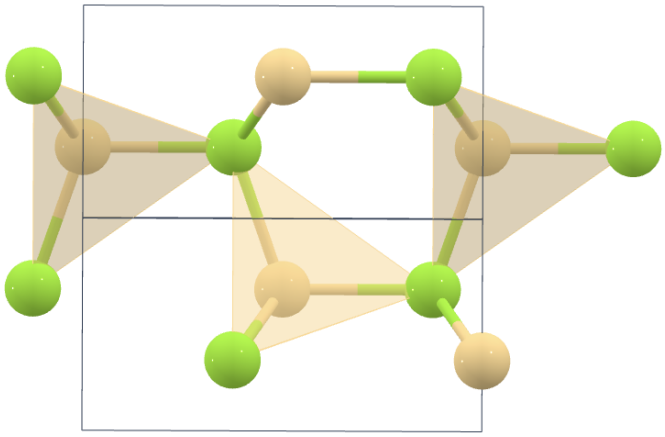

Figure 2.2: Unit cell of wurtzite CdSe

2.1.3 Perovskites

Hybrid organic–inorganic halide perovskites with the general formula ABX_3, exemplified by methylammonium (MA, CH_3NH_3) lead/tin iodide ($MAPbI_3$/$MASnI_3$), and often alloyed with formamidinium (FA, $CH[NH_2]_2$) and/or cesium (Cs) at the A-site, have garnered significant interest in recent years for photovoltaic (PV) applications [85]. This interest stems from their high power conversion efficiencies (exceeding 25%) [32] and compatibility with low-cost solution-based fabrication techniques [6]. Beyond photovoltaics, perovskite materials also show promise in light-emitting diodes (LEDs) [55] and photodetectors [86]. Nevertheless, the widespread application of hybrid organic–inorganic perovskites is limited by their susceptibility to degradation under environmental conditions such as humidity and oxygen exposure [12]. To address these stability concerns, all-inorganic halide perovskites—such as $CsPbI_3$ and $CsSnI_3$—have emerged as promising alternatives, offering comparable optoelectronic properties alongside improved environmental robustness [87].

A thorough understanding of native defects and impurities is essential for controlling doping levels and carrier lifetimes in halide perovskite-based devices. First-principles studies based on density functional theory (DFT) have been widely employed to investigate the

properties of native defects in these materials. However, there remains no standardized computational protocol that consistently yields reliable results and conclusions [99, 107]. Prior studies emphasize the importance of incorporating spin–orbital coupling (SOC) effects for accurately predicting key material properties such as bandgap values [63]. Nevertheless, the inclusion of SOC within hybrid functional calculations imposes significant computational costs, often restricting defect simulations to relatively small supercells. In addition, finite-size corrections for charged defects are sometimes omitted without explicit justification [63, 100]. Therefore, there is a pressing need for a reliable and computationally efficient DFT framework that can accurately reproduce experimental bandgaps while remaining suitable for large-scale defect studies.

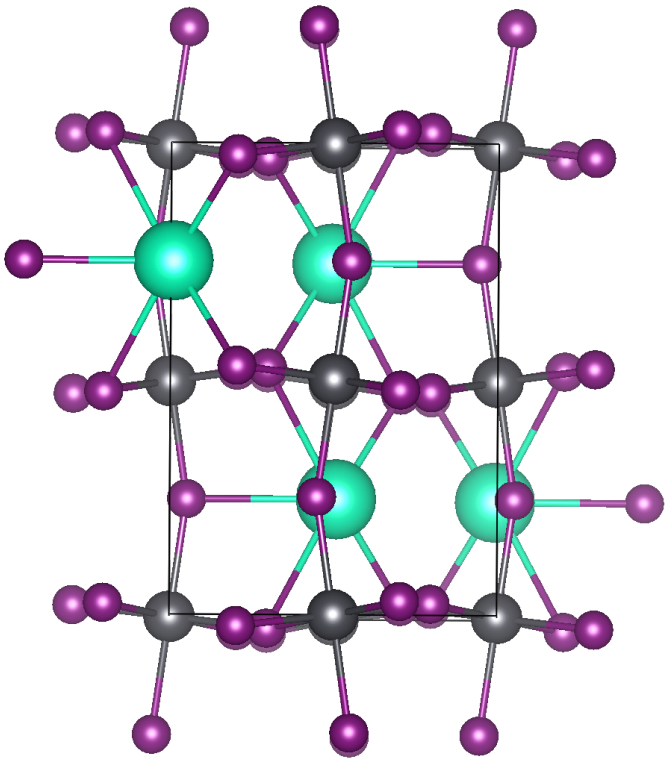

Figure 2.3: Unit cell of orthorhombic $CsPbI_3$

2.2 Methodology

2.2.1 Density Functional Theory (DFT)

Density functional theory provides a computationally efficient way to investigate the electronic and atomic structure of many-body systems quantum mechanically, such as molecules and condensed phases. According to the Hohenberg-Kohn theorem [24], the ground state properties of a N-electron many-body system can be determined by functionals of the spatially dependent electron density

$$n(\vec{r}) = N \int d^3\vec{r}_2 \cdots \int d^3\vec{r}_N \Psi^*(\vec{r}, \vec{r}_2, ..., \vec{r}_N)\Psi(\vec{r}, \vec{r}_2, ..., \vec{r}_N) \tag{2.1}$$

where Ψ is the electronic many-body wave function of this system. Instead of solving the full Schrödinger equation for Ψ, the ground state energy can be determined by minimizing the energy functional $E[n]$. In practice, this process is realized by introducing an auxiliary non-interacting system $\{\phi_1, \phi_2, ..., \phi_N\}$ and self-consistently solving the set of Kohn-Sham equations [33]

$$\{-\frac{\hbar^2}{2m}\nabla^2 + V_{ion}(\vec{r}) + V_H[n(\vec{r})] + V_{xc}[n(\vec{r})]\}\phi_i = \epsilon_i\phi_i \tag{2.2}$$

where V_{ion}, V_H and V_{xc} are the external potential caused by the ion-electron interaction, the Hartree potential caused by the electron-electron Coulomb repulsion and the exchange-correlation potential caused by the many-particle interaction, respectively. The electron density reconstructed by this auxiliary non-interacting system is

$$n(\vec{r}) = \sum_{i=1}^{N} |\phi_i(\vec{r})|^2 \tag{2.3}$$

and the total energy is

$$E_{tot} = \sum_{i=1}^{N} \epsilon_i - E_{DC}[n(\vec{r})] \tag{2.4}$$

where E_{DC} is the double counting term that should be subtracted from the summation of the eigen-energies of the auxiliary non-interacting system.

In this thesis, the Vienna Ab-initio Simulation Package (VASP) software package [40, 41] is used for DFT calculations. Wave functions are expanded using the plane-wave basis set, and the projector-augmented wave method (PAW) is implemented for enhanced computational efficiency.

Density functional theory (DFT) has become the most widely used first-principles method for studying the electronic structure of solids. In its standard local density approximation (LDA) or generalized gradient approximation (GGA), DFT provides an efficient description of bonding and ground-state properties for a wide variety of materials [26]. However, these semilocal exchange–correlation functionals systematically underestimate band gaps and often fail to capture the physics of systems containing localized d or f electrons. The main limitation arises from the self-interaction error and the tendency of LDA/GGA to artificially delocalize electrons in partially filled, strongly correlated orbitals.

To address this issue, the so-called DFT+U method was introduced. The approach supplements the conventional DFT functional with an additional Hubbard-like on-site Coulomb term that penalizes partial occupancies of localized states. In practice, DFT+U corrects the electronic structure by driving orbital occupations toward integer values and restoring a more realistic degree of electron localization.

Several formulations of the DFT+U correction exist. The most widely employed is the rotationally invariant scheme proposed by Dudarev *et al.* [14], which introduces an effective interaction parameter $U_{eff} = U - J$, combining the on-site Coulomb interaction U and Hund's exchange J. Alternative formulations, such as the Liechtenstein approach, treat U and J explicitly [53]. In all cases, an additional double-counting correction must be included to avoid repeating electron–electron interactions already accounted for at the DFT level.

Despite its empirical nature, DFT+U has been highly successful in improving band gaps, magnetic moments, and structural properties of correlated materials at a modest

computational cost compared to hybrid functionals or many-body methods. Nevertheless, the approach is not parameter-free: the numerical value of U depends on the choice of localized orbital basis, the pseudopotential or projector scheme, and the implementation details of the code. As a result, U values are generally not transferable across different materials or software packages, and they are often determined either by linear-response calculations, constrained random phase approximation (cRPA), or by fitting to experimental data.

In this thesis, DFT+U is extensively applied in both halide perovskites and chalcogenides, which not only provides satisfactory benchmarking for materials parameters, but also reduces the cost of computational resources drastically.

2.2.1.1 Defect Calculation using DFT

Defect formation energies (DFE) can be derived according to the following equations using the results from DFT calculations based on the supercell method [17]:

$$DFE[X^q] = E[X^q] - E_{bulk} - \Sigma_i n_i \mu_i + q(\epsilon_{VB} + \epsilon_F) + E^q_{corr} \tag{2.5}$$

where $E[X^q]$ is the energy of the supercell with defect X in charge state q, E_{bulk} is the energy of the pristine supercell, n and μ are respectively the number and chemical potential of atoms added to or subtracted from the bulk supercell, ϵ_{VB} is the energy of the valence band maximum (VBM), and ϵ_F is the position of the Fermi level with respect to VBM. E^q_{corr} is the charged-cell correction to DFE due to the interaction of localized defect charge in a finite-size supercell with its periodic images, which is typically calculated in the Freysoldt, Neugebauer and Van de Walle (FNV) correction scheme [18]. The defect thermodynamic transition levels can be calculated as:

$$\epsilon(q/q') = \frac{E[X^q] - E[X^{q'}]}{q' - q} + \frac{E^q_{corr} - E^{q'}_{corr}}{q' - q} - \epsilon_{VB} \tag{2.6}$$

which identify the position of fermi level for charge state transitions.

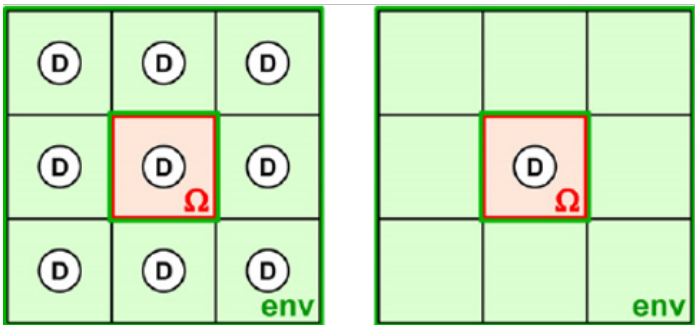

Figure 2.4: Simulation scheme for defect in DFT under periodic boundary condition. In order to simulate an isolated single defect, finite-size correction for spurious interaction between defect images is needed.

2.2.1.2 Finite-size Charged-cell Correction

As shown in Fig. 2.4, DFT simulation of defect under the periodic boundary condition introduces spurious interaction between the simulated defect and its images. As a result, the raw data of defect formation energies from DFT need correction.

In DFT calculations, a defect with charge q is represented as a localized charge distribution of magnitude q along with a uniform compensating jellium background of charge density $-q/\Omega$, where Ω is the supercell volume. This setup introduces spurious electrostatic interactions—not only between periodic images of the localized charge, but also between the localized charge and the jellium background in neighboring image cells—which must be corrected for accurate defect energetics. The Freysoldt–Neugebauer–Van de Walle (FNV) approach is particularly well-suited for correcting the energies of charged defects in a dielectric medium. In this scheme, the DFT-calculated electrostatic potential is explicitly utilized to construct a more accurate model of the defect-induced electrostatics. The total correction to the defect formation energy is then expressed as

$$E_{corr} = E_{lat} - qV_{q/0} \tag{2.7}$$

where E_{lat} corresponds to the correction energy for a model charge distribution. For a point charge model

$$E_{lat} = \frac{q^2\alpha}{2\epsilon L} \tag{2.8}$$

where α is the Madelung constant, which depends on the Bravais lattice. The potential alignment term $qV_{q/0}$ is obtained by comparing the electrostatic potential from the model charge distribution with the difference between the DFT-calculated potentials of the charged defect supercell and the corresponding bulk supercell

$$V_{q/0} = (V_q^{DFT} - V_{bulk}^{DFT})|_{far} - V^{model}|_{far} \tag{2.9}$$

, and can be shown that this term essentially represents the correction for the interaction between the model charge and the compensating jellium background from the periodic images in other supercells. The extended FNV method, also called as the Kumagai method, uses the atomic site potential as a potential marker instead of using the planar-averaged electrostatic potential for determining the potential offset [48].

Although E_{lat} is largely insensitive to the choice of the charge model—since the interaction between the defect and its periodic images is dominated by the long-range Coulomb potential $1/\epsilon r$—a significant issue encountered in this study is that, for a defect X^q, the appropriate charge to use in the correction is not always the formal charge q. In fact, Oba *et al.* have shown for defects in zinc oxide ZnO that, rather than the formal charge q, should be determined for finite-size corrections by examining the specific electronic and structural characteristics of the defect [68]. Specifically, when the formal charges q were used in the correction, the calculated formation energies for defects such as Zn_i^0 and Zn_O^0 failed to converge as the supercell size was extrapolated toward the infinite limit. Instead, using a corrected charge $q_c = +2$ for Zn_i^0 and Zn_O^0 gave satisfactory convergence leading to a good linear L^{-3} dependence. This phenomenon is attributed to the fact that the two additional electrons, relative to the nominally charged defects Zn_i^{2+} and Zn_O^{2+}, occupy extended states

at the conduction band minimum (CBM) rather than localized in-gap defect states. Consequently, these electrons do not effectively screen the +2 core charges, and the long-range electrostatic behavior of the nominally neutral defects remains essentially identical to that of their +2 charged counterparts. A similar behavior has been reported for the neutral defects in InP [8].

In this thesis, the electronic characteristics of charged defects obtained from DFT calculations are systematically examined. The density-derived electrostatic and chemical (DDEC) method [54, 83] is employed to determine the net atomic charges (NACs) of all atoms in the lattice, including impurities and defect sites. This analysis provides a direct measure of charge localization and is particularly useful for identifying the appropriate correction charge q_c. For example, the NAC distributions of Zn_i^0 and Zn_i^{2+} are nearly identical, confirming that the two additional electrons in Zn_i^0 are delocalized rather than localized on the defect site. Such cases illustrate why using nominal charges q in the Freysoldt–Neugebauer–Van de Walle (FNV) correction scheme can lead to substantial errors: partial localization or delocalization of charges may cause E_{corr} to be over- or underestimated. To address this limitation, a modified correction scheme is adopted here, in which NACs from the DDEC method are used as the starting point to quantify charge localization and apply physically justified, reliable corrections to defect formation energies.

Following the DDEC analysis, the net atomic charges q_{NAC} associated with each defect are obtained. However, it is noted that q_{NAC} represents the dielectrically screened charge distribution, rather than the fully localized unscreened charge required for the Freysoldt–Neugebauer–Van de Walle (FNV) correction. To estimate the appropriate unscreened localized charge, a scaling factor k is introduced. This factor is carefully calibrated to account for the dielectric screening that may be implicitly included in the DDEC-derived charges but absent in the FNV model. The product of q_{NAC} and the scaling factor k is then treated as the effective localized charge q_{loc} used in the FNV correction scheme,

$$q_{\mathrm{loc}} = k * q_{\mathrm{NAC}}. \tag{2.10}$$

Conceptually, the scaling factor k, defined as the ratio between the original localized charge and the net atomic charge (NAC) after dielectric screening, is determined by the dielectric properties of the host material. In practice, the scaling factor k can be determined using one of two approaches. In the first approach, defects known to be fully localized are selected, allowing the nominal defect charge to be equated with the localized charge q_{loc}. Under this condition, the value of k can be directly calculated. However, this method is often impractical, as it requires prior knowledge of the extent of charge localization, which is not always available.

As an alternative, the second approach involves systematically varying the supercell size and tuning the value of k to achieve convergence of the defect formation energy across different supercell dimensions. For both methods, it is recommended that defects with relatively large values of q_{NAC} be selected, since these yield larger correction terms and thereby reduce the relative uncertainty in the evaluation of k. This strategy ensures that the derived scaling factors are both meaningful and effective in improving the accuracy of the charge correction process.

As an illustrative case, the methodology described above is applied to the study of defects in CdTe. The defect system selected as a reference for determining the scaling factor k is Te_{Cd}^{+}, which is found to exhibit localized deep Kohn–Sham levels within the bandgap. As will be shown in a later section, both the (0/+1) and (+1/+2) charge transition levels associated with this defect lie deep within the bandgap and are characterized by large carrier capture cross sections, consistent with prior theoretical studies [39]. By applying the supercell extrapolation method described previously, a k value of 3.5 is obtained for CdTe. Specifically, 64-atom, 216-atom and 512-atom supercells are constructed for calculation of defect formation energies. This obtained k value is subsequently validated by applying it to other charged defects.

As demonstrated by the examples in Fig. 2.5, the effectiveness of the proposed charge correction method in addressing the limitations of the traditional FNV approach is evident.

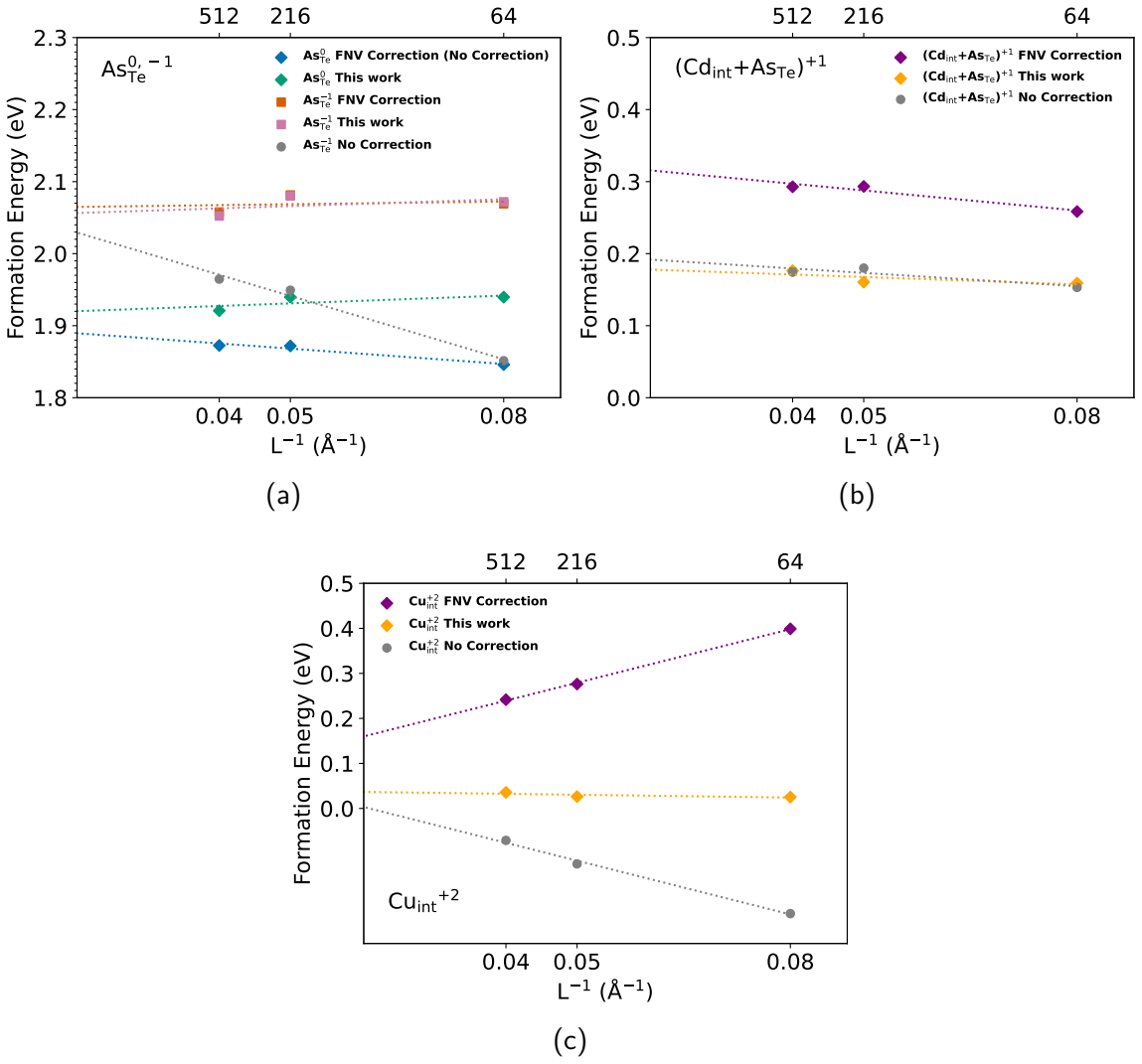

Figure 2.5: Defect formation energies vs. inversed supercell size for (a) $As_{Te}^{0,-1}$, (b) $(Cd_{int} + As_{Te})^{+}$ and (c) Cu_{int}^{+2}.All defect structures are relaxed with fixed lattice parameters. The quantity shown on the x-axis represents the inverse of the linear dimension of the corresponding cubic CdTe supercell.

In addition to this improvement, several critical observations warrant further discussion:

- Nominally neutral defects with $q = 0$, such as As^{0}_{Te} shown in Fig. 2.5a, may effectively behave as charged defects accompanied by a delocalized electron or hole, and therefore still require finite-size corrections. Specifically, As^{0}_{Te} can be approximated as As^{-1}_{Te}

with a missing electron (i.e., an additional hole) residing at the valence band maximum (VBM). Since such delocalized carriers are unable to fully screen the localized defect charge, residual spurious Coulomb interactions can persist even in nominally neutral systems. This phenomenon has also been noted in previous studies [68]. By applying the charge correction method introduced in this section, the (0/–1) transition level of As_{Te} is corrected to lie 0.13 eV above the VBM, resulting in improved agreement with experimental observations [67].

- For charged defects with partially localized charge distributions, the proposed method effectively accounts for the discrepancy between the localized charge q_{loc} and the nominal charge q. This approach mitigates the risk of overcorrection commonly observed when applying the traditional FNV scheme. The accuracy of the method is validated by the consistent defect formation energies obtained for Cu_{int} across supercells containing 64, 216, and 512 atoms, as illustrated in Fig. 2.5c.

For many intrinsic defects in relatively ionic compounds, such as zinc interstitials in ZnO and tin vacancies in $CsSnI_3$, it is often found that the the correction charges are effectively the same across different charge states of a given defect. As mentioned above, Zn_i^0 basically behaves as Zn_i^{+2} with two delocalized CB-like electrons. Similarly, V_{Sn}^0 in $CsSnI_3$ behaves as V_{Sn}^{-2} with two VB-like holes. Use nominal charge q for correction will result in overestimation of how deep the transition levels are in the bandgap for these type of defects. For highly localized defects, such as As_{Te}^{-1} in CdTe shown in Fig. 2.5a, the results obtained using the proposed correction method are found to be consistent with those from the traditional FNV approach, indicating minimal discrepancy. These findings show the robustness of the developed finite-size correction scheme, which not only reproduces established results for well-localized defects but also extends applicability to more complex cases involving partial charge delocalization—thereby overcoming key limitations of existing methods.

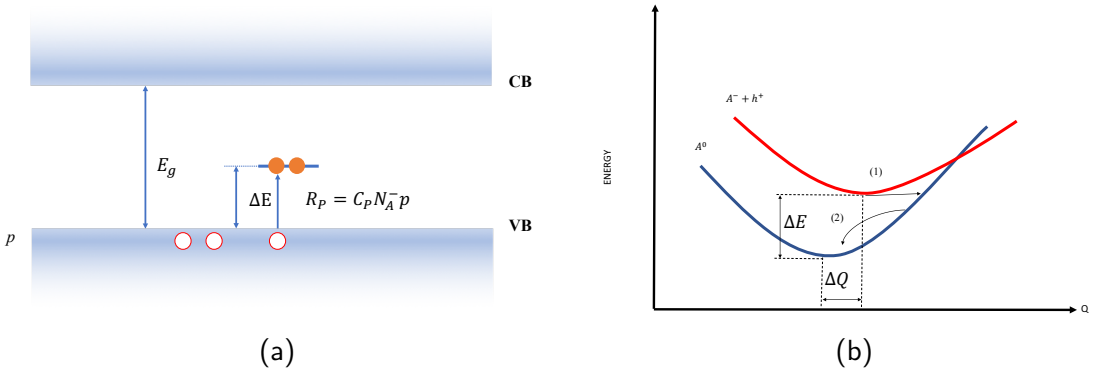

Figure 2.6: Representation of carrier capture at a defect: (a) band diagram and (b) configuration coordinate diagram. The defect in the diagram is a deep acceptor with a negative and a neutral charge state. $\triangle E$ is the ionization energy of the defect, and Q is a properly selected configuration coordinate. In (b), step(1) is the change of the electronic state due to electron-phonon coupling (nonradiative) and step(2) is the vibration relaxation due to phonon-phonon interactions.

2.2.1.3 Defect-assisted Non-radiative Recombination

Both radiative and non-radiative recombinations exist in semiconductor materials. Radiative recombination is the process in which an electron in the conduction band recombines with a hole in the valence band by emitting a photon, which is intrinsic and inevitable. On the other hand, non-radiative recombination mechanisms, including Auger and Schockley-Read-Hall (SRH) recombination, can further degrade the carrier lifetime and device performance. In this section, we mainly focus on the defect-assisted SRH recombination process and show how to calculate the corresponding recombination rates using DFT from first-principles.

Defect-assisted SRH recombination process can be understood by the configuration coordinate diagram (CCD), as shown in Fig. 2.6. The red and blue curves in Fig. 2.6b represent the energy dispersion of charge state A^- and A^0 with respect to the change of their atomic coordinates, respectively. The difference in energy minimum of the two curves correspond to the (0/-) transition level. Due to the different structural relaxation of A^-

and A^0, their equilibrium positions are differed by

$$\Delta Q = \sqrt{\sum_{\alpha} m_{\alpha}(R_{\alpha}^{f} - R_{\alpha}^{i})^2} \tag{2.11}$$

where m_α, R_α^f and R_α^i are the mass, final and initial Cartesian coordinates of atom α in the defective supercell, respectively. The process of A^- capturing a hold from the valence band can be divided into two steps: (1) the transition of charge state from A^- to A^0 facilitated by the electron-phonon coupling and (2) the relaxation of atomic structures for A^0 due to emission of phonons. The non-radiative carrier-capture coefficients can be calculated by Fermi's gold rule:

$$C_{n/p} = \frac{2\pi}{\hbar} g V W_{if}^2 \sum_m w_m \sum_n |\left\langle \chi_{im} | \hat{Q} - Q_0 | \chi_{fn} \right\rangle|^2 \times \delta(\Delta E + m\hbar\Omega_i - n\hbar\Omega_f) \tag{2.12}$$

where χ_{im} and χ_{fn} are the wavefunctions of the m$^{\text{th}}$ and n$^{\text{th}}$ phononic wave functions in the initial i and final f states. V is the supercell volume, g is the configurational degeneracy and W_{if} is the electron-phonon overlap. w_m is the probability of thermal occupation of the m$^{\text{th}}$ phonon state, and Ω_i/Ω_f are the inital/final phonon frequencies. The anharmonic potential energy surfaces (PES) in CCDs are constructed by linearly interpolating between the equilibrium structures of A^- to A^0, and then used for obtaining the phonon frequencies as well as the phonon wave functions by solving the one-dimensional Schrödinger equations. The NONRAD package combined with VASP are applied for realizing the calculation scheme shown above.

Once the non-radiative carrier-capture coefficients are calculated, the SRH recombination rate can be estimated by the following equation:

$$R^{SRH} = \frac{np - n_i^2}{\tau_p \left[n + n_i e^{(E_t - E_i)/k_{\text{B}}T} \right] + \tau_n \left[p + n_i e^{(E_i - E_t)/k_{\text{B}}T} \right]} \tag{2.13}$$

in which n and p are electron and hole concentrations, n_i is the intrinsic carrier concentration, E_t is the thermodynamic transition level of a pair of charge states (e.g. A^-/A^0), and

$$\tau_p = \frac{1}{C_p N_t} \qquad \tau_n = \frac{1}{C_n N_t} \ , \tag{2.14}$$

are the hole and electron lifetimes, respectively. The trap density N_t is defined as the sum of the concentrations of both charged defects involved. The resulting calculated R_{SRH} can be used to identify deep carrier traps and serve as input parameters in the TCAD model.

2.2.1.4 Defect Diffusion Migration Barrier

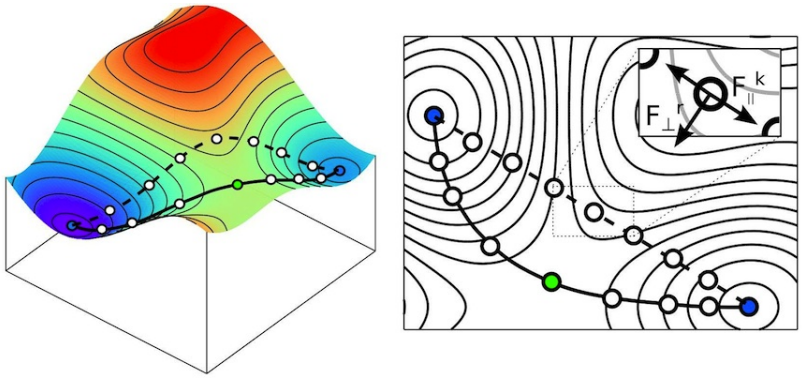

Figure 2.7: Nudged elastic band method for finding diffusion barrier.

The migration energy barrier is a critical parameter for quantifying defect diffusivity in semiconductors. To determine this barrier from first principles, the nudged elastic band (NEB) method is commonly employed [22], as it enables the calculation of the minimum energy path between fixed initial and final atomic configurations. The migration barriers obtained from NEB calculations also provide essential input parameters for the process simulation component of our TCAD model, facilitating a more accurate prediction of defect dynamics and their impact on device performance.

2.2.2 Continuum Modeling

2.2.2.1 Process Simulation

Process simulation as implemented in Sentaurus Sprocess is used to study the distribution of defects under situations away from equilibrium, such as thermal annealing in the manufacturing process and transient process under illumination. The transport and reaction of defects are described by the continuity equations. Based on Fick's first law

$$J = -D\nabla C - C\mu\nabla U, \tag{2.15}$$

the flux of defects is composed of the diffusion term which is proportional to the concentration gradient ∇C, and the drift term which is proportional to the electrochemical potential gradient ∇U. D is the diffusivity and μ is the mobility. On the other hand, Poisson's equation relates the electric potential ψ and net charge density ρ by

$$\nabla^2\psi = \frac{\rho}{\epsilon} \tag{2.16}$$

$$\rho = p - n + \sum_i z_i N_{Di}^+ - \sum_j z_j N_{Aj}^- \tag{2.17}$$

where p is the hole density, n is the electron density, N_D^+ is the density of ionized donors and N_A^- is the density of ionized acceptors. z_i is the charge state of donor N_{Di}^+ and z_j is the charge state of acceptor N_{Aj}^-. ϵ is the dielectric constant of the host material. In order to also incorporate the reaction between defects, a modification of Fick's second law (describing the rate of change of defect concentration C_γ) is implemented by adding a reaction-driven term

$$\partial_t C_\gamma = -\nabla \cdot J_\gamma - \sum_l \eta_{\gamma l} R_l \tag{2.18}$$

in which $\eta_{\gamma l}$ denotes the number of defects γ consumed by reaction l and R_l is the associated reaction rate

$$R_l = k_f \left[\prod_{\alpha=1}^{n} C_\alpha - \frac{1}{K} \left(\frac{p}{n_i} \right)^h \prod_{\beta=1}^{m} C_\beta \right] \tag{2.19}$$

where $\{C_\alpha\}$ and $\{C_\beta\}$ are the sets of reactant and product concentrations, respectively. The equilibrium constant K is calculated from the difference in formation energies ΔE_l^f

$$K = \frac{\theta_l}{C_s^{m-n}} e^{-\Delta E_l^f / k_b T} \tag{2.20}$$

using the concentration of possible defect sites C_s and the entropy coefficient θ_l as well. In Eq (2.19), k_f denotes the forward reaction coefficient, which has different form for defect-defect reaction

$$k_f = 4\pi r \sum_\alpha D_\alpha \tag{2.21}$$

and the ionization process

$$k_f = C_{n/p} \tag{2.22}$$

In Eq (2.21), k_f is evaluated using the interaction radius r and the summation of the diffusivities of reactants. By contrast, as shown in Eq (2.22), k_f for the ionization process is simply the carrier-capture coefficient as introduced in Section 2.2.1.3.

The diffusivity D_α can be calculated based on the random walk formalism on a sublattice

$$D_\alpha = g z \lambda^2 \nu \exp(-\frac{E_m}{kT}) \tag{2.23}$$

where g is a geometric factor determined by the dimensionality of the crystal lattice, z is the coordination number of the atomic sites in the lattice. λ is the nearest neighbor hopping distance, which represents the distance between neighboring defect sites which involved in diffusion. ν is the attempt frequency. E_m is the migration barrier energy introduced in Section (2.2.1.4) calculated by the NEB method.

2.2.2.2 Detailed Balance of Multilevel Defect Recombination

Traditionally, experimentally measured carrier lifetimes are used directly as inputs for device simulations. However, this approach becomes inadequate when defects possess more than two charge states and, consequently, multiple transition levels. In contrast to a single defect level, the occupancy of such coupled levels depends on the Fermi level position, doping concentration, and injection level. Under these conditions, recombination behavior must instead be described using the multilevel defect recombination model, originally developed by Sah and Shockley [76].

As an illustrative example, consider a defect X that can exist in three charge states: neutral, +1, and +2. In this case, four possible ionization processes can occur, each associated with a corresponding reaction rate:

$$\mathrm{X}^{2+} + e^- \rightarrow \mathrm{X}^{+} \qquad R1 = k_1(C^{2+}n - C^{+}n_1) \tag{2.24}$$

$$\mathrm{X}^{+} + h^+ \rightarrow \mathrm{X}^{2+} \qquad R2 = k_2(C^{+}p - C^{2+}p_1) \tag{2.25}$$

$$\mathrm{X}^{+} + e^- \rightarrow \mathrm{X}^{0} \qquad R3 = k_3(C^{+}n - C^{0}n_2) \tag{2.26}$$

$$\mathrm{X}^{0} + h^+ \rightarrow \mathrm{X}^{+} \qquad R4 = k_4(C^{0}p - C^{+}p_2) \tag{2.27}$$

$$\begin{aligned} k_1 &= \nu_{th}\sigma^{e}_{+1/+2}, \quad k_2 = \nu_{th}\sigma^{h}_{+1/+2} \\ k_3 &= \nu_{th}\sigma^{e}_{+1/0}, \quad k_4 = \nu_{th}\sigma^{h}_{0/+1} \end{aligned} \tag{2.28}$$

where ν_{th} denotes the thermal velocity, and σ represents the carrier capture cross section for each charge transition process. C^q is the defect density in charge state q. The remaining

parameters can be expressed as functions of the Fermi level and the trap transition levels.:

$$n = N_c \exp\left(\frac{E_{F,n} - E_c}{kT}\right) \tag{2.29}$$

$$p = N_v \exp\left(\frac{E_v - E_{F,p}}{kT}\right) \tag{2.30}$$

$$n_1 = N_c \exp\left(\frac{E_{\text{trap},1} - E_c}{kT}\right) \tag{2.31}$$

$$n_2 = N_c \exp\left(\frac{E_{\text{trap},2} - E_c}{kT}\right) \tag{2.32}$$

$$p_1 = N_v \exp\left(\frac{-E_{\text{trap},1} + E_v}{kT}\right) \tag{2.33}$$

$$p_2 = N_v \exp\left(\frac{-E_{\text{trap},2} + E_v}{kT}\right) \tag{2.34}$$

Given the rates of the relevant ionization processes, the time derivatives of the defect densities can be explicitly expressed. Under steady-state conditions, densities remain unchanged and these time derivatives are set to zero.

$$\begin{aligned}\frac{dC^0}{dt} &= R3 - R4 \\ &= k_3(C^+ n - C^0 n_2) - k_4(C^0 p - C^+ p_2) = 0\end{aligned} \tag{2.35}$$

$$\begin{aligned}\frac{dC^+}{dt} &= R2 - R1 - R3 + R4 \\ &= k_1(C^{2+} n - C^+ n_1) - k_2(C^+ p - C^{2+} p_1) \\ &\quad - k_3(C^+ n - C^0 n_2) + k_4(C^0 p - C^+ p_2) = 0\end{aligned} \tag{2.36}$$

$$\begin{aligned}\frac{dC^{2+}}{dt} &= R2 - R1 \\ &= k_2(C^+ p - C^{2+} p_1) - k_1(C^{2+} n - C^+ n_1) = 0\end{aligned} \tag{2.37}$$

which result in the ratio between densities of charge states

$$\frac{C^{+}}{C^{0}} = \frac{k_3 n_2 + k_4 p}{k_3 n + k_4 p_2} = K^{+1/0} \tag{2.38}$$

$$\frac{C^{2+}}{C^{+}} = \frac{k_2 p + k_1 n_1}{k_2 p_1 + k_1 n} = K^{+2/+1} \tag{2.39}$$

$$\frac{C^{2+}}{C^{0}} = \frac{(k_2 p + k_1 n_1)(k_3 n_2 + k_4 p)}{(k_2 p_1 + k_1 n)(k_3 n + k_4 p_2)} = K^{+2/0} \tag{2.40}$$

and with the frozen-in approximation usually applied,

$$C^{0} + C^{+} + C^{2+} = C^{T} \text{ (Total Defect Density)} \tag{2.41}$$

all the defect charge state densities can then be fully determined.

Schematic of the multilevel defect recombination is shown in Fig. 2.8. The total SRH recombination rate should be the summation of two components if the two transition levels are not coupled [78]

$$R_{tot}^{SRH} = R_{+1/0}^{SRH} + R_{+2/+1}^{SRH} \tag{2.42}$$

where within $R_{+1/0}^{SRH}$ and $R_{+2/+1}^{SRH}$ the trap densities for calculating carrier lifetimes are correspondingly

$$N_t^{+1/0} = C^{+} + C^{0} \tag{2.43}$$

$$N_t^{+2/+1} = C^{2+} + C^{+}. \tag{2.44}$$

Under illumination, injected carriers lead to a redistribution of defect charge-state densities, often deviating substantially from their thermal-equilibrium values. Consequently, the carrier capture lifetimes and the SRH recombination rate are not fixed quantities, but instead depend on factors such as the injection level and the position of the Fermi level. This model is implemented in the Sentaurus TCAD simulation using the Physical Model Interface (PMI).

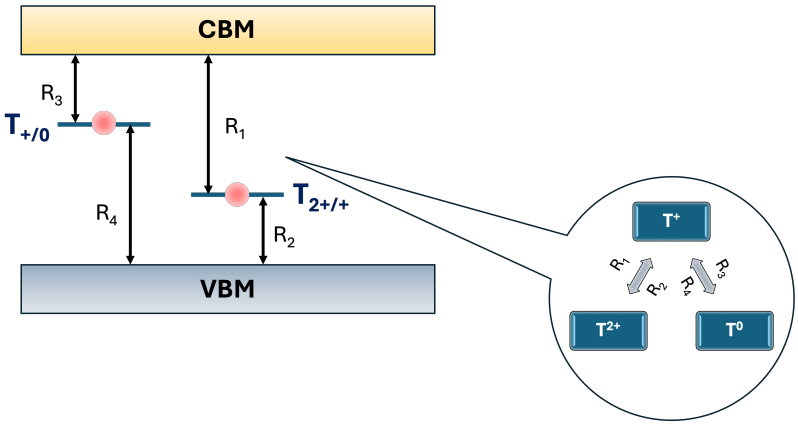

Figure 2.8: Schematic of multilevel defect recombination. $'T'$ represents trap transition levels. The trap in the figure has $0/+1/+2$ charge states. R1∼R4 are capture and emission rate under steady state in SRH recombination.

2.2.2.3 Device Simulation

Device simulations, implemented using Sentaurus SDevice [82], are employed to describe carrier transport and recombination processes throughout the device, thereby enabling the prediction of its optical and electrical characteristics. The underlying models are based on Poisson's equation and the carrier continuity equations. Poisson's equation is used to determine the spatial distribution of the electrostatic potential within the device, while the continuity equations are solved to obtain the carrier concentrations:

$$\frac{\partial n}{\partial t} = \nabla \cdot j_n/q + (G - R) \tag{2.45}$$

$$\frac{\partial p}{\partial t} = \nabla \cdot j_p/q + (G - R) \tag{2.46}$$

where j_n and j_p denote electron and hole current densities, G and R represent the carrier generation and recombination rate, respectively. Drift and diffusion of carriers can be described by:

$$j_n = q\mu_n n\varepsilon + qD_n \frac{\partial n}{\partial x} \tag{2.47}$$

$$j_p = q\mu_p p\varepsilon - qD_n \frac{\partial p}{\partial x} \tag{2.48}$$

where μ_n and μ_p are electron and hole mobility, D_n and D_p are diffusivities of electron and hole, and ε is the electric field derived from Poisson's equation.

Process simulations are used to determine the spatial distribution of doping concentrations and defect densities within the device. These outputs are subsequently incorporated into the device simulator. Shallow-level defects are treated as dopants using the Incomplete Ionization model, whereas deep-level defects are represented within the Shockley–Read–Hall (SRH) recombination framework to capture carriers. The capture cross sections for these defects are calculated using the procedure described in Section 2.2.1.3. The Physical Model Interface is employed to seamlessly integrate process simulation data with the device simulator and to account for variations in defect transition levels arising from differences in material properties.

Another key component of device simulation is optical modeling, which is essential for accurately predicting the performance of optoelectronic devices such as solar cells. The optical simulator computes light propagation through each device layer and determines both the spectral absorption profile and the resulting carrier generation rate, G, as defined in Eq. 2.45 and Eq. 2.46. The quantum yield model is used to quantify the fraction of absorbed photons that generate electron–hole pairs. In this approach, the quantum yield is set to unity when the photon energy is greater than or equal to the material bandgap, E_g, and to zero otherwise.

In this work, the transfer-matrix method (TMM) [82] is employed to simulate optical generation in CdSeTe solar cells. The ElementWise option is enabled to account for spatial variations in material properties within the device. The complex refractive index and other wavelength-dependent optical parameters are obtained from reported experimental datasets. The simulated results exhibit excellent agreement with experimental measurements, thereby validating the accuracy and reliability of this optical modeling approach.

Chapter 3

FIRST-PRINCIPLES STUDY OF POINT DEFECTS IN INORGANIC HALIDE PEROVSKITES

Inorganic halide perovskites have emerged as promising candidates for optoelectronic applications due to their enhanced environmental stability compared to their hybrid counterparts. However, the presence of point defects in these materials can critically influence carrier concentrations and recombination lifetimes, thereby limiting device performance. A comprehensive understanding of the formation and electronic properties of these defects is therefore essential for optimizing material quality and functionality.

In this chapter, generalized gradient approximation with Hubbard U correction (GGA+U) and spin–orbit coupling (SOC) is employed to investigate native point defects in $CsPbI_3$ and $CsSnI_3$. Defect formation energies and evaluate non-radiative recombination rates for selected deep-level defects are calculated using first-principles methodologies. Notably, the results reveal that iodine interstitials in $CsPbI_3$ and tin interstitials in $CsSnI_3$ exhibit particularly high non-radiative carrier capture rates, suggesting their significant role in limiting carrier lifetime. Furthermore, it is demonstrated that accurate defect energetics and atomic relaxations are only attainable when sufficiently large supercells are used, due to long-range defect-induced lattice distortions. This study not only identifies critical non-radiative recombination pathways associated with interstitial defects, but also underscores the necessity of using large supercells to ensure the reliability of defect calculations in halide perovskites. [1]

[1] This section is adapted from our publication: Yijun Tong, Xiaofeng Xiang and Scott Dunham. Interstitals as non-radiative recombination centers for all-inorganic halide perovskites, Computational Materials Science, 2025, 246, 113384.

3.1 Methods

The underestimation of bandgap values in halide perovskites when using (semi)local exchange–correlation functionals, such as the generalized gradient approximation (GGA), is a well-documented limitation—particularly when spin–orbit coupling (SOC) is included. To date, only hybrid density functionals with empirically adjusted mixing parameters for the exchange interaction have been shown to yield accurate bandgap predictions [105, 108]. However, applying hybrid functionals in combination with SOC is computationally demanding, thereby restricting the feasible supercell size for defect calculations. Moreover, the adjustment of the mixing parameter introduces a degree of semi-empiricism that may affect the transferability of the results.

To address these challenges, the native point defects in γ-$CsPbI_3$ and γ-$CsSnI_3$ are investigated using GGA+U calculations with SOC. This approach enables us to achieve reasonable agreement with experimental bandgap values while maintaining computational efficiency, thereby allowing the usage of larger supercells in defect modeling.

3.1.1 Details of DFT Calculations

The revised Perdew–Burke–Ernzerhof exchange–correlation functional for solids (PBEsol) [73] was employed in this study, with spin–orbit coupling (SOC) included in both the electronic structure calculations and structural relaxations for bulk and defect-containing supercells. A kinetic energy cutoff of 500eV was used for the plane-wave basis set. Van der Waals interactions were accounted for using the DFT-D3 correction scheme [21]. Effective Hubbard U parameters, following the simplified rotationally invariant approach [14], were applied to the p orbitals of Pb ($U_{\text{eff}} = 5$ eV) in γ-$CsPbI_3$ and Sn ($U_{\text{eff}} = 4.3$ eV) in γ-$CsSnI_3$.

For bulk calculations of γ-$CsPbI_3$ and γ-$CsSnI_3$ (space group Pnma), a Γ-centered $4 \times 4 \times 3$ k-point mesh was used. Defect calculations were carried out in 360-atom supercells, constructed using a $3 \times 3 \times 2$ expansion of the conventional unit cell. A single Γ-point was employed for Brillouin zone sampling in defect calculations. All atomic structures were

Table 3.1: Structural parameters and band gaps from GGA+U and HSE

	$\gamma-CsPbI_3$		$\gamma-CsSnI_3$	
	GGA+U	HSE (α=0.43)	GGA+U	HSE (α=0.59)
a [Å]	9.18	9.02	9.04	8.77
b [Å]	8.44	8.59	8.35	8.61
c [Å]	12.53	12.48	12.44	12.38
V [$Å^3$]	970.81	966.97	939.02	934.81
Band gap [eV]	1.63	1.67	1.25	1.29

relaxed until the residual forces on each atom were below 5 meV/Å.

For comparison, additional hybrid functional calculations were performed using the Heyd–Scuseria–Ernzerhof (HSE) functional. The mixing parameters were set to $\alpha = 0.43$ for γ-$CsPbI_3$ and $\alpha = 0.59$ for γ-$CsSnI_3$, following prior studies [105, 108]. Due to computational limitations, SOC was not included during structural relaxation in the HSE calculations.

In Table 3.1, the calculated structural parameters and bandgap values for both γ-$CsPbI_3$ and γ-$CsSnI_3$ are presented, based on GGA+U and HSE methods. The lattice constants along the c-axis, as well as the cell volumes, are found to be similar between the two computational approaches. The lattice parameters obtained from GGA+U are slightly larger along the a-axis and smaller along the b-axis compared to those from HSE. This anisotropic distortion is likely caused by the different orbital occupations of Pb-s/p and I-p states along the a and b directions. Because the Hubbard U correction is applied isotropically, it shifts the orbital energies in an unequal manner across different bonding directions, which in turn generates different force imbalances along the a and b axes. A similar phenomenon has been reported in $LaMnO_3$, where a strong correlation between cooperative Jahn–Teller distortion and oxygen-octahedral rotations was observed using the GGA+U method [51]. The bandgap values of both perovskites predicted by GGA+U and

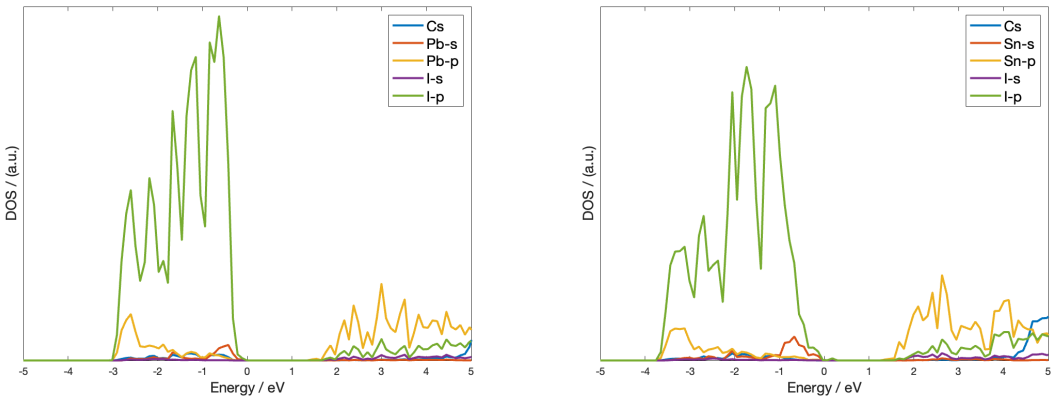

Figure 3.1: Calculated DOS of (a) $\gamma-CsPbI_3$ and (b) $\gamma-CsSnI_3$ using GGA+U.

HSE are also in close agreement.

The calculated density of states (DOS) are shown in Fig. 3.1a and Fig. 3.1b. For both materials, the valence band maxima (VBM) are found to be primarily composed of I-p and Pb-s/Sn-s orbitals, while the conduction band minima (CBM) are dominated by Pb-p/Sn-p orbitals, consistent with previous reports [93]. In this work, the bandgap values are corrected by the application of Hubbard U parameters on the Pb-p/Sn-p orbitals, which effectively shift the conduction bands to higher energies.

3.1.2 Thermodynamic Stability of Perovskites

To identify the allowable range of chemical potentials for all constituent elements, the thermodynamic stability of both perovskites is evaluated. Under equilibrium growth conditions, the chemical potentials of Cs, Pb/Sn, and I are constrained by the following relation:

$$\mu_{Cs} + \mu_{Pb/Sn} + 3\mu_I = E(CsPbI_3/CsSnI_3) \tag{3.1}$$

where E denotes the total energy obtained from DFT calculations. To prevent the formation of secondary phases such as PbI_2/SnI_2 and CsI, the chemical potential values must also satisfy the following additional constraints:

$$\mu_{Pb/Sn} + 2\mu_I < E(PbI_2/SnI_2) \tag{3.2}$$

$$\mu_{Cs} + \mu_I < E(CsI) \tag{3.3}$$

and the corresponding selected chemical potential values for different preparation conditions are summarized in Table 3.2 and Table 3.3. These values are chosen to represent representative growth environments, including element-rich and element-poor conditions, while ensuring thermodynamic stability against competing secondary phases.

Table 3.2: Selected chemical potential values (eV) in $CsPbI_3$

	μ_{Cs}	μ_{Pb}	μ_I
Pb-rich	-3.0549	-1.9983	-3.064
Pb-moderate	-3.5551	-2.9983	-2.5639
Pb-poor	-4.1421	-4.1724	-1.9769

Table 3.3: Selected chemical potential values (eV) in $CsSnI_3$

	μ_{Cs}	μ_{Sn}	μ_I
Sn-rich	-3.0857	-1.8113	-3.1161
Sn-moderate	-3.4609	-2.5613	-2.741
Sn-poor	-3.7359	-3.1113	-2.4661

3.2 Defect Calculations of $CsPbI_3$ and $CsSnI_3$

The calculated defect formation energies (DFEs) of selected native point defects in $CsPbI_3$ and $CsSnI_3$ are shown in Fig. 3.3 and Fig. 3.4, respectively. The equilibrium concentration of each defect is exponentially dependent on the negative of its formation energy. The corresponding defect transition levels are presented in Fig. 3.2.

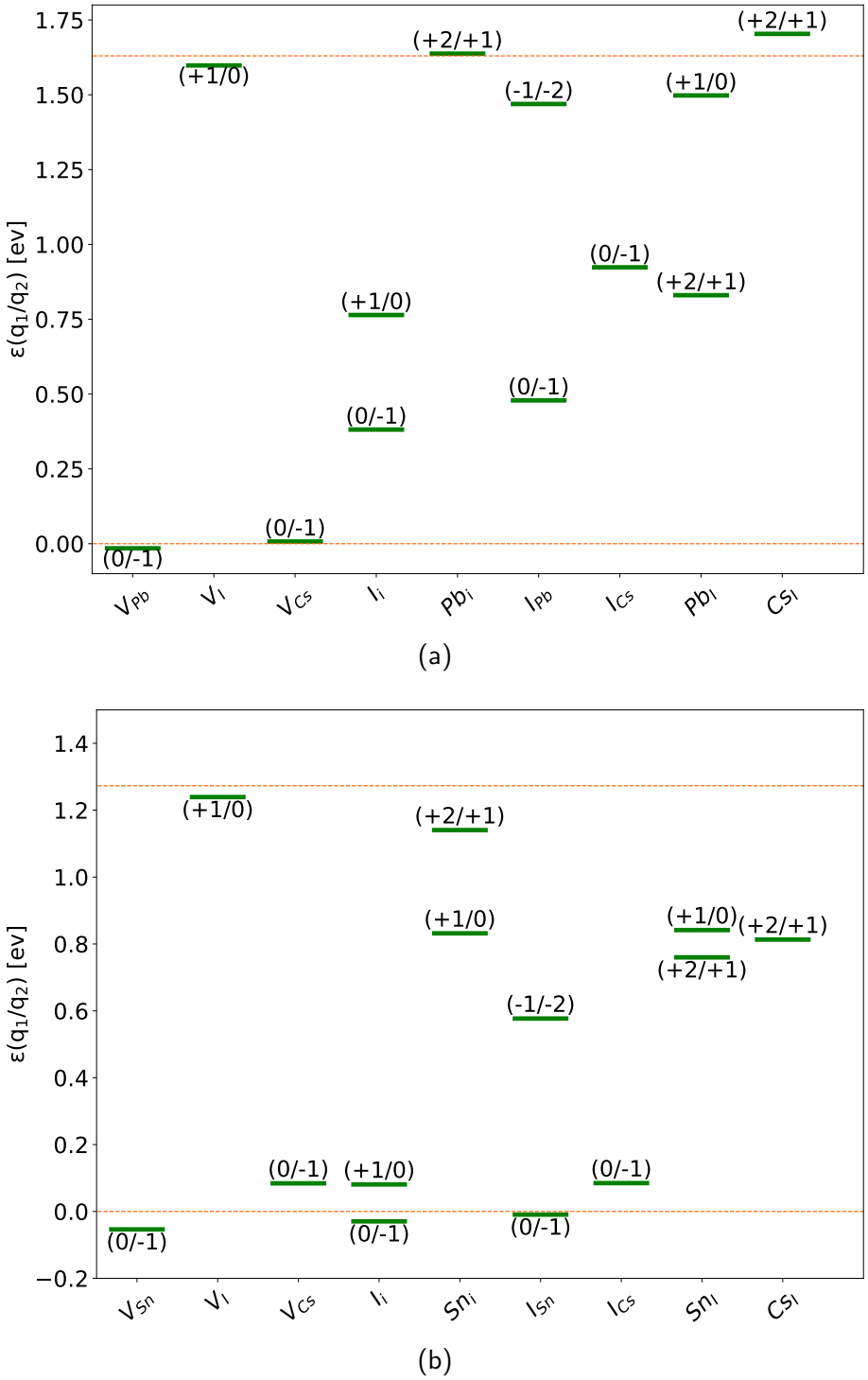

Figure 3.2: Defect transition levels of selected native defects in (a) $CsPbI_3$ and (b) $CsSnI_3$.

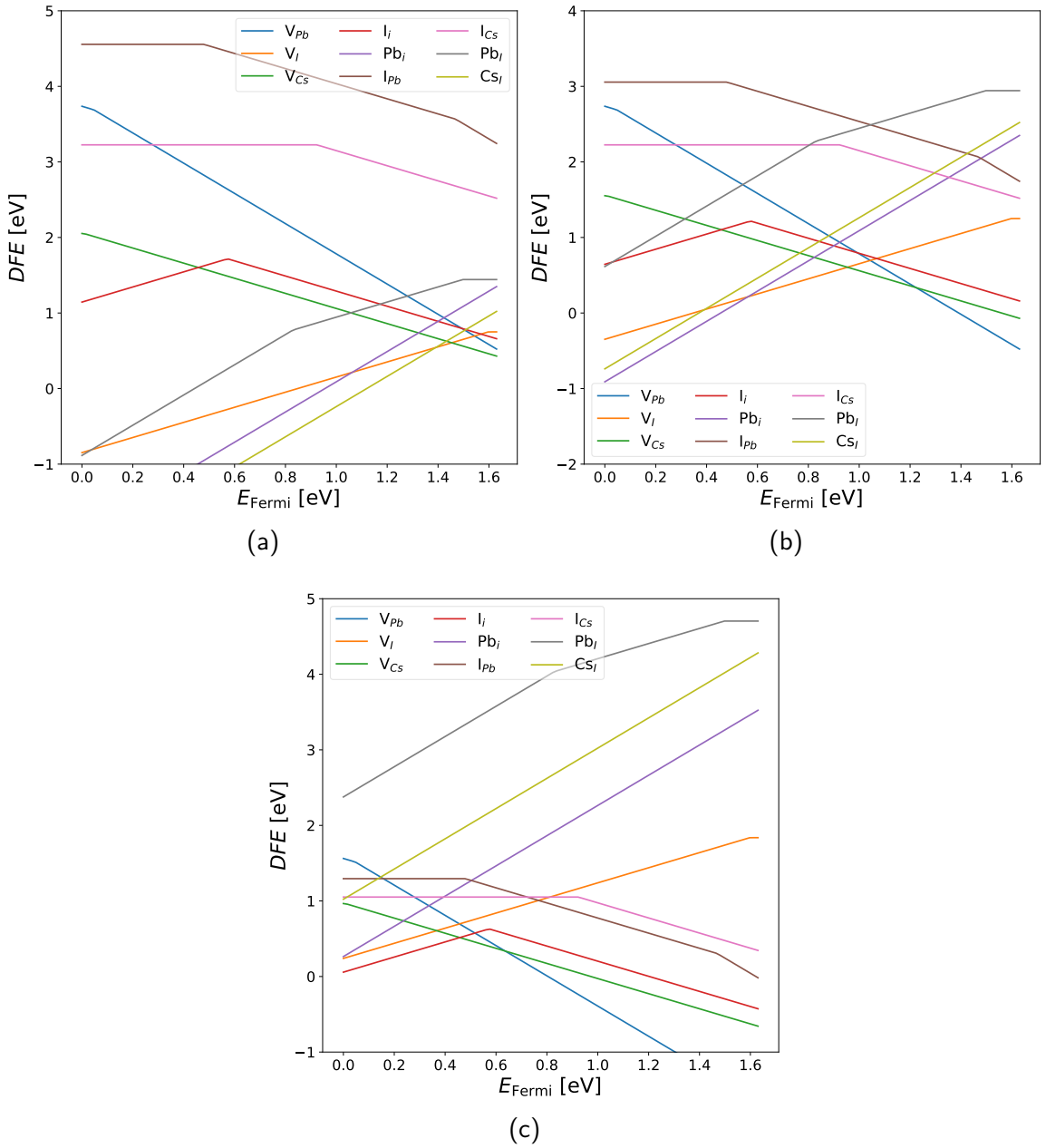

Figure 3.3: Calculated defect formation energies (DFE) versus Fermi level of native defects in $CsPbI_3$ under (a) Pb-rich (b) Pb-moderate and (c) Pb-poor condition, respectively.

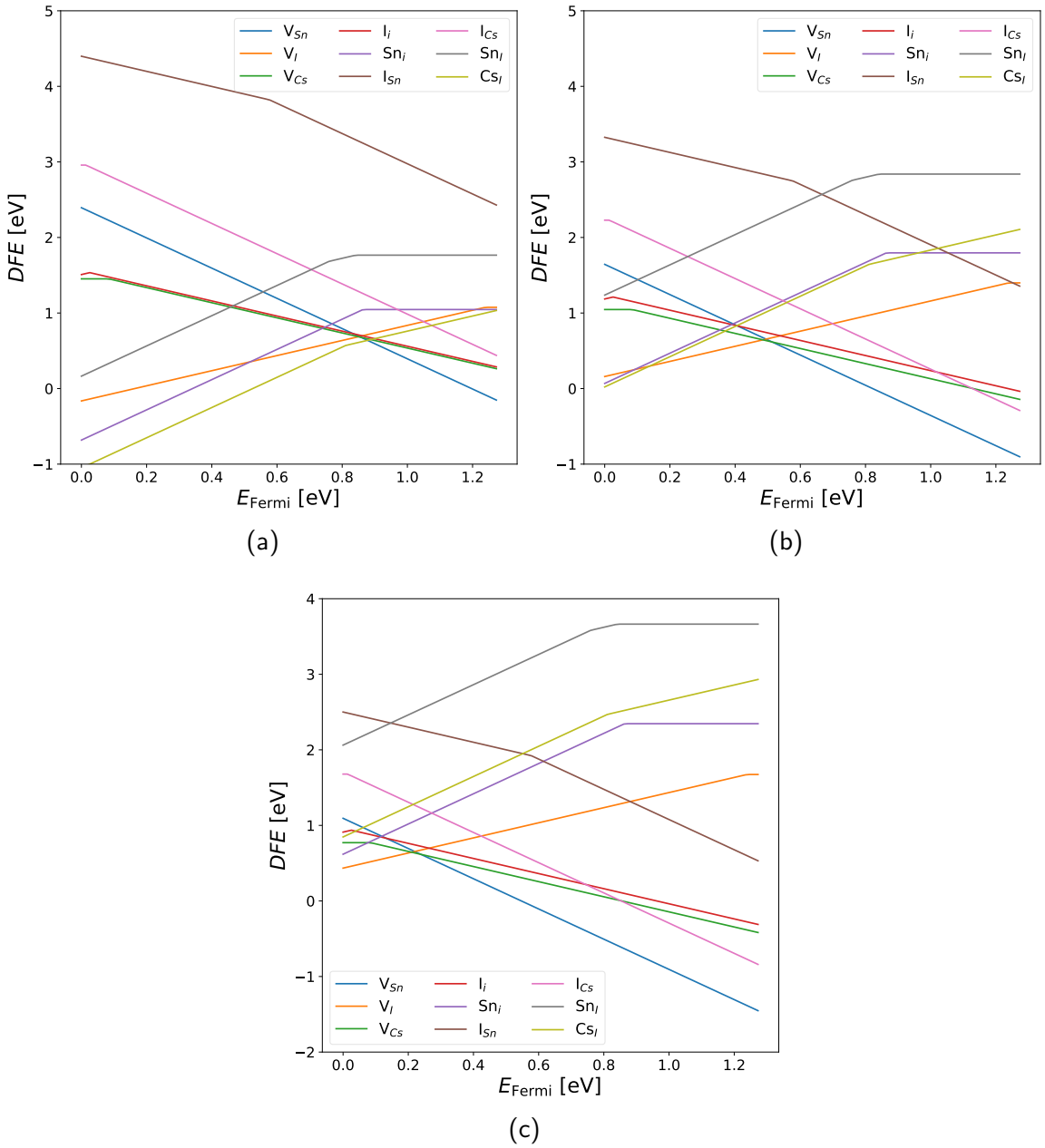

Figure 3.4: Calculated defect formation energies (DFE) versus Fermi level of native defects in $CsSnI_3$ under (a) Sn-rich (b) Sn-moderate and (c) Sn-poor condition, respectively.

3.2.1 $CsPbI_3$

For $CsPbI_3$, the defect formation energies (DFEs) of donor-type defects are found to be relatively low, particularly under Pb-rich conditions, resulting in high donor concentrations and an overall n-type character. This behavior is consistent with previous reports [95]. Reducing the chemical potential of Pb shifts the defect chemistry toward the intrinsic regime. Notably, the (+1/0) and (0/–1) charge transition levels of iodine interstitials (I_i), located 0.7641 eV below the conduction band minimum (CBM) and 0.3812 eV above the valence band maximum (VBM), respectively, are deep levels. This suggests that I_i can act as both a deep donor and a deep acceptor.

It is observed that both neutral and singly positively charged iodine interstitials (I_i^0 and I_i^{+1}) form iodine trimer-like configurations by breaking two Pb–I bonds and displacing toward the midpoint between neighboring iodine atoms. The formation of such trimer structures lowers the formation energies of these charge states and gives rise to deep defect levels. In contrast, analogous charge states of iodine interstitials in $CsSnI_3$ do not exhibit trimer-like bonding and correspondingly yield shallow transition levels.

The concentration of I_i in $CsPbI_3$ is found to be non-negligible under both Pb-moderate and Pb-poor conditions, indicating the potential for these defects to act as dominant deep traps. Additionally, the (+2/+1) transition level of Pb antisites (Pb_I) lies 0.8 eV below the CBM and is classified as a deep level. The concentration of Pb_I is particularly significant under Pb-rich conditions. Although the formation of I_i can be suppressed under such conditions, an enhancement in Pb_I formation is simultaneously promoted.

Under Pb-rich growth conditions, the $CsPbI_3$ absorber remains n-type, and as a result, hole capture by deep traps is expected to dominate Shockley–Read–Hall (SRH) non-radiative recombination. Given that the concentration of I_i remains appreciable even in the Pb-rich regime, the hole capture rates associated with I_i^0 and I_i^{-1} are of particular importance and need further investigation.

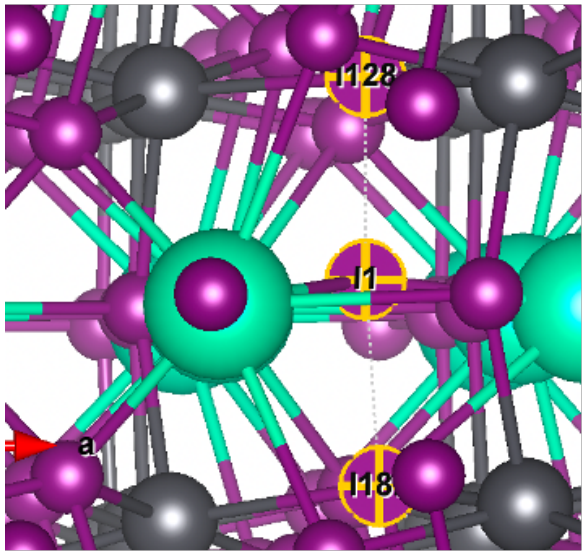

Figure 3.5: Local structure of Ii^{+1} in $CsPbI_3$.

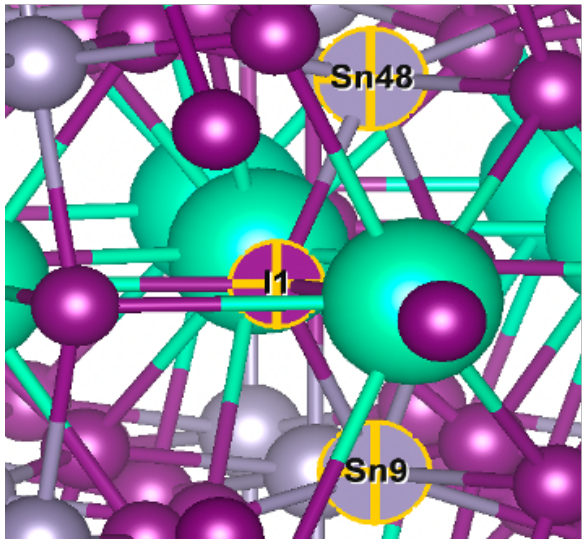

Figure 3.6: Local structure of Ii^{+1} in $CsSnI_3$.

3.2.2 $CsSnI_3$

For $CsSnI_3$, the material is found to be p-type under Sn-poor conditions due to the high concentration of acceptor defects, particularly tin vacancies, consistent with prior studies [98, 56]. Under Sn-rich and Sn-moderate conditions, $CsSnI_3$ exhibits near-intrinsic behavior, accompanied by an increased concentration of tin interstitials. These interstitials introduce deep defect levels, with (+1/0) and (+2/+1) charge transition levels located 0.441 eV and 0.133 eV below the conduction band minimum (CBM), respectively.

Analysis of the defect structures reveals that the number of Sn–I bonds associated with the interstitial Sn atom increases progressively from Sn_i^0 to Sn_i^{+1} and Sn_i^{+2}, indicating a preference for Sn–I bond formation as the positive charge state increases. In contrast, Pb interstitials (Pb_i) in $CsPbI_3$ are found to introduce only shallow levels.

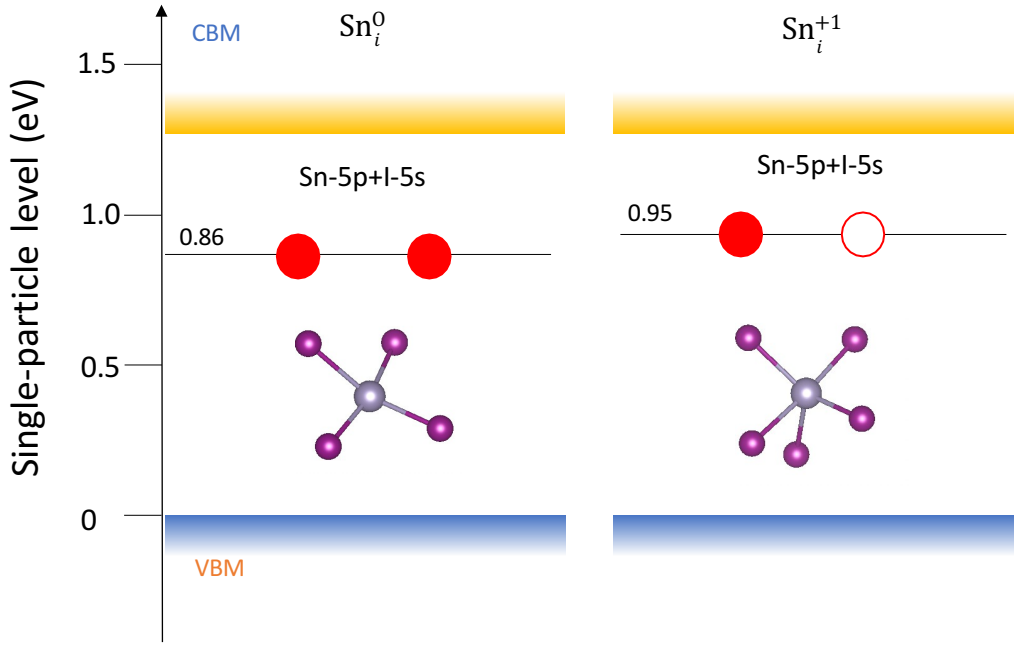

Figure 3.7: Single particle levels for Sn_i^0 and Sn_i^{+1}. Local defect structures are shown below the single particle levels.

Further investigation of the defect geometry of the nominal I_i^{-1} state in both perovskites shows that the Sn–I bond length (3.145 Å) is shorter than the Pb–I bond length (3.288 Å). Given that the nominal net charges of B-site and halide atoms are similar in both compounds, this difference suggests that Sn–I bonding is intrinsically stronger than Pb–I bonding, likely due to enhanced electrostatic attraction under shorter distance. This inference is consistent with the previously noted absence of iodine trimer-like structures for I_i^0 and I_i^{+1} in $CsSnI_3$.

On the other hand, acceptor defects with both deep energy levels and appreciable concentrations are not observed in $CsSnI_3$. As a result, it is concluded that the primary role of acceptors in this material is limited to enabling self-induced p-type doping.

3.2.3 Defect-assisted Carrier Capture Calculations

The rate of Shockley–Read–Hall (SRH) recombination induced by point defects can be calculated from first-principles methods, as introduced in 2.2.1.3. To evaluate whether deep levels significantly contribute to carrier trapping, the defect-assisted carrier capture coefficients of iodine interstitials in $CsPbI_3$ and tin interstitials in $CsSnI_3$ are calculated. This is accomplished by reconstructing one-dimensional configuration coordinate diagrams (CCDs), as shown in Fig. 3.8 and Fig. 3.9. A sufficient number of phonon eigenvalues are included (N=500) in order to guarantee convergence. Finite-size corrections to CCDs are implemented using the methodology proposed by Kumagai [47].

Table 3.4: Carrier capture rate of iodine interstitials in $CsPbI_3$ at 300K

Transition Level	$\Delta Q[amu^{1/2}\text{Å}]$	$C_n[cm^3s^{-1}]$	$C_p[cm^3s^{-1}]$
(0/-1)	30.90	$2.41 * 10^{-9}$	$3.34 * 10^{-7}$
(+1/0)	44.89	$1.33 * 10^{-8}$	$1.22 * 10^{-8}$

Based on the calculated results shown in Table 3.4 and Table 3.5, both iodine interstitials (I_i) in $CsPbI_3$ and tin interstitials (Sn_i) in $CsSnI_3$ exhibit strong carrier capture capabil-

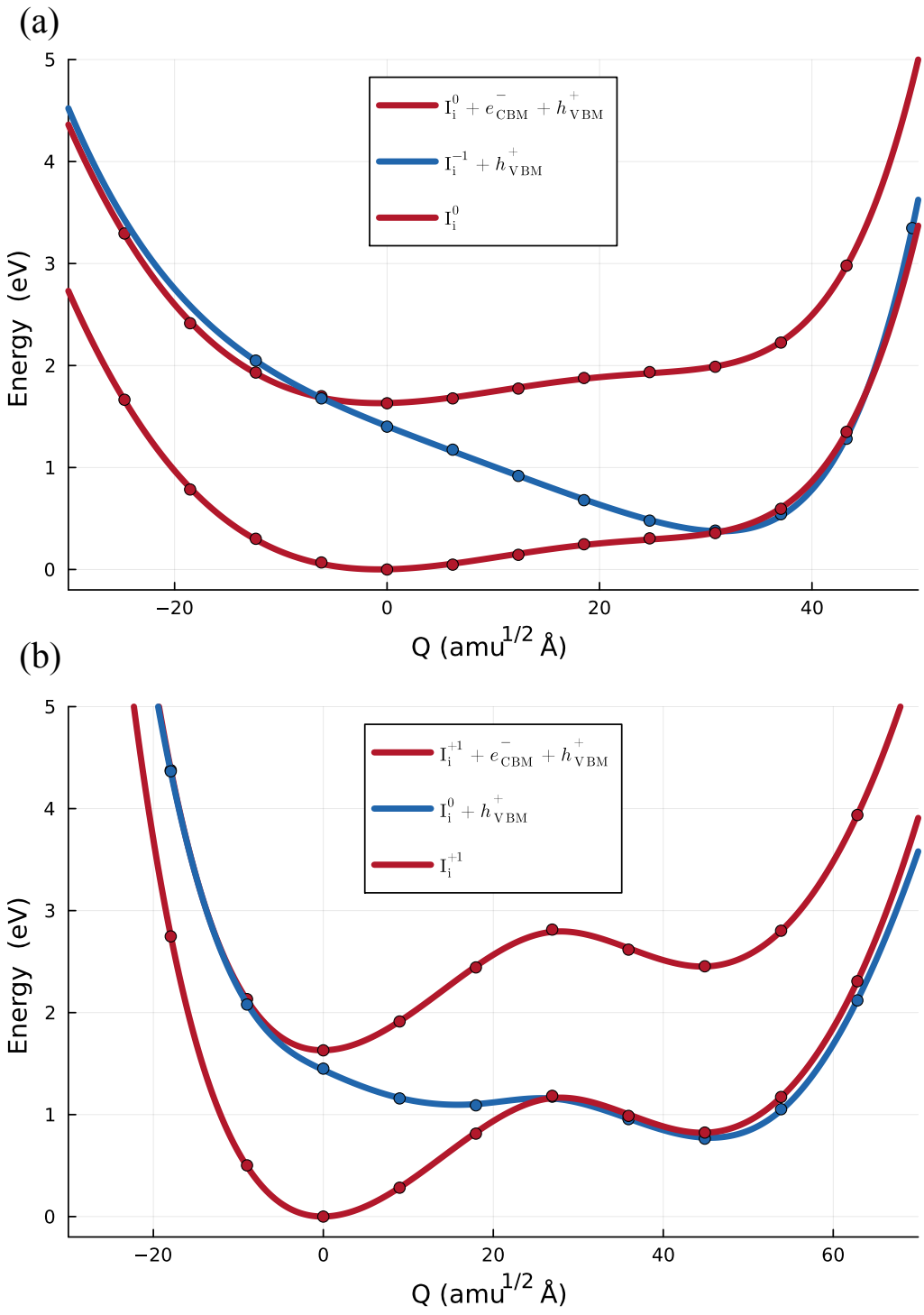

Figure 3.8: Calculated one-dimensional CCDs of (a) (0/-1) and (b) (+1/0) transition levels for iodine interstitials in $CsPbI_3$(360-atom supercell).

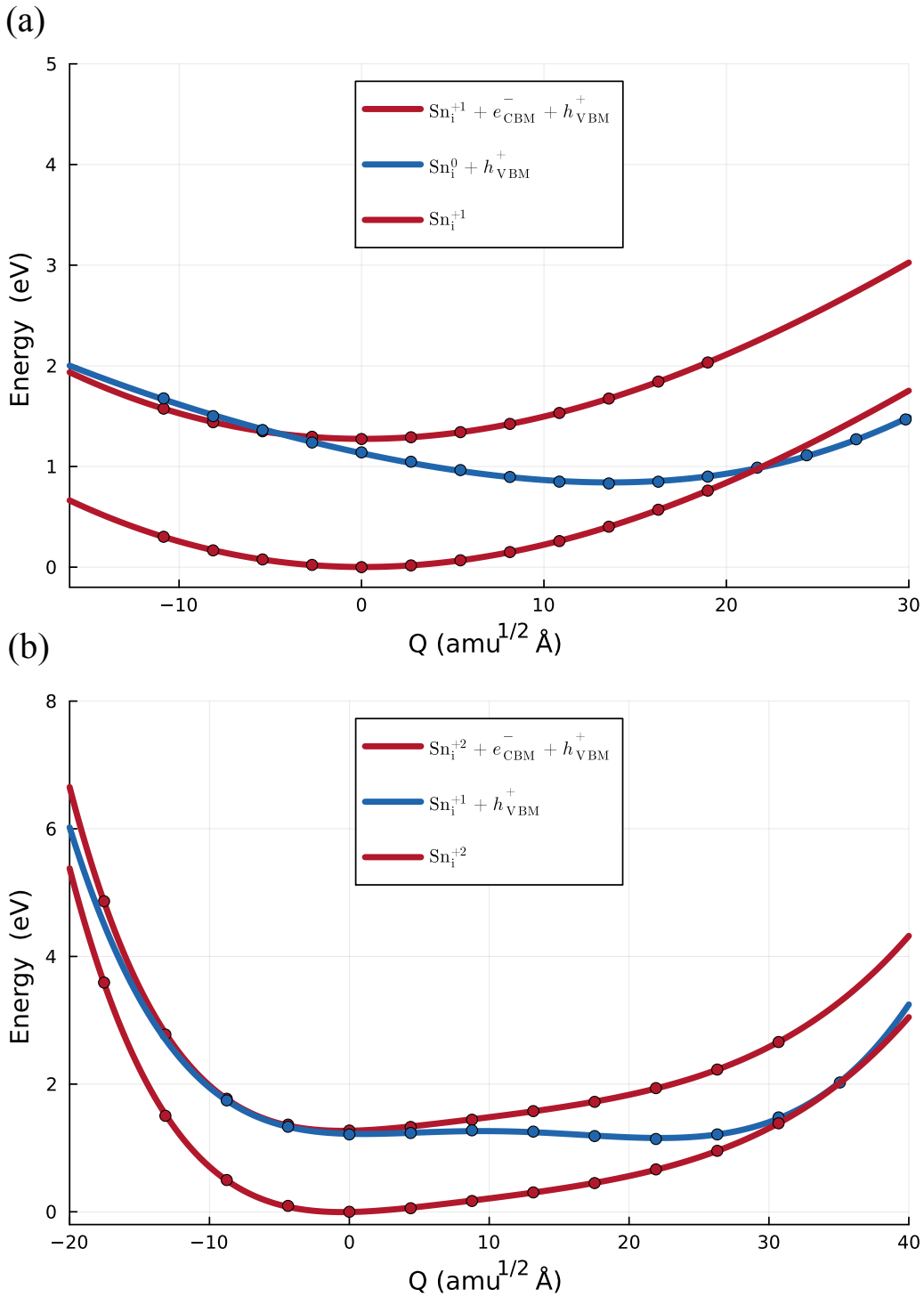

Figure 3.9: Calculated one-dimensional CCDs of (a) (+1/0) and (b) (+2/+1) transition levels for tin interstitials in $CsSnI_3$(360-atom supercell).

Table 3.5: Carrier capture rate of tin interstitials in $CsSnI_3$ at 300K

Transition Level	$\Delta Q[amu^{1/2}\text{Å}]$	$C_n[cm^3s^{-1}]$	$C_p[cm^3s^{-1}]$
(+1/0)	13.56	$7.10 * 10^{-6}$	$7.24 * 10^{-11}$
(+2/+1)	21.92	$2.83 * 10^{-5}$	$6.31 * 10^{-14}$

ities. In particular, the (0/–1) and (+1/0) transitions of I_i are associated with strongly anharmonic potential energy surfaces (PES) and large configuration coordinate differences (ΔQ). The similarity of the PES near the ground-state geometry of the excited states (depicted by the blue curves) indicates a strong overlap between phonon wavefunctions, which in turn leads to high hole capture rates. This behavior is especially detrimental in the case of an n-type $CsPbI_3$ substrate.

Table 3.6: $\Delta Q[amu^{1/2}\text{Å}]$ of (0/-1) and (+1/0) transitions for I_i in $CsPbI_3$

	80-atom cell	160-atom cell	360-atom cell	540-atom cell
(0/-1)	35.69	29.72	30.9	30.95
(+1/0)	14.16	45.15	44.89	44.93

It is noted that the calculated ΔQ values are significantly larger than those reported in previous studies [106]. This discrepancy is believed to arise primarily from differences in the size of the supercells used in defect calculations. To validate this hypothesis, ΔQ for the (+1/0) transition of I_i is calculated using supercells containing 80 (2×2×1), 160 (2×2×2), 360 (3×3×2), and 540 (3×3×3) atoms. As shown in Table 3.6, convergence within $0.05\text{amu}^{1/2}\text{Å}$ is achieved when the supercell size exceeds 360 atoms. In contrast, the 80-atom supercell yields significantly different ΔQ values, likely due to incomplete structural relaxation imposed by the limited cell size. Larger supercells allow atomic displacements farther from the defect site, resulting in more accurate relaxation and capture dynamics. This necessity is further illustrated by comparing Fig. 3.10 with Fig. 3.8(b), where the impact of supercell size on PES profiles is evident.

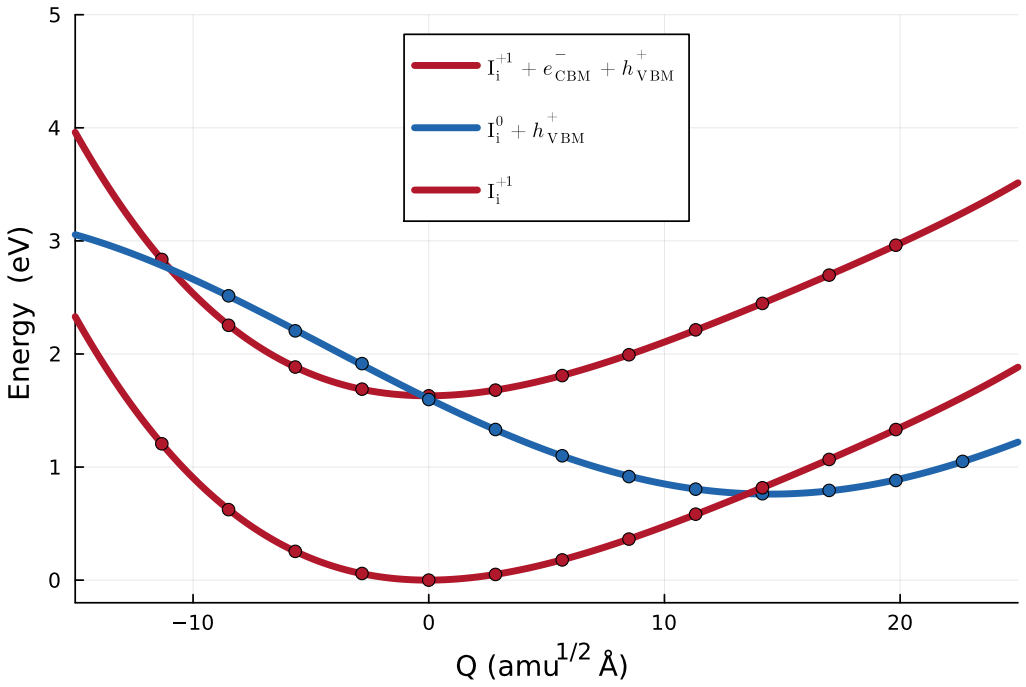

Figure 3.10: Calculated one-dimensional CCDs of (+1/0) transition level for iodine interstitials in $CsPbI_3$(80-atom supercell).

For Sn_i in $CsSnI_3$, the electron capture rates are found to exceed the hole capture rates, which poses a significant issue in p-type $CsSnI_3$, such as self-doped material grown under Sn-poor conditions. Although avoiding Sn-poor conditions may reduce the risk of forming SnI_4 [49] and decrease the background hole concentration, Sn-rich conditions promote the formation of tin interstitials, which introduce deep-level traps. This trade-off provides a possible explanation for the experimentally observed non-monotonic behavior in quantum efficiency as a function of SnF_2 additive concentration in tin-based perovskites [84].

3.2.4 3D-2D Hybrid Perovskites

Tin-based halide perovskites have emerged as promising lead-free alternatives for photovoltaic and optoelectronic applications, offering reduced toxicity and comparable optoelectronic properties to their lead-based counterparts. Among these, formamidinium tin iodide ($FASnI_3$) is a high-performance 3D perovskite with a suitable bandgap ($\sim$ 1.3 eV) and high absorption coefficient. However, its poor environmental stability and susceptibility to oxidation of Sn^{2+} to Sn^{4+} hinder practical deployment [25].

To address these challenges, compositional engineering has been used to partially replace FA cations with bulky organic phenethylammonium (PEA) cations, yielding the quasi-2D/3D mixed-cation perovskite $PEA_{0.2}FA_{0.8}I_3$. The incorporation of PEA forms low-dimensional (2D) Ruddlesden–Popper–type phases within the 3D matrix, which effectively passivate grain boundaries, suppress ion migration, and improve resistance to moisture and oxygen. This structural modulation preserves the favorable electronic transport properties of the 3D network while enhancing the overall film stability, enabling higher operational lifetimes and improved device performance in tin-based perovskite solar cells [49].

Tin vacancies have been identified as a major source of self-p-doping in tin halide perovskites. In addition to introducing shallow acceptor states, these vacancies promote the unwanted oxidation of lattice tin ions, which can ultimately lead to the formation of metallic tin phases. [49]. In this section, density functional theory (DFT) calculations are performed

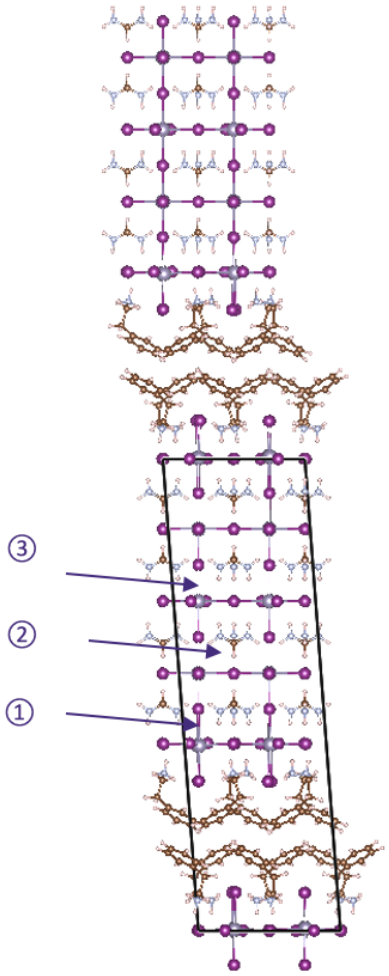

Figure 3.11: Structure of 3D-2D hybrid perovskite $PEA_{0.2}FA_{0.8}I_3$. Labels in the figure (1-3) indicates the possible positions of tin vacancies.

on the 3D–2D structured $PEA_{0.2}FA_{0.8}I_3$ and on tin vacancies located at different lattice sites, in order to elucidate the mechanisms by which this architecture enhances the stability of tin-based perovskites.

As shown in Fig. 3.11, a Ruddlesden–Popper–structured $PEA_{0.2}FA_{0.8}I_3$ model with 5 Sn-I layers (n=5) is constructed and fully relaxed using DFT. Three distinct tin sites are then selected as candidates for introducing tin vacancies, with each configuration calculated individually using VASP. Among the three configurations, the tin vacancy at site 1 is found to have the highest formation energy, while that at site 3 possesses the lowest, suggesting a site-dependent stability of vacancy formation. Specifically, the formation energy of the tin vacancy at site 1 is 0.96 eV higher than at site 3. This substantial increase in vacancy formation energy at the interface indicates effective passivation through PEA incorporation. Consequently, the severe self-p-doping commonly observed in bulk tin perovskites—and the associated strong Burstein–Moss effect [23]—is expected to be mitigated near the interface, leading to a red-shift in the photoluminescence (PL), as shown in Fig. 3.12. The enhanced PL observed at the interface further demonstrates the effectiveness of PEA passivation, as it suppresses non-radiative recombination pathways.

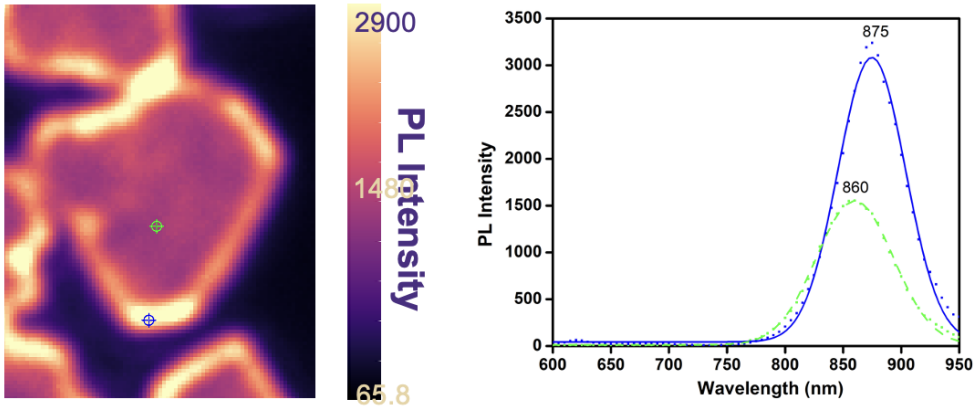

Figure 3.12: Spatially resolved PL and spectrally resolved PL for bulk region (green) and interface region (blue) (data courtesy of Dr. Robert Westbrook, unpublished).

Chapter 4

MULTI-SCALE MODELING OF DEFECT-RELATED PROPERTIES IN CDTE/CDSETE PHOTOVOLTAICS

Cadmium telluride (CdTe) and its selenium-alloyed counterpart (CdSeTe) have attracted considerable attention for optoelectronic applications, particularly in solar cells and radiation detectors. The incorporation of selenium into CdTe not only enables bandgap tuning but also leads to notable improvements in key electronic properties, such as carrier lifetime and mobility, thereby enhancing the potential for high-efficiency photovoltaic performance [15].

Despite these advantages, the presence of native point defects and defect complexes continues to pose a significant challenge, as they can profoundly influence both the electrical and optical behavior of the material. In particular, such defects may introduce mid-gap states that facilitate non-radiative recombination or act as compensating centers, limiting carrier transport and device efficiency. To elucidate the role of these defects, a detailed investigation into their formation energies, charge transition levels, and recombination dynamics within CdSeTe is essential. A comprehensive understanding of these defect-related phenomena is critical for optimizing material quality and advancing device performance.

In this chapter, selected intrinsic point defects and group V dopants in CdTe/CdSeTe are investigated using density functional theory (DFT) calculations. Particular emphasis is placed on the impact of these defects on the electronic properties of CdTe and CdSeTe absorbers. Density derived electrostatic and chemical (DDEC) method is applied as a helpful tool for analyzing proper finite-size charge cell corrections. Intrinsic defects that are widely recognized as important are included, such as V_{Cd} [104, 39], V_{Te} [102, 72], Cd_{Te} [102, 72], Te_{Cd} [102, 70], Cd_{int} [102] and Te_{int} [39, 102, 35]. For group V dopants such as arsenic and phosphorus, both conventional substitutional defects and compensating AX

center configurations are examined. In addition, defect complexes including $(Cd_{int}+As_{Te})^{+}$ and $(V_{Te}+As_{Te})^{+}$ are also investigated, as significant Coulombic attraction may arise between As_{Te}^{-1} and Cd_{int}^{2+} or V_{Te}^{2+}.[1]

4.1 First-principles Study of Point Defects in CdTe/CdTeSe

4.1.1 Methods

Benchmarking the bandgap and lattice parameters of a material is a critical preliminary step for ensuring the reliability of defect property calculations. In the case of CdTe, the use of the traditional generalized gradient approximation (GGA) for the exchange–correlation functional yields a bandgap of approximately 0.68 eV, which is significantly lower than the experimental value. This underestimation is attributed to the known limitations of GGA in describing the localized nature of Cd-d electrons. As a result, an exaggerated anti-bonding interaction between Cd-d and Te-p orbitals is produced, leading to an upward shift of the valence band maximum (VBM) [94]. Such inaccuracies highlight the necessity of adopting bandgap correction methods when modeling electronic and defect-related properties in CdTe and related materials.

The hybrid functional developed by Heyd, Scuseria, and Ernzerhof (HSE) [104] is widely recognized for its ability to mitigate common errors in traditional density functional theory (DFT), such as the self-interaction problem. However, the use of HSE is computationally demanding, which limits its applicability to relatively small supercells. This constraint not only poses challenges for accurate defect calculations—where large supercells are often required to minimize finite-size effects—but also hinders extensive studies in compositionally complex or alloyed systems. To address the limitations of both standard GGA and the high computational cost of hybrid functionals, the GGA+U method has been widely adopted as a practical alternative. In this approach, an effective Hubbard U correction is applied to

[1]This section is adapted from our publication: Xiaofeng Xiang, Yijun Tong, Aaron Gehrke and Scott Dunham. Point defects in CdTe and CdTeSe alloy: A first principles investigation with DFT+U, Physical Review Materials, 2024, 8(8), 084602.

localized orbitals—typically d or f states—to better account for on-site Coulomb interactions and reduce self-interaction errors. By improving the treatment of electron localization, GGA+U enables more accurate predictions of electronic structure and defect energetics, while maintaining computational efficiency suitable for large supercell calculations.

To begin with, a series of effective Hubbard U values are applied, and CdTe unit cells are fully relaxed without symmetry constraints. All calculations are performed using a plane-wave energy cutoff of 450 eV for the wavefunctions. Collinear spin polarization is included in all simulations. The resulting bandgap values and lattice parameters are extracted and summarized in Fig. 4.1. An optimized effective value of $U = 12.2$ eV is identified, which provides good agreement with experimental measurements for both the bandgap and lattice parameter [16]. In contrast, although the HSE functional yields an accurate bandgap, the corresponding lattice parameter is significantly overestimated. Based on this evaluation, a U value of 12.2 eV is applied to the Cd-4d orbitals in all subsequent defect calculations.

4.1.2 Results and Discussions

4.1.2.1 Intrinsic Defects

The cadmium vacancy (V_{Cd}) is recognized as a key intrinsic defect in CdTe and its related alloys, with its geometric configurations and charge transition levels being extensively debated in both theoretical and experimental literature [104]. In this study, it is found that the neutral charge state of V_{Cd} preferentially adopts a C_{2v} symmetry configuration, characterized by a dimer-like structure with two fully occupied degenerate states and one unoccupied state. In contrast, the negatively charged states (V_{Cd}^{-1} and V_{Cd}^{-2}) are found to be most stable in a T_d symmetry configuration. Reported charge transition levels for V_{Cd} span a wide energy range from approximately 0.1 to 0.8 eV above the valence band maximum (VBM), as established across multiple theoretical and experimental studies [9, 88, 7, 31]. It is possible that either supercells that are not large enough were used for simulation, or inappropriate methods were used for charged-cell correction. The charge transition levels

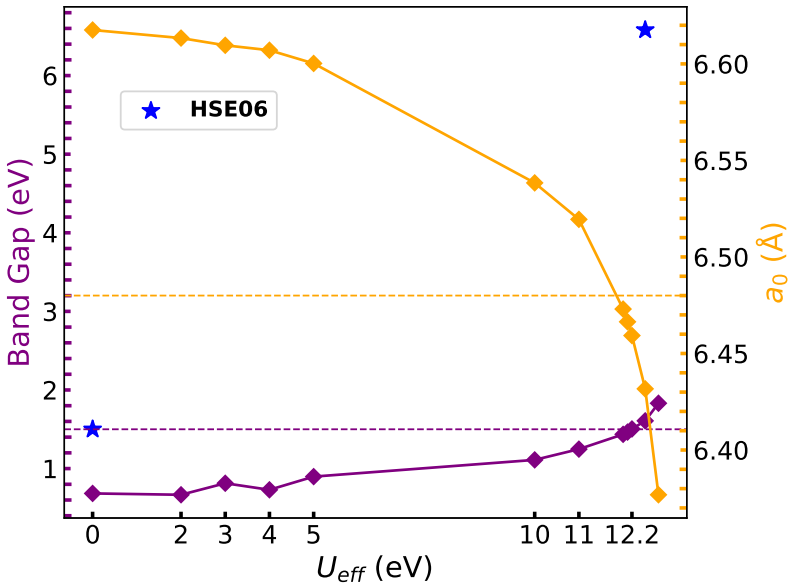

Figure 4.1: The dependence of the lattice parameter a_0 and bandgap on the applied Hubbard U parameter is shown for different methods, including standard DFT ($U = 0$ eV) and GGA+U. HSE06 results are indicated by star symbols, while experimental reference values are marked by dashed lines.

of V_{Cd} in CdTe are determined to be 0.17 eV for the (–1/0) transition and 0.30 eV for the (–2/–1) transition.

The nonradiative carrier capture behavior of V_{Cd} in CdTe is further examined through calculations of defect carrier-capture cross sections based on single-phonon mode approximation [1]. As shown in Fig. 4.2 and Table 4.1, the potential energy surface (PES) associated with the (–2/–1) transition exhibits a quasi-harmonic profile, while the PES of the (–1/0) transition displays pronounced anharmonicity. This contrast is attributed to the close geometric proximity between the T_d structured V_{Cd}^{-2} and V_{Cd}^{-1}, while large discrepancy in geometry between V_{Cd}^{-1} and V_{Cd}^{0}. Similar behavior has been reported in previous studies employing the HSE06 functional for V_{Cd} in CdTe [31]. Carrier capture cross section calculations indicate that the (–1/0) transition is associated with strong nonradiative recombination activity, while the (–2/–1) transition contributes only weakly to nonradiative

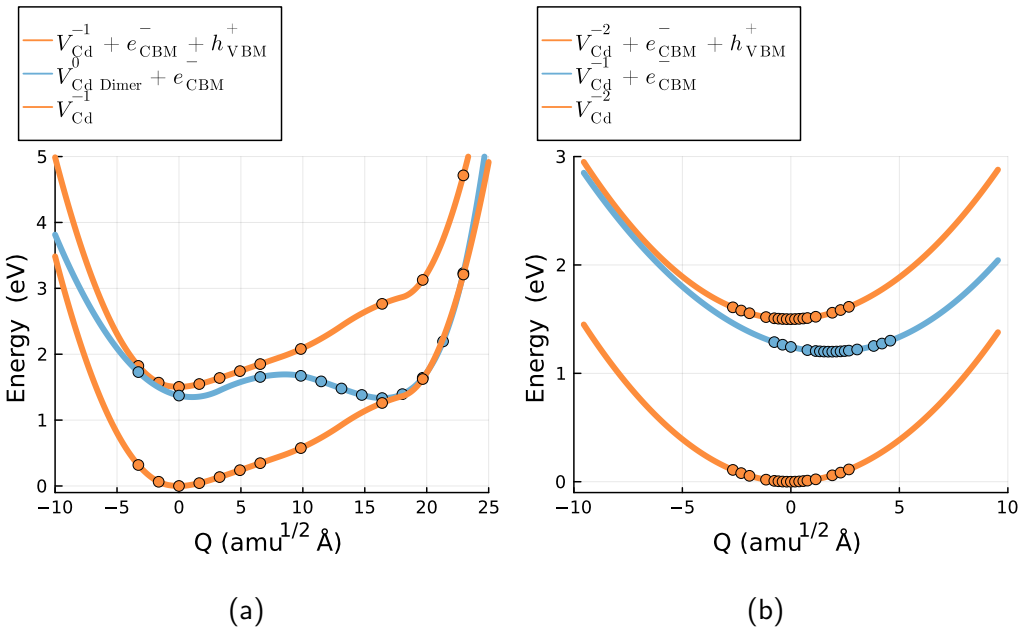

Figure 4.2: Configuration Coordinate Diagram of V_{Cd} (-1/0) and (-2/-1). Q in X-axis corresponds to the mass-weighted configuration coordinate. Q indicates the configurational coordinate path between equilibrium configurations. $Q = 0$ indicates defects ground state with T_d symmetry.

processes.

The second intrinsic defect examined in this study is the tellurium-on-cadmium antisite (Te_{Cd}), which is expected to form with appreciable concentration under Cd-poor growth conditions. Structural analysis reveals that the Te_{Cd}^{0} and Te_{Cd}^{+} charge states adopt a C_{3v} symmetry, whereas the doubly positively charged state Te_{Cd}^{2+} stabilizes in a T_d configuration. Both the (0/+1) and (+1/+2) charge transition levels are located deep within the bandgap, indicating the potential for strong nonradiative recombination activity. To confirm this, nonradiative carrier capture cross sections are computed, with the results summarized in Table 4.1. The findings confirm that Te_{Cd} introduces deep-level trap states capable of acting as efficient nonradiative recombination centers. Previous theoretical studies have reported differing results [39, 31]. For example, Krasikov *et al.* obtained carrier

capture cross sections for Te_{Cd} that are comparable to ours, but their results for V_{Cd} deviate significantly [39]. This discrepancy arises from their use of an approximate harmonic configuration–coordinate diagram (CCD) for carrier capture calculations, rather than a fully anharmonic profile, leading to strong deviations from physical reality. Kavanagh *et al.* also employed an anharmonic CCD approach, but their calculations for the neutral V_{Cd} defect produced a strongly distorted structure, even though it exhibited the same C_{2v} symmetry as in our results [31]. This discrepancy is likely due to their use of a relatively small 64-atom supercell, which can lead to inaccurate geometric relaxation and electronic occupation. Furthermore, their use of the Lany–Zunger correction scheme for charged supercells may be problematic, as this method has known deficiencies in accurately treating the potential alignment term [34].

Table 4.1: Capture cross section of deep level defects in CdTe at 300K

Defect	Transition Level	Trapping Process	$\sigma(T = 300K)[cm^2]$
V_{Cd}	(-2/-1)	hole capture	8.0×10^{-17}
		electron capture	1.9×10^{-20}
V_{Cd}	(-1/0)	hole capture	2.8×10^{-16}
		electron capture	2.1×10^{-15}
Te_{Cd}	(+2/+1)	hole capture	2.1×10^{-18}
		electron capture	1.0×10^{-15}
Te_{Cd}	(+1/0)	hole capture	3.3×10^{-15}
		electron capture	8.1×10^{-18}

The defects V_{Te}, Cd_{int}, and Cd_{Te} are identified as shallow donors, as shown in Fig. 4.3. Both V_{Te} and Cd_{Te} exhibit negative-U behavior, meaning the density of +1 charge state is insignificant compared to neutral and +2 charge state in equilibrium. The (+2/0) transition levels of V_{Te} and Cd_{Te}, along with the (+2/+1) level of Cd_{int}, are located very close to the conduction band minimum (CBM) or even inside the conduction band (CB). As a result, the +2 charge state is dominant for all three defects under p-type conditions in CdTe and its alloys.

Among the three, Cd_{Te} has the highest formation energy in both Cd-rich and Te-rich

environments, suggesting it is unlikely to be the main compensating donor. The neutral state of V_{Te} is most stable in a Jahn–Teller distorted structure, consistent with results from previous HSE06 calculations [104]. The +2 charge state of V_{Te} prefers a symmetric T_d configuration, while Cd_{int}^{+2} is most stable when located in a tetrahedral site surrounded by four Te atoms.

The interstitial tellurium defect (Te_{int}) nominally acts as a donor. Previous studies have reported that Te_{int} tends to form a split-interstitial configuration oriented along the [110] direction [59]. Previous reports have proposed that Te_{int} may act as a deep-level defect [58], and the results in this study indeed confirm that its charge transition level lies close to the middle of the bandgap, as shown in Fig. 4.3. However, its formation energy is relatively high, even under Te-rich growth conditions. Using the formation energy values together with the compositionally constrained thermodynamic (CCT) model [66], the concentration of Te_{int} at 300 K under Te-rich conditions is estimated to be roughly three orders of magnitude lower than both the free carrier density and the concentrations of the two other major deep-level defects, Te_{Cd} and V_{Cd}. This low concentration suggests that Te_{int} is unlikely to play a significant role in limiting carrier lifetime in CdTe.

The tellurium-on-cadmium antisite defect (Te_{Cd}) has been reported to potentially form stable complexes with interstitial tellurium (Te_{int}) and cadmium vacancies (V_{Cd}) due to their favorable binding energies [38]. However, the results of this study indicate that the formation energies of both Te_{Cd}–Te_{int} and Te_{Cd}–V_{Cd} complexes remain high. This is attributed to the binding energies being insufficient to offset the energetic cost of creating both constituent defects. Using the compositionally constrained thermodynamic (CCT) approach, the concentrations of these complexes at 300 K are estimated to be approximately three orders of magnitude lower than the carrier density, suggesting they are unlikely to play a significant role in determining the electronic properties of CdTe. Process simulation also shows that after cooling from growth temperatures the concentrations of these complexes are negligible [96].

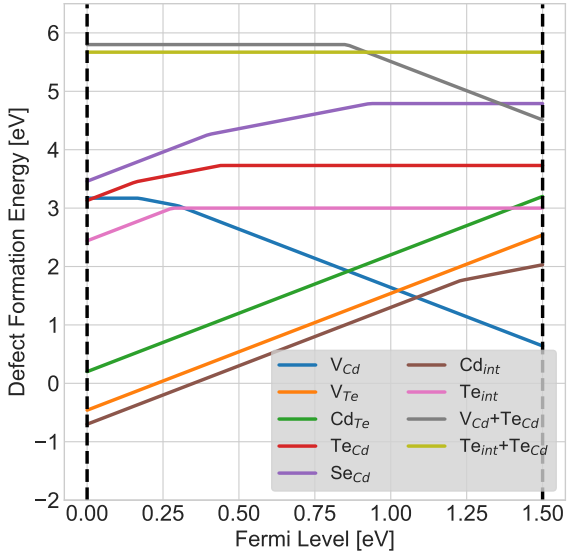

(a)

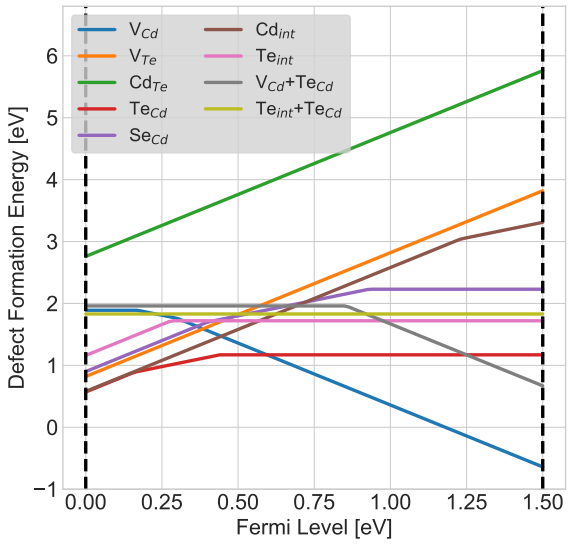

(b)

Figure 4.3: Defect formation energies vs Fermi level of intrinsic defects in CdTe under (a) Cd-rich and (b) Te-rich condition. The chemical potential conditions are $\mu_{Cd}+\mu_{Te} = -1.28$ eV and $\mu_{Cd} + \mu_{Se} < 0.15$ eV.

4.1.2.2 Group V Dopants

Arsenic (As) and phosphorus (P) are recognized as effective dopants in CdTe-based materials, with demonstrated potential for improving p-type conductivity in photovoltaic devices [103]. However, their behavior in CdTe and CdSeTe—particularly the dominant compensating mechanisms in As- and P-doped systems—remains less well understood [10].

In CdTe and CdSeTe, As and P can substitute for Te or Se atoms, functioning as acceptors due to their group V valence, which provides one fewer valence electron compared to Te. In this study, attention is focused on the substitutional defects As_{Te} and P_{Te}, along with their associated defect complexes. The calculations reveal that the neutral and singly negatively charged states of both As_{Te} and P_{Te} adopt T_d symmetry, in agreement with earlier theoretical reports [103]. The (0/–1) charge transition levels are computed to be 0.13eV for As_{Te} and 0.18eV for P_{Te} (Table 4.2, Table 4.3), confirming their character as shallow acceptors capable of enabling effective p-type doping in CdTe.

In addition to the negatively charged states, As and P can also form singly positively charged substitutional defects, As_{Te}^{+1} and P_{Te}^{+1}, commonly referred to as AX centers [103, 35]. Unlike their negatively charged counterparts, AX centers act as donors. As illustrated in Fig.4.4, the AX configuration arises when the As or P atom displaces toward one of the neighboring Te atoms, thereby breaking the original T_d symmetry. This distortion splits the triply degenerate defect states associated with the T_d configuration into two fully occupied states and one empty state, as shown in Fig.4.5. Structurally, the displacement results in the breaking of one Cd–As/P bond for each of the two affected atoms.

The energetic stability of the AX center is governed by the competition between the band splitting energy, $\Delta E_{\mathrm{split}}$, and the Cd–As/P bond energy, E_{bond}. When $\Delta E_{\mathrm{split}}$ exceeds E_{bond}, the AX configuration is expected to be more stable than the ideal tetrahedral structure. However, the present calculations indicate that, in CdTe, the formation energy of the As AX center (1.92eV) is nearly identical to that of the T_d-structured As_{Te}^{+1} defect (1.93eV). Similarly, the P AX center has a formation energy of 2.04eV, which is close

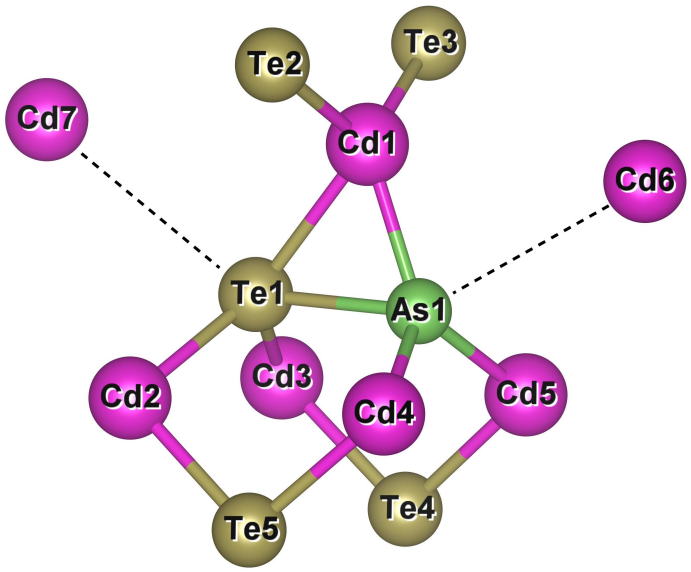

Figure 4.4: Schematic of AX center defect configuration

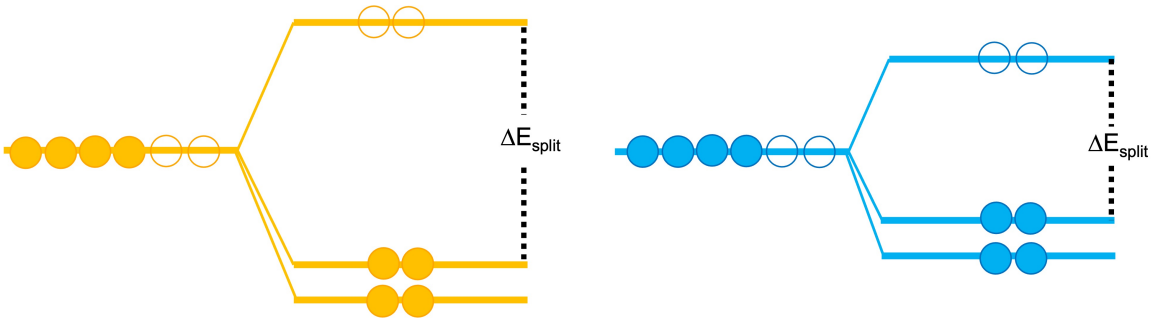

Figure 4.5: Schematic of AX center defect band splitting. Left one indicates AX in CdTe and right one indicates AX in $CdSe_{0.25}Te_{0.75}$. $\triangle E_{split}$ is the band splitting energy

to the value for T_d-structured P_{Te}^{+1} (2.10eV). These results suggest that in CdTe the AX configuration does not confer a significant stability advantage over the regular tetrahedral substitutional geometry.

An open question in the study of compensating donors in CdSeTe is whether species other than the AX center could dominate compensation. Chatratin *et al.* [10] proposed that V_{Te} and Cd_{Te} may act as compensating donors, while Cd_{int} was excluded from consideration

Table 4.2: Arsenic defect formation energy and complex binding energy (eV) in $CdSe_xTe_{1-x}$.

	As_{Te}^{+1} AX	As_{Te}^{+1} T_d	As_{Te}^{0}	As_{Te}^{-1}	(-1/0)	$E_{binding}$ $(Cd_{int} + As_{Te})^+$	$E_{binding}$ $(V_{Te} + As_{Te})^+$
CdTe	1.92	1.93	1.94	2.07	0.13	1.21	0.55
$CdSe_{0.25}Te_{0.75}$	1.57∼1.79	1.89	1.93	2.11	0.18	1.32	0.37
$CdSe_{0.50}Te_{0.50}$	1.70∼1.87	1.84	1.87	2.19	0.31	1.35	0.47

Table 4.3: Phosphorus defect formation energy and complex binding energy (eV) in $CdSe_xTe_{1-x}$.

	P_{Te}^{+1} AX	P_{Te}^{+1} T_d	P_{Te}^{0}	P_{Te}^{-1}	(-1/0)	$E_{binding}$ $(Cd_{int} + P_{Te})^+$	$E_{binding}$ $(V_{Te} + P_{Te})^+$
CdTe	2.04	2.10	1.93	2.04	0.11	1.14	0.35
$CdSe_{0.25}Te_{0.75}$	1.72∼1.94	2.08	2.05	2.09	0.04	1.31	0.31
$CdSe_{0.50}Te_{0.50}$	1.82∼2.01	2.10	2.07	2.13	0.06	1.31	0.38

due to its high mobility. However, the possibility of Cd_{Te} being the primary compensating donor appears limited, as its formation energy is relatively high [67, 97]. Based on these considerations, V_{Te} and Cd_{int} are regarded as the more probable dominant compensating defects in CdSeTe.

Although the high mobility of Cd_{int} raises concerns regarding its stability as an isolated defect, the present results indicate that Cd_{int}^{+2} can form stable complexes with As_{Te}^{-1} or P_{Te}^{-1} through electrostatic attraction and/or covalent bonding. These interactions lead to the formation of $(Cd_{\mathrm{int}} + As_{\mathrm{Te}})^+$ (Fig. 4.6) and $(Cd_{\mathrm{int}} + P_{\mathrm{Te}})^+$ complexes. The relatively high binding energies of these complexes, as summarized in Table 4.2 and Table 4.3, suggest that they could be important contributors to compensation in CdSeTe. While Group V acceptors also exhibit measurable binding with V_{Te}, the binding energies in these cases are significantly smaller than those observed for complexes with Cd_{int}. Consequently, $(V_{\mathrm{Te}} + As_{\mathrm{Te}})^+$ and $(V_{\mathrm{Te}} + P_{\mathrm{Te}})^+$ are considered less likely to be the dominant compensating donors in the material.

4.1.2.3 Defect Properties in CdSeTe Alloy

Defect properties and energetics in CdSeTe alloys can differ from those in pure CdTe. Key findings on this topic, based on our earlier work [97], are summarized here.

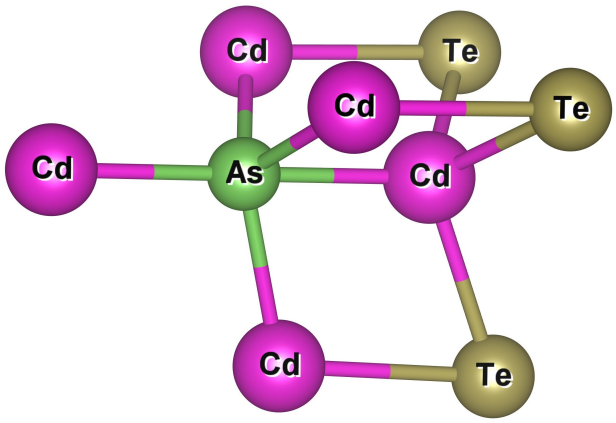

(a)

Figure 4.6: Defect Structure of $(Cd_{int} + As_{Te})^{+}$ in CdTe.

Experimental studies have reported that bulk recombination in CdSeTe alloys is reduced compared to CdTe [3, 36]. Consistent with these observations, our calculations show that the formation energies of the two primary deep-level defects—Te_{Cd} and V_{Cd}—increase slightly with selenium incorporation (Se fraction increasing from 0% to 50%). Specifically, the formation energy of V_{Cd}^{0} is 0.15eV higher in the 50% alloy, while that of Te_{Cd}^{+2} is 0.18eV higher. These increases suggest a reduced concentration of deep-level centers in CdSeTe. Taken together, these effects imply that bulk recombination rates are expected to be lower in CdSeTe alloys compared to pure CdTe.

In CdSeTe alloys doped with group V elements, the (0/–1) charge transition level of As_{Te} is found to shift toward the conduction band minimum (CBM) with increasing Se content, reaching 0.31 eV above the valence band maximum (VBM) at a Se ratio of 50%. In contrast, the transition level of P_{Te} remains close to the VBM across the same composition range. These results indicate that, for As-doped CdSeTe, precise control of the Se ratio is required to sustain high doping efficiency.

The singly positively charged As_{Te}^{+1} defect in CdSeTe also exhibits a noticeable depen-

dence on the Se alloying ratio. For the T_d-structured configuration, the formation energy is calculated to be 1.93 eV in CdTe, 1.89 eV in $CdSe_{0.25}Te_{0.75}$, and 1.84eV in $CdSe_{0.50}Te_{0.50}$, indicating a slight energetic preference for the T_d +1 defect at higher Se content. In contrast, the formation energy of the AX-centered As_{Te}^{+1} decreases more significantly with increasing Se ratio. For example, in $CdSe_{0.25}Te_{0.75}$, the AX defect formation energy ranges from 1.57eV to 1.79eV depending on the specific Se/Te arrangement, compared to 1.92eV in CdTe. This trend suggests that the presence of Se may stabilize the AX configuration, potentially lowering its formation energy and thus enhancing compensation of p-type doping. As shown in Fig. 4.5, this stabilization is not attributed to an increase in the band splitting energy $\Delta E_{\mathrm{split}}$, but rather to a local bonding effect in which a nearby Se atom weakens the Cd–As/Te bond. Evidence for this is provided by calculations on a 64-atom CdSeTe supercell containing only one Se atom in the group VI sublattice, where the lowest AX formation energy occurs when the Se atom occupies either the Te4 or Te5 position. From Fig. 4.4, it can be seen that placing the smaller Se atom at these sites compresses the nearby Cd atoms along the As1–Te1 direction, thereby strengthening the As1–Te1 bond but weakening the As1–Cd6 and Te1–Cd7 bonds. Furthermore, in the alloy environment, the As atom tends to move toward the Te atom to form a dimer-like structure, whereas movement toward the Se atom is energetically unfavorable. A similar trend is observed for P_{Te} defects.

To further assess the influence of AX center defects on group V dopability, the transition mechanism between the AX configuration and the neutral As_{Te} substitutional defect was examined in a 25% CdSeTe alloy. The configuration coordinate diagram (CCD) for the As_{Te} (+1_AX/0) transition is shown in Fig.4.7. A barrier of approximately 0.4 eV is found between the AX- and T_d-structured As_{Te}^{+1} states, which is likely to limit the formation of AX defects. This finding is consistent with similar transition barriers reported for CdTe [35]. Although certain alloy configurations may favor AX defect formation, the overall concentration of AX centers is expected to remain low due to this transition barrier. Recent computational studies [10] also have suggested that AX centers are not the primary bottle-

neck for achieving p-type doping in CdTe or CdSeTe alloys. Nevertheless, their potential impact on group V dopability warrants further study, with attention to both the kinetic and thermodynamic factors governing AX defect formation.

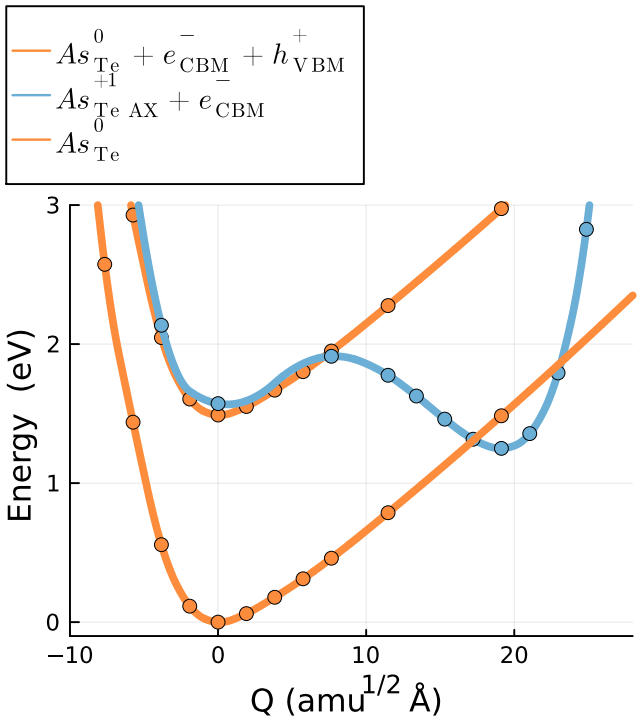

Figure 4.7: Configuration coordinate diagram of As_{Te} (+1_AX/0) in $CdSe_{0.25}Te_{0.75}$. As^{+}_{Te} with formation energy close to the Boltzmann distribution at 300 K is selected as the excited state. As^{0}_{Te} exhibits minimal dependence on the Se/Te arrangement.

For complexes in CdSeTe, the bonding between Cd^{+2}_{int} and As^{+1}_{Te} or P^{+1}_{Te} was analyzed in detail, as summarized in Table 4.4. The table lists the bond lengths (in ångströms, Å) and bond orders (BO) for the nearest-neighbor atoms surrounding Cd interstitials within $(Cd_{\mathrm{int}} + As_{\mathrm{Te}})^{+}$ and $(Cd_{\mathrm{int}} + P_{\mathrm{Te}})^{+}$ complexes in both CdTe and CdSeTe alloys. The BO values, estimated using the density-derived electrostatic and chemical (DDEC) method [61],

range from 0 (purely ionic bond) to 1 (purely covalent bond). The results show that Cd–Te, Cd–Se, Cd–As, and Cd–P bond lengths decrease slightly as the Se alloy fraction increases, which can be attributed to the contraction of the lattice constant. The BO values, however, remain nearly unchanged across alloy compositions, indicating that the bonding nature of $(Cd_{\text{int}} + As_{\text{Te}})^{+}$ and $(Cd_{\text{int}} + P_{\text{Te}})^{+}$ is largely insensitive to Se content. From these values, the Cd–Te and Cd–Se bonds are inferred to have roughly equal ionic and covalent character (approximately 50% each), while Cd–As and Cd–P bonds are predominantly covalent. This strong covalent component, combined with Coulomb interactions, accounts for the high binding energies observed in these complexes.

Table 4.4: Bond lengths (Å) and bond orders for nearest neighbors surrounding Cd interstitial in $(Cd_{int} + As_{Te})^{+}$ and $(Cd_{int} + P_{Te})^{+}$. Bond lengths are provided outside the brackets, while bond orders are denoted inside the brackets.

Defect Type	$(Cd_{int} + As_{Te})^{+}$			$(Cd_{int} + P_{Te})^{+}$		
Bond / Material	**Cd - Te**	**Cd - Se**	**Cd - As**	**Cd - Te**	**Cd - Se**	**Cd - P**
CdTe	2.84 (0.52)	-	2.57 (0.64)	2.83 (0.52)	-	2.49 (0.66)
$CdSe_{0.25}Te_{0.75}$	2.82 (0.52)	2.65 (0.52)	2.55 (0.65)	2.81 (0.52)	2.64 (0.52)	2.47 (0.67)
$CdSe_{0.50}Te_{0.50}$	2.80 (0.55)	2.64 (0.53)	2.54 (0.69)	2.79 (0.55)	2.63 (0.54)	2.46 (0.70)

4.2 Device Modeling of CdTe/CdSeTe Solar Cells

CdSeTe solar cells exhibit excellent reliability and a lower temperature coefficient than silicon solar cells [60, 90], making them promising candidates for large-scale photovoltaic deployment. However, improvements in open-circuit voltage (V_{oc}) have lagged behind other performance gains. For example, V_{oc} values near 900 mV were already achieved in 2013 for CdTe devices approaching 20% efficiency using Cu doping [20]. Yet, even with the recent record efficiency of 22.3% in As-doped CdSeTe devices, V_{oc} remains at a similar level (899 mV) [60]. This slow progress is notable given that several material and device parameters identified as necessary for 25%-efficient CdTe cells—such as carrier lifetime, doping concentration, and interface passivation [30]—have largely been achieved [2, 45, 44].

One of the key factors contributing to the V_{oc} deficiency in CdSeTe devices is believed to be potential fluctuations—both in the band gap and in the electrostatic potential [89, 91, 92]. Such fluctuations can enhance nonradiative carrier recombination, leading to V_{oc} losses on the order of 99–129 meV and reducing the overall device efficiency. Quantifying and understanding these effects are therefore critical for developing strategies to suppress recombination losses and push CdSeTe performance closer to its theoretical limits.

In this work, a comprehensive device model for CdSeTe solar cells is developed, integrating defect multilevel transitions with potential fluctuation effects. By combining first-principles calculations with device-level simulations, the model enables a detailed understanding of carrier dynamics, recombination mechanisms, and the origins of theV_{oc} deficiency. This integrated framework establishes a basis for devising targeted optimization strategies to enhance both the efficiency and stability of CdSeTe solar cells.[2]

4.2.1 Methods

4.2.1.1 Device Calibration

The device model is built in Sentaurus TCAD, according to the simplified device structure shown in Fig. 4.8. The layers consist of a 5μm CdSeTe/CdTe absorber, 100nm MgZnO layer as buffer and a 300nm SnO_2/i-SnO_2 bilayer. These layer structures are consistent with experimental settings in [109].

Band parameters of $CdTe_{1-x}Se_x$ is dependent on Se ratio x, which is shown in Eq. 4.1 and Eq. 4.2

$$\begin{aligned} E_g^{total} &= (1-x)E_g^{\mathrm{CdTe}} + xE_g^{\mathrm{CdSe}} \\ &\quad + bx(1-x)\ . \end{aligned} \tag{4.1}$$

[2]This section is adapted from our manuscript: Yijun Tong*, Xiaofeng Xiang* and Scott T. Dunham. Understanding Voltage Loss in CdSeTe Solar Cells: Integrating Defect Chemistry and Potential Fluctuations in Device Modeling (in preparation).

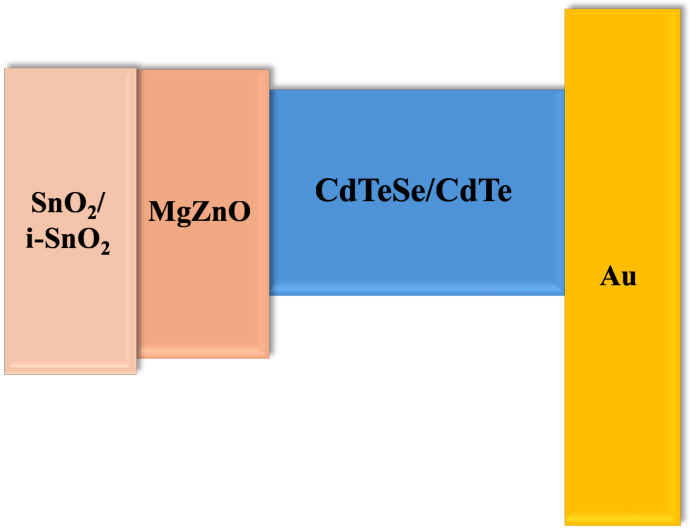

Figure 4.8: Device schematic of CdTeSe solar cells. CdTeSe layer ranges from 0 to 5.0 μm, but only a portion is shown in the schematic for concise illustration.

$$\begin{aligned}\chi = (1-x)\chi_{\mathrm{CdTe}} + x\chi_{\mathrm{CdSe}} \\ + cx(1-x)\ ,\end{aligned} \tag{4.2}$$

where bandgap of CdTe E_g^{CdTe} is 1.49 eV, bandgap of CdSe E_g^{CdSe} is 1.79 eV, electron affinity of CdTe χ_{CdTe} is 4.50 eV and electron affinity of CdSe χ_{CdSe} is 4.93 eV. Bowing parameter b for bandgap is 0.90 while bowing parameter c for electron affinity is -0.27.

Complex refractive index of CdSeTe is extracted from [28] for various Se compositions. Other critical parameters for each layer are shown in Table 4.5.

Table 4.5: Critical parameters in CdTeSe Device Model

	CdSeTe	i-SnO	SnO	MgZnO
Bandgap (eV)	Eq. 4.1	3.60	3.60	3.64
Carrier Density (cm^{-3})	Vary	1.0 x 10^{18}	5.0 x 10^{20}	1.0 x 10^{18}
Refractive Index	Data [28]	Data [19]	Data [19]	Data [71]
Effective mass e/h	0.095*(1-SST)+0.082*(SST)/0.84*(1-SST)+1.243*(SST)	0.25/1.0	0.25/1.0	0.2/0.7
Electron affinity	Eq. 4.2	4.70	4.80	0.2/0.7
Mobility e/h (cm^2/V s)	320/80	10/2.5	30/2.5	30/1.5
Lifetime e/h (ns)	SRH & Radiative Recombination	1.0	1.0	1.0

In this study, CdTe:Cu and CdSeTe:Cu are employed as baseline models for device calibration. The chemical potentials of Cu, Cd, Se, and Te are adjusted to reproduce the experimentally reported carrier densities and lifetimes. For the CdSeTe:Cu baseline model, the SST (Se/(Se+Te)) profile is extracted from [109], as shown in Fig. 4.9. Defect energetic and recombination parameters are taken from our previous work [96] and incorporated into the Sentaurus TCAD framework using the multilevel defect implementation method described in Section 2.2.2.2.

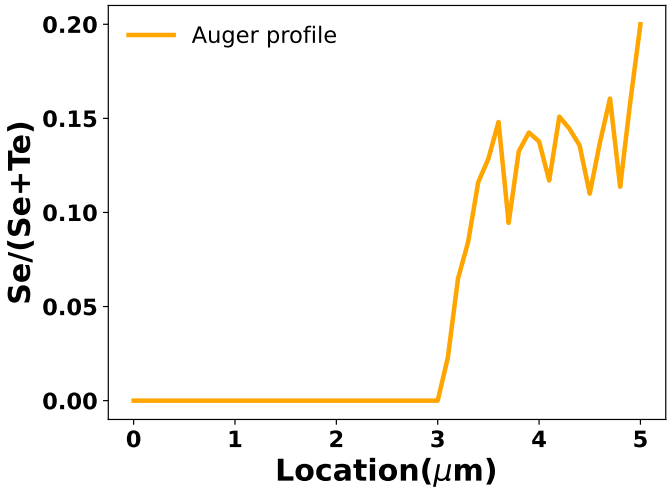

Figure 4.9: Se ratio profile of CdTeSe solar cells in [109].

Following the profile setup described above, the simulation models of both CdTe:Cu and CdSeTe:Cu are calibrated and validated against experimental measurements, as summarized in Table 4.6. The simulated device efficiency (η) and fill factor (FF) for both CdTe:Cu and CdSeTe:Cu exceed the corresponding experimental values. This discrepancy is likely attributable to series resistance effects, which are known to reduce both efficiency and fill factor in actual devices. In the present setup, however, the series resistance has not been explicitly matched to experimental conditions.

After establishing a reliable baseline model, the calibrated device profile is transferred

to CdSeTe:As. The resulting simulated device parameters are in agreement with those reported for state-of-the-art CdSeTe:As solar cells by First Solar [60].

Table 4.6: CdSeTe Solar cell device performance from experiment and simulation

	J_{sc} (mA)	V_{oc} (V)	η%	Fill Factor
Experiment data (CdTe:Cu), NREL(Ref. [109])	25.2	0.87	12.6	57.6
Experiment data (CdSeTe:Cu), NREL(Ref. [109])	28.5	0.82	15.1	64.9
Device Simulation Calibration (CdTe:Cu)	25.3	0.88	16.1	72.4
Device Simulation Calibration (CdSeTe:Cu)	28.7	0.81	18.5	79.6
Device Simulation (CdSeTe:As)	28.7	1.00	23.7	82.5
Device Simulation (CdSeTe:As, σ_{tot} 28meV)	28.7	0.91	21.0	80.8
Experiment data (CdSeTe:As), First Solar (Ref. [60])	30.9	0.92	22.1	78.3

4.2.1.2 Setup of Potential Fluctuations

Potential fluctuations arise from two main sources as shown in Fig 4.10: (1) band gap fluctuations caused by variations in alloy composition, strain, and stoichiometry, and (2) electrostatic fluctuations induced by charged defects located within grains, at grain boundaries, or at interfaces. Band gap fluctuations are optically active and can be detected through optical measurements, whereas electrostatic fluctuations are not optically sensitive [89]. However, both types of fluctuations influence electrical behavior and can be probed through electrical measurements. Notably, electrostatic fluctuations are injection-dependent due to screening effects from free charge carriers.

Local band gap variations appear as band tails in optical spectra [46, 64]. Different forms of band tails—exponential, Gaussian, and power-law[77]—have been reported across a wide range of materials, including II-VI, III-V, group IV, organic, and perovskite semiconductors. For CdSeTe, the band tail is most commonly described by an exponential form [46, 69]. The exponential band tail DOS can be expressed as [29]:

$$D(E) = \frac{N_t}{2\sigma} \exp(-\frac{|E - E_0|}{\sigma}) \tag{4.3}$$

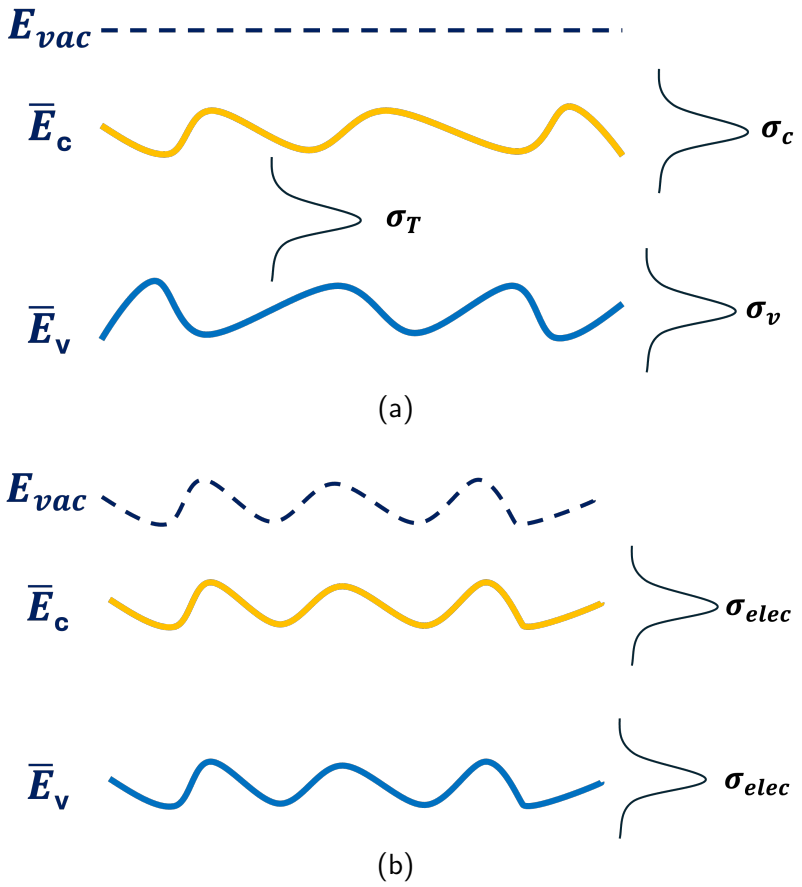

Figure 4.10: Two types of potential fluctuations are considered: (a) bandgap fluctuations and (b) electrostatic potential fluctuations. In case (a), the conduction band E_c and the valence band E_v edges fluctuate independently, resulting in spatial variations in both the band gap and electron affinity. These fluctuations are modeled using an exponential tail described by Eq. 4.3 characterized by σ_c and σ_v for the conduction and valence bands, respectively; collectively, these define the Urbach energy σ_u. The spatial distribution of defect transition levels is modeled by a Gaussian profile with standard deviation σ_T. In case (b), the band gap remains spatially uniform, but electrostatic fluctuations—arising from nonuniform charge distribution—are superimposed on the band diagram. In this work, we focus on electrostatic potential fluctuations induced by charged defects distributed within grains. The electrostatic fluctuation induced by spatial distribution of charged defects is described by σ_{elec}.

where N_t is the integral of the band tail DOS over the energy, E_0 denotes energy position of conduction band minimum (CBM) or valence band maximum (VBM). And σ is a characteristic energy width of the band tail distribution. Based on the band tail DOS of Eq. 4.3, the total electron density as a function of the electron quasi-Fermi level $E_{\mathrm{F,n}}$ and temperature T is computed as the following (a similar expression applies for holes):

$$\begin{aligned} n(E_{F,n},T) &= n_b(E_{F,n},T) + n_{bt}(E_{F,n},T) \\ n_{bt}(E_{F,n},T) &= \int_{-\infty}^{\infty} \frac{D(E)}{1+\exp(\frac{E+E_C-E_{F,n}}{kT})} \end{aligned} \tag{4.4}$$

where $n_b(E_{F,n},T)$ is the electron density computed using the DOS without the band tails, and $n_{bt}(E_{F,n},T)$ is the density of electrons that occupy the band tail DOS.

In optical measurement, Urbach energy σ_u is extracted by fitting the absorption spectrum to an exponential function. The resulting value reflects an average over the illuminated volume of the sample. Thus,

$$\sigma_u = \sqrt{\sigma_c^2 + \sigma_v^2} \tag{4.5}$$

In addition, due to charged defects, the CB and VB edges fluctuate with σ_{elec}. Total fluctuation can be expressed as:

$$\sigma_{tot} = \sqrt{\sigma_u^2 + \sigma_{elec}^2} \tag{4.6}$$

This expression assumes that composition-induced fluctuations (σ_{u}, e.g., from alloy disorder) and electrostatic fluctuations (σ_{elec}, e.g., from charged defects) are statistically independent. σ_{tot} is the value we should use in Eq. 4.3.

σ_{elec} can be estimated using following equation [79, 80, 74]:

$$\sigma_{elec} = \frac{e^2}{4\pi\varepsilon\varepsilon_0}(\frac{4\pi}{3})^{1/3}\frac{N_{A/D}^{2/3}}{p+\Delta p+\Delta n} \tag{4.7}$$

where e is the elementary charge, $\varepsilon\varepsilon_0$ is the static permittivity of the semiconductor, $N_{A/D}$

is total donor or acceptor concentration, p is the carrier density from net doping, Δp and Δn are photogenerated carrier densities. This equation describes electrostatic potential fluctuations arising from the random spatial distribution of concentrations of charged defects. However, it does not capture variations in defect formation energies and charge-transition levels caused by the local atomic environment, as demonstrated in our previous work [96, 97]. To account for this effect, the distribution of defect transition levels is represented by a Gaussian function with a standard deviation σ_T. Such variations can contribute to V_{oc} deficiency but do not add to σ_{tot}.

4.2.2 Results and Discussion

To investigate the impact of potential fluctuations on open-circuit voltage loss ΔV_{oc}, two contributing mechanisms are examined: (1) total disorder σ_{tot}, which includes both bandgap and electrostatic contributions, and (2) trap transition level fluctuations σ_{T} under a constant σ_{tot}.

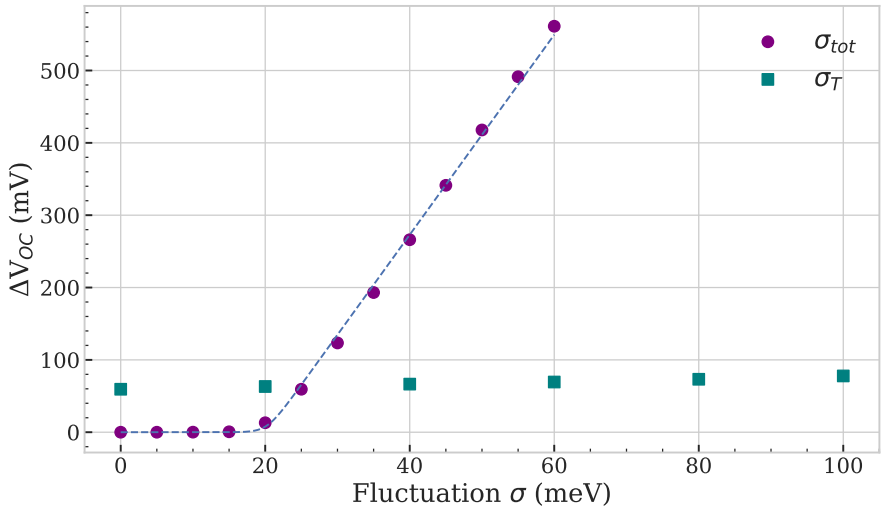

Figure 4.11: ΔV_{oc} versus σ_{tot} and σ_{T}. The dotted line represents a fitting curve based on the two-bandgap model [92]. For modeling the impact of trap transition level fluctuation, a constant σ_{tot} of 25 meV is used.

Figure 4.11 presents the simulated ΔV_{oc} as a function of fluctuation magnitude for both σ_{tot} and σ_T. The ΔV_{oc} associated with trap transition-level variation (green squares) remains nearly constant across the entire fluctuation range (0–100 meV). In contrast, potential fluctuations have a significant impact on ΔV_{oc}, as illustrated in Fig. 4.11. The relationship between ΔV_{oc} and σ_{tot} can be accurately described by the two-bandgap model given in Eq. 4.8 [92].

$$\Delta V_{oc} = \frac{kT}{q} \ln \left(r \exp \frac{m\sigma}{kT} + 1 - r \right) \tag{4.8}$$

In this model, the parameter r represents the ratio between subgap and above-gap absorbance, with a fitted value of 5.53×10^{-6}. The parameter $m\sigma$ characterizes the Stokes shift between absorption and luminescence. From our fitting results, As-doped CdSeTe samples with an Urbach energy of 23-26 meV are expected to exhibit a Stokes shift of approximately 0.32-0.37 eV. This predicted Stokes shift requires further experimental validation to confirm its accuracy.

Experimental data indicate that As-doped CdSeTe samples exhibit an Urbach energy in the range of 23–26 meV, with a corresponding ΔV_{oc} 99–129 mV[46]. However, in our simulation (Fig.4.11), the calculated ΔV_{oc} is approximately 60 meV. This discrepancy can be attributed to the fact that optical measurements are inherently insensitive to electrostatic fluctuations, as discussed earlier. The low activation of As in CdSeTe likely introduces additional electrostatic disorder near the bandgap edge, which is not captured by purely optical characterization.

To investigate the role of electrostatic fluctuations σ_{elec}, we analyzed their dependence on the arsenic (As) activation ratio, as shown in Fig. 4.12. In this simulation, a constant bandgap fluctuation (σ_{u}=25 meV) was assumed to isolate the impact of electrostatic effects. The value of σ_{elec} was varied according to the As activation ratio, following Eq. 4.7, which establishes a direct link between the total concentration of ionized defects and local electrostatic fluctuations. The simulation results reveal that both the total disorder-induced V_{oc} loss (blue curve) and the loss specifically attributed to electrostatic fluctuations (orange

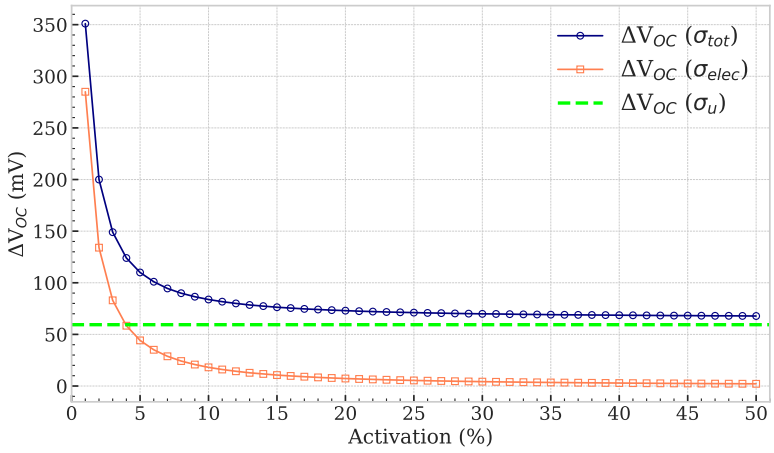

Figure 4.12: ΔV_{oc} versus As activation ratio. Blue dots indicate the ΔV_{oc} due to total disorder σ_{tot}, while orange dots correspond to the loss caused solely by electrostatic fluctuations σ_{elec} and green dashed line indicates the loss caused by bandgap fluctuation σ_{u}. Here, a constant σ_{u} of 25 meV is used. The value of σ_{elec} is varied with the As activation level according to Eq. 4.7. The injected carrier concentrations Δp and Δn are around 1×10^{17} cm^{-3} in space charge region under open circuit, and the background hole density p is kept at 1×10^{16} cm^{-3} regardless of activation ratio.

curve) decrease with increasing As activation. This reduction is primarily due to a decrease in compensating defects as the activation ratio increases. At low activation ratios (<4%), σ_{elec} contributes to more than 50% of the total V_{oc} loss. In contrast, at higher activation ratios, the contribution of σ_{elec} reduces and V_{oc} loss converges to the value determined by bandgap fluctuation. The green dashed line in Fig. 4.12 represents the constant contribution of σ_{u}, which remains unaffected by activation.

When the activation ratio of As ranges from 2% to 4%, the simulated ΔV_{oc} increases to approximately 110–150 mV, which is consistent with experimental observations. This suggests that the observed voltage loss is driven by a combination of bandgap fluctuation and electrostatic fluctuation (arising from low As activation).

State-of-the-art CdSeTe:As solar cells exhibit an activation ratio of roughly 2–3% [60], which falls within the region where σ_{elec} plays a critical role in determining ΔV_{oc}. This high-

lights the importance of improving As activation to reduce electrostatic disorder. Strategies such as passivating compensating defects or optimizing doping processes to enhance dopant activation are essential for further V_{oc} improvement. Moreover, reducing bandgap fluctuations is equally critical. This can be achieved by carefully controlling alloy composition, strain, and stoichiometry during the deposition process. Optimizing these parameters could potentially minimize bandgap disorder (σ_{u}), leading to improved V_{oc} and overall device performance. These findings corroborate our modeling approach and demonstrate that V_{oc} deficits in As-doped CdSeTe can be attributed to potential fluctuations. The strong correlation between the modeled and experimental data supports the hypothesis that low As activation introduces high electrostatic disorder, thereby reducing the open-circuit voltage. Further experimental studies are recommended to quantify the Stokes shift and verify its impact on V_{oc} loss.

Chapter 5

IN-DEPTH THEORETICAL INVESTIGATION OF SE VACANCIES IN CDSE

Cadmium selenide (CdSe) possesses a near-ideal bandgap of $E_g \approx 1.7$ eV, making it a strong candidate for the top junction in tandem photovoltaic devices. Despite this favorable bandgap, the performance of CdSe solar cells has remained below expectations. Experimental studies have attributed this deficiency primarily to extremely rapid (sub-nanosecond) minority-carrier trapping by deep defect states, which severely limits carrier lifetimes. The density of such defects in as-grown polycrystalline CdSe films has been measured to be in the range of (5–50) $\times 10^{17}$ cm^{-3}, a level high enough to dominate nonradiative Shockley–Read–Hall (SRH) recombination losses.

In this chapter, density functional theory (DFT) calculations are employed to identify and characterize the dominant defects responsible for these losses. Our results indicate that selenium vacancies (V_{Se}) are consistent with both the experimentally observed hole-trapping behavior and one of the sub-bandgap photoluminescence (PL) peaks. A configuration coordinate diagram (CCD) for V_{Se} is constructed to provide insight into experimental observations, with particular attention to the D1 PL emission feature.

The findings offer valuable guidance for mitigating carrier-trap-related losses. Specifically, reducing V_{Se} density through optimized growth conditions, targeted defect passivation, or controlled stoichiometry are suggested to improve device performance. The benefits are particularly pronounced when employing thin CdSe absorbers, which not only enhance carrier transport by reducing path length needed for carriers to reach the interfaces, but also limit SRH recombination losses.

Furthermore, CdSe exhibits near-single-crystal-like band-edge emission, owing to its uniform bandgap and minimal electrostatic potential fluctuations. This property is advan-

tageous for tandem applications, as it suppresses band tails in the top-junction absorber, thereby preventing undesirable spectral overlap and photon management complications for the bottom junction.[1]

5.1 Methods

Density functional theory (DFT) calculations were carried out using the Vienna ab initio simulation package (VASP) with the projector-augmented wave (PAW) method to describe the ion cores. The Perdew–Burke–Ernzerhof (PBE) exchange–correlation functional was employed, and spin polarization was included in both electronic calculations and structural relaxations for bulk cells and defect-containing supercells. The plane-wave kinetic energy cutoff was set to 520 eV. Electronic self-consistency and ionic relaxation were converged to 10^{-5} eV and 5 meV/Å, respectively. A simplified (rotationally invariant) Hubbard U correction was applied to Cd d orbitals ($U_{\text{eff}} = 12.2$ eV), yielding bandgap and lattice parameters in close agreement with experimental values for both CdSe and CdTe. Defect calculations were performed in a 300-atom supercell with single-Γ-point k-space sampling. Charged-cell corrections to defect formation energies were evaluated using the Freysoldt–Neugebauer–Van de Walle (FNV) scheme to account for spurious electrostatic interactions between localized charges and their periodic images. Configuration coordinate diagrams (CCDs) were constructed from linearly interpolated structures between two ground-state geometries corresponding to different defect charge states.

Benchmarking for CdSe began by applying the same effective Hubbard U value for Cd-d orbitals as used in CdTe and CdSeTe. Remarkably, this choice yielded bandgap and lattice constant values for both zinc blende and wurtzite CdSe that matched experimental results well, as shown in Table 5.1 [75]. This agreement across CdTe and CdSe can be attributed to their similar Cd–VI bonding characteristics, where both Te and Se are group VI elements and

[1]This chapter is adapted from our manuscript: Darius Kuciauskas, Taylor Hill, James R. Sites, Sachit Grover, Yijun Tong, and Scott T. Dunham. Increased Voltage in CdSe Solar Cells by Mitigation of Charge Carrier Trapping Due to Se Vacancies (under review).

exhibit comparable d–s coupling. The GGA+U approach lowers the Cd-4d bands, thereby strengthening this coupling. Using $U = 12.2$ eV thus provides a consistent correction for both materials, offering accuracy comparable to more expensive hybrid functional methods while maintaining significantly lower computational cost.

Table 5.1: Lattice constant, bandgap for CdTe and CdSe bbtained from GGA+U, HSE06 and experiments.

Method	**GGA+U**		**HSE06**		**Experiment [75]**	
	Bandgap (eV)	a_0 **(Å)**	**Bandgap (eV)**	a_0 **(Å)**	**Bandgap (eV)**	a_0 **(Å)**
CdTe (Zinc Blende)	1.50	6.46	1.50	6.58	1.50	6.48
CdSe (Zinc Blende)	1.72	5.95	-	-	1.71	5.98
CdSe (Wurtzite)	1.72	$a = b = 4.34$ $c = 7.08$	1.68	$a = b = 4.30$ $c = 7.01$	1.71	$a = b = 4.30$ $c = 7.02$

As will be discussed in subsequent sections, quantifying defect-induced radiative recombination is an essential component of our model. To determine the radiative emission coefficient, which provides a first-principles framework for evaluating radiative processes associated with point defects. [13]. Within the Born-Oppenheimer approximation and the Condon approximation [50], the luminescence intensity (number of photons per unit time, per unit energy, for a given photon energy $\hbar\omega$) is given by [81]

$$I(\hbar\omega) = \frac{e^2 n_r \omega \eta_{sp}}{3m^2 \epsilon_0 \pi c^3 \hbar} |p_{if}|^2 \sum_n |\langle \chi_{i0} | \chi_{fn} \rangle^2| \times \delta(E_{ZPL} - \hbar\omega_{fn} - \hbar\omega) \tag{5.1}$$

where n_r is the refraction index, $\hbar\omega_{fn}$ is the energy of final vibrational state, and η_{sp} is the spin selection factor. By integrating $I(\hbar\omega)$ over $\hbar\omega$, the total recombination rate can be achieved

$$r = \frac{e^2 n_r \omega \eta_{sp}}{3m^2 \epsilon_0 \pi c^3 \hbar^2} |p_{if}|^2 \langle \hbar\omega \rangle \tag{5.2}$$

in which

$$\langle \hbar\omega \rangle = \sum_n |\langle \chi_{i0} | \chi_{fn} \rangle^2| \times \delta(E_{ZPL} - \hbar\omega_{fn}) \tag{5.3}$$

is the average energy of emitted photons. For defects with large Huang-Rhys factor, in other words strong electron-phonon coupling, $\langle \hbar\omega \rangle$ coincides with the vertical optical transition

E_{opt}. The final radiative capture coefficient is

$$C = Vr \tag{5.4}$$

and V is the volume of supercell used in simulation.

In order to calculate the momentum matrix element $|p_{if}|$, the dipole matrix element is calculated from DFT and subsequently apply the commuting relationship from quantum mechanics

$$\langle i|p|f\rangle = \frac{m}{i\hbar}(E_n - E_m)\langle i|r|f\rangle \tag{5.5}$$

where the dipole matrix element is nothing but

$$d_{if} = -e\langle i|r|f\rangle \tag{5.6}$$

5.2 Results and Discussions

5.2.1 Experimental Results

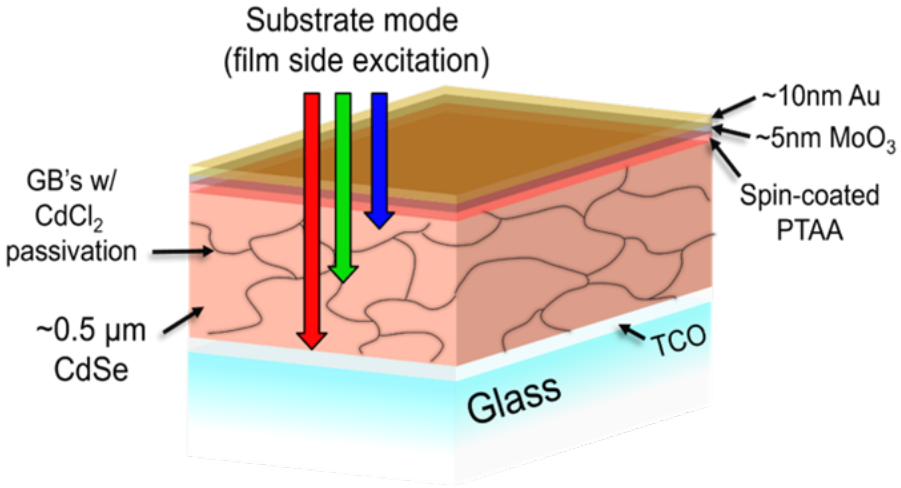

Figure 5.1: Illustration of the device configuration used in this study. TCO is transparent conductive oxide (SnO_2:F), PTAA is poly(triaryl) amine, GBs are grain boundaries.

Key experimental findings from our collaborators are summarized here to motivate the theoretical investigation.

Polycrystalline CdSe absorbers of two thicknesses were fabricated and incorporated into complete solar cell devices. When the absorber thickness was reduced from 1.2 μm (S1) to 0.5 μm (S2), the open-circuit voltage (V_{oc}) increased markedly from 752mV to 917mV, while the short-circuit current density (J_{sc}) remained essentially unchanged. This pronounced V_{oc} improvement suggests that carrier trapping is the primary loss mechanism in polycrystalline CdSe solar cells.

Photoluminescence (PL) spectra for both S1 and S2 were measured to gain further insight into the fabricated absorbers. Absorptance spectra, derived from the PL data using the Generalized Planck's Law, are shown in the inset of Fig. 5.2(a). The bandgap extracted from these absorptance spectra using the derivative method [42] is $E_{\mathrm{g}} = 1.71$eV. Additionally, low-temperature (4K) excitonic PL measurements [inset of Fig. 5.2(b)] confirm the presence of the wurtzite CdSe phase, as the excitonic PL signature differs from that expected for zinc blende CdSe [11].

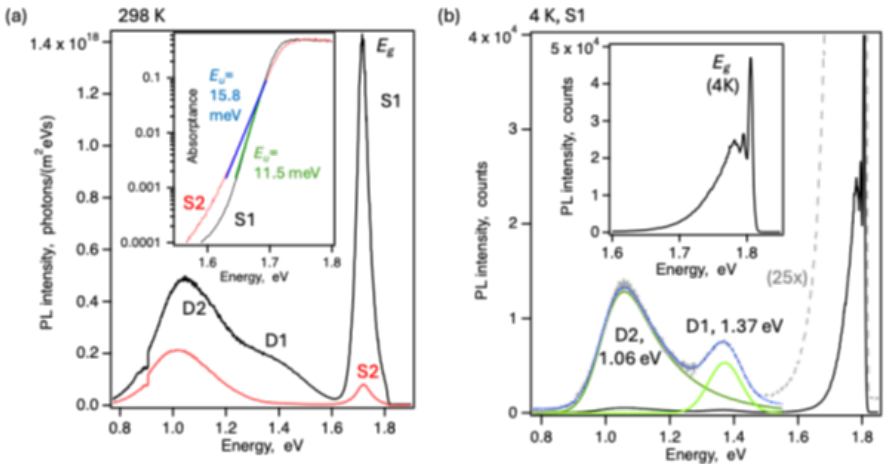

Figure 5.2: (a) Absolute PL emission spectra for S1 (black) and S2 (red) at 298 K. Inset shows absorptance spectra calculated from PL and fits to determine Urbach energies E_u. (b) PL emission at 4K for S1. The inset shows high energy (exciton) region.

Unlike most high-efficiency photovoltaic semiconductors, the CdSe samples exhibit pronounced sub-bandgap defect-related PL emissions. The full width at half maximum (FWHM) of the D2 defect peak remains nearly unchanged between room temperature and cryogenic conditions (258 meV at 298K vs. 213 meV at 4K), indicating that D2 likely corresponds to a mid-gap defect state. In contrast, the D1 defect peak shows a substantial narrowing at low temperature (366 meV at 298K vs. 119 meV at 4K), suggesting that D1 is associated with a shallower defect level.

The origins of the D1 and D2 emissions have been examined in prior spectroscopic studies. D1 emission has been reported in CdSe grown by molecular beam epitaxy (MBE) [27]—although the corresponding spectral range for D2 was not investigated—and in thermally evaporated CdSe films used for solar cell fabrication [4]. In earlier work, Brasil *et al.* constructed configuration coordinate diagrams and attributed D1 to selenium vacancies (V_{Se}) and D2 to oxygen-on-selenium defects (O_{Se}) [5].

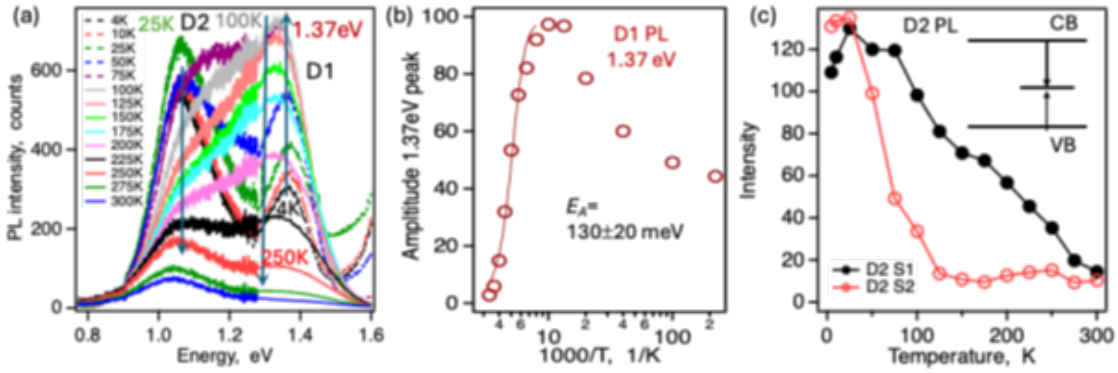

Figure 5.3: Defect D1 and D2 PL emission. (a) Temperature-dependence of defect emission bands for S1. (b) Analysis of D1 emission in graph (a) to determine activation energy E_A. (c) D2 emission temperature dependence for S1 and S2.

Figure 5.3(a) presents the temperature dependence of the D1 and D2 emissions for sample S1. The D1 emission exhibits a more complex behavior: between 4 K and 100 K, its photoluminescence (PL) amplitude increases by approximately a factor of 2.5, followed by thermal quenching above 100 K with an activation energy of 130 ± 15 meV (fit shown in

Fig. 5.3(b)). This trend closely matches the observations of Brasil *et al.* — who reported a D1 maximum at 1.35 eV and $E_A = 170$ meV — and assigned D1 to selenium vacancies (V_{Se}) [5]. To further evaluate this assignment, density functional theory (DFT) calculations are carried out in the next section, with a specific focus on the optical properties of V_{Se}, which were not addressed in earlier first-principles studies [101].

5.2.2 Computational Results

5.2.2.1 DFT Calculation Results

As discussed in the previous section, selenium vacancies are believed to be the dominant defects in CdSe, and have been suggested to account for some of the observed optoelectronic behavior [5]. In this study, three charge states of Se vacancies are calculated: neutral, +1 and +2. The thermodynamic transition level (above VBM) is calculated to be 1.6352 eV for (+2/+1) and 0.7463 eV for (+1/0), which indicates negative-U behavior. The V_{Se}^{+2} and V_{Se}^{+1} atomic structures are nearly identical and the associated charge distributions (from DDEC) indicate that V_{Se}^{+1} is essentially V_{Se}^{+2} with a delocalized bound electron. This is consistent with the +2/+1 ionization level locating just below conduction band minimum. The configuration coordinate diagram (CCD) between V_{Se}^{+1} and V_{Se}^{0} is shown in Fig. 5.4. V_{Se}^{0} shows a metastable state (noted as V_{Se}^{0*}) which shares the same structure as the ground state of $V_{Se}^{+1/+2}$ and has a second delocalized electron.

Based on the calculated ionization levels, the majority of selenium vacancies in undoped CdSe is in the stable V_{Se}^{0} structure under equilibrium conditions. During illumination, fast hole trapping induces a transient boost in the concentration of V_{Se}^{+1}, which can (1) transition into V_{Se}^{+2} by emitting an electron, (2) transition into V_{Se}^{0*} by capturing an electron, or (3) detrap the captured hole and relax back to V_{Se}^{0}. Process (3) is slow due to large a barrier and thus can generally be ignored. Process (1) is reversible and relatively rapid, allowing equilibration of the +1/+2 vacancy populations. Process (2) populates the metastable V_{Se}^{0*} state. There are two primary paths for relaxation of this metastable state: (1) photon emission

via recombination of free hole with bound electron and (2) transformation to stable neutral V_{Se}^{0} via structural deformation. The V_{Se}^{0*} radiative recombination pathway emits photons with energy calculated to be ∼1.3 eV, closely matching the experimental D1 PL value of ∼1.35 eV. The structural transformation from V_{Se}^{0*} to stable V_{Se}^{0}, which involves symmetric contraction of the surrounding Cd atoms toward the vacant site, requires overcoming an energy barrier and thus is temperature dependent. As temperature is increased, the thermal transition from metastable V_{Se}^{0*} to stable V_{Se}^{0} will depopulate V_{Se}^{0*} and thus cause the defect PL to decrease. The ∼150 meV barrier is likely to be the cause of D1 PL quenching above 100K and matches well with the experimentally observed activation energy of 130 meV (this work) and 170 meV [5].

The asymmetry between fast hole trapping from V_{Se}^{0} to V_{Se}^{+1} and slow hole detrapping from V_{Se}^{+1} to V_{Se}^{0} is also consistent with experimental results, as discussed above. Under illumination, most of the generated holes are trapped via formation of positively-charged Se vacancies, which slowly decay via electron capture by way of the neutral metastable state.

5.2.2.2 Continuum Simulation Results

In order to better quantify the model, continuum model based on the method introduced in section 2.2.2.1 is build in Sentaurus Sprocess, with a focus on processes related to Se vacancies. Specifically, following defect reactions are considered:

$$V_{Se}^{2+} + e^{-} \rightarrow V_{Se}^{+} \tag{5.7}$$

$$V_{Se}^{+} + h^{+} \rightarrow V_{Se}^{2+} \tag{5.8}$$

$$V_{Se}^{+} + e^{-} \rightarrow V_{Se}^{0*} \tag{5.9}$$

$$V_{Se}^{0*} \rightarrow V_{Se}^{0} \tag{5.10}$$

$$V_{Se}^{0} + h^{+} \rightarrow V_{Se}^{+} \tag{5.11}$$

$$V_{Se}^{0*} + h^{+} \rightarrow V_{Se}^{+} \; (radiative) \tag{5.12}$$

$$\phi \rightarrow e^{-} + h^{+} \tag{5.13}$$

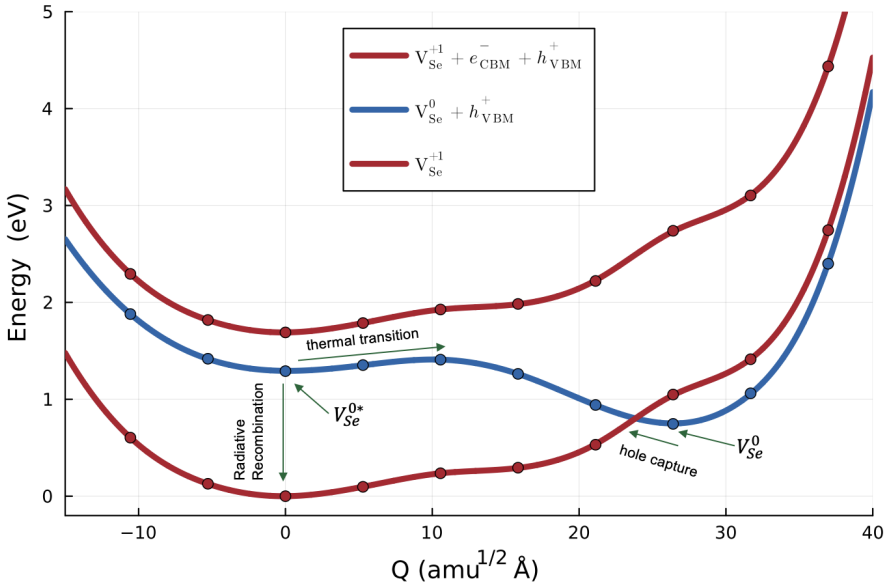

Figure 5.4: Calculated configuration coordinate diagram (CCD) between V_{Se}^{0} and V_{Se}^{+1}. Q represents the distance in configuration space projected linearly between the ground state structures of +1 (Q=0) and neutral (Q=27) Se vacancies. Arrows show the key processes manifested in PL and solar cell behavior as described in the text.

where equation 5.13 stands for the optical generation process. The corresponding reaction rates for each reaction are

$$R_1 = N_c v_{th} \sigma_1 (C^{2+} \frac{n}{N_c} - C^{+} \frac{1}{K_1}), \quad K_1 = \exp\left(\frac{E_g - E_t^{+2/+1}}{k_B T}\right) \tag{5.14}$$

$$R_2 = N_v v_{th} \sigma_2 (C^{+} \frac{p}{N_v} - C^{2+} \frac{1}{K_2}), \quad K_2 = \exp\left(\frac{E_t^{+2/+1}}{k_B T}\right) \tag{5.15}$$

$$R_3 = N_c v_{th} \sigma_3 (C^{+} \frac{n}{N_c} - C^{0*} \frac{1}{K_3}), \quad K_3 = \exp\left(\frac{E_g - E_t^{+1/0*}}{k_B T}\right) \tag{5.16}$$

$$R_4 = \nu \exp\left(-\frac{E_b}{k_B T}\right) \tag{5.17}$$

$$R_5 = N_v v_{th} \sigma_5 (C^{0} \frac{p}{N_v} - C^{+} \frac{1}{K_5}), \quad K_5 = \exp\left(\frac{E_t^{+1/0}}{k_B T}\right) \tag{5.18}$$

$$R_6 = K_6 p V_{Se}^{0*}, \quad K_6 = (5.77 \times 10^{-17})(V f \eta E_{opt} \frac{|p_{if}|^2}{2m}) \tag{5.19}$$

$$R_7 = G_L - R_r (np - n_i^2). \tag{5.20}$$

Table 5.2: Parameters used in continuum simulation

$v_{th}\sigma_1$ (cm^3s^{-1})	$1.26 * 10^{-13}$
$v_{th}\sigma_2$ (cm^3s^{-1})	$1.0 * 10^{-25}$
$v_{th}\sigma_3$ (cm^3s^{-1})	$9.15 * 10^{-21}$
$v_{th}\sigma_5$ (cm^3s^{-1})	$9.72 * 10^{-13}$
ν (Hz)	$1.0 * 10^9$
E_b (meV)	150
K_6 (cm^3s^{-1})	$1.08 * 10^{-10}$
R_r (cm^3s^{-1})	$5.47 * 10^{-10}$

In the above equations, R_4 denotes the transtion rate of metastable neutral V_{Se}^{0*} to stable neutral V_{Se}^{0} via a thermal barrier E_b. As expressed in equation 5.17, R_4 is proportional to the attempt frequency ν, and follows an Arrhenius dependence on E_b. R_6 represents the reaction rate for the radiative recombination process at $Q = 0$, in which the metastable neutral defect V_{Se}^{0*} captures a hole and subsequently emits a photon with an energy of 1.3 eV. The defect radiative recombination coefficient K_6 is calculated via the method introduced previously.

Continuum simulations were performed over a temperature range from 30 K to 300 K under illumination, with a carrier generation rate of $G_L = 10^{21}\ cm^{-3}/s$. As depicted in Fig. 5.5, the peak amplitude for the 1.3 eV defect emission increases from 30K to 100K, followed by a pronounced decrease as the temperature approaches 300K. This result is in close agreement with the experimental measurement shown in Fig. 5.3(b). This behavior also confirms our hypothesis that the thermal transition rate R_4 over the thermal barrier $\sim$150 meV competes with the radiative defect emission R_6 as temperature varies. The simulation result of time-resolved PL for D1 emission is shown in Fig. 5.6(b), where a transient time of $\sim$ 0.1 ns is evident. This result is consistent with experiment, as shown in Fig. 5.6(a). After 0.1 ns, the increase in 0* density due to injected carriers and the depletion of 0* density by radiative recombination as well as thermal transition is balanced, which leads to the stabilized PL intensity. In Fig. 5.6(a), the dip in D1 PL around 0.2 ns may be due to the onset of competition between D1 and D2 emission, in which the transient time

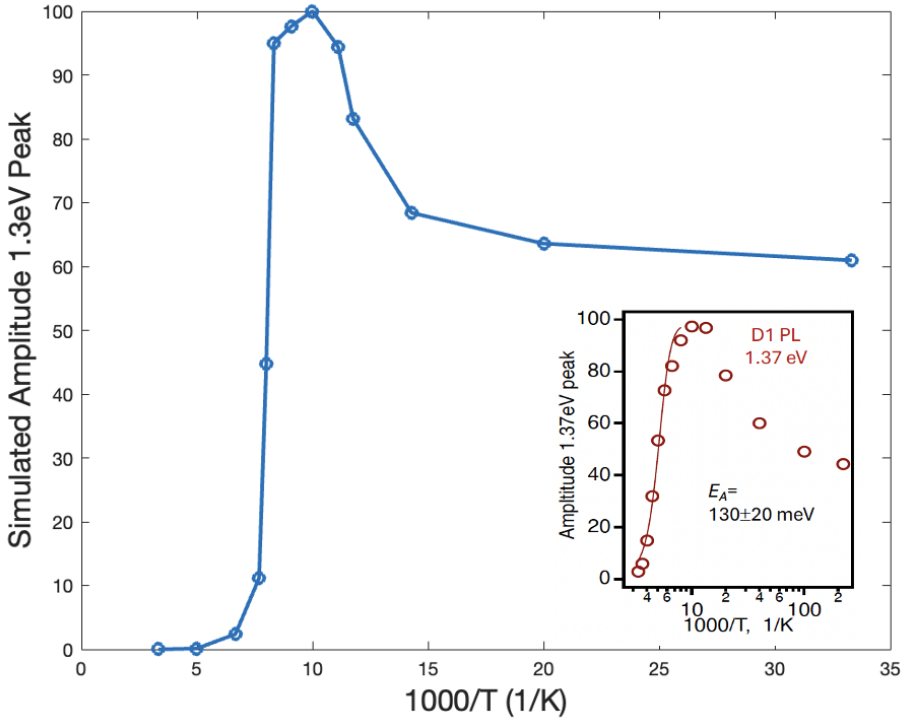

Figure 5.5: Simulated PL peak amplitude vs. temperature for the 1.3 eV defect emission. PL intensity is normalized to have a peak value of 100 to be consistent with reported experimental results. Inset is the experimental result from Fig. 5.3(b).

for D2 PL is around 0.2 ns.

The dependence of defect and carrier densities on the injection level is illustrated in Fig. 5.7. As the injection level increases, the rise in positively charged Se vacancy concentration is considerably more pronounced than that of free holes. For example, at an injection level of $10^{15}\ cm^{-1}/s$, the hole density is increased by about $10^{3}\ cm^{-3}$, while the densities of positively charged Se vancancies are increased by about $10^{15}\ cm^{-3}$. Thus, almost all the light-generated holes are trapped by Se vacancies. This behavior is also consistent with experimental findings [43], in which it is found that the open-circuit voltage (V_{oc}) is increased from 752 mV to 917 mV when the thickness of CdSe absorber is reduced from 1.2 μm to 0.5 μm. This is strong evidence of a trap-limited transport process. A simple model to explain this is the trap-induced mobility reduction

$$\mu_{trap} = \mu_h \left[1 + \frac{N_t}{N_v} \exp\left(\frac{E_t}{k_b T}\right)\right] \tag{5.21}$$

where N_t is the density of traps with transition level E_t from the band edge, and μ_h is the mobility without trapping. Using experimentally measured parameters, the diffusion length can be estimated as $L_d = \sqrt{D\tau_{SRH}}$, where $D = \frac{k_b T}{e}\mu$ is the diffusivity. Under the influence of carrier trapping, the diffusion length decreases substantially, from $L_d = 0.2 - 0.7\ \mu m$ to $L_{d,trapping} = 0.05 - 0.15\ \mu m$. This reduction represents a critical limitation for CdSe solar cells, leading to the improved device performance observed for thin CdSe absorbers.

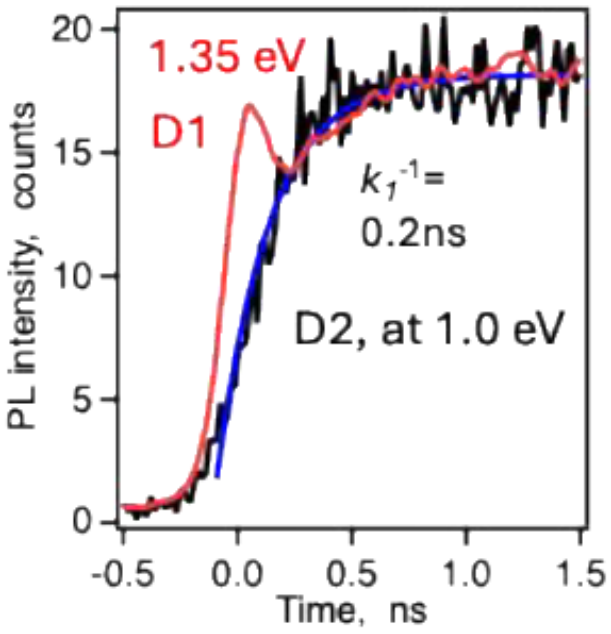

(a)

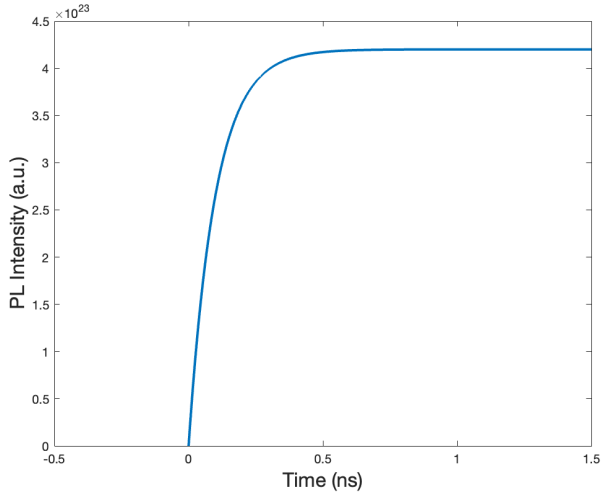

(b)

Figure 5.6: Time-resolved PL for D1 emission from (a) experiment and (b) continuum simulation.

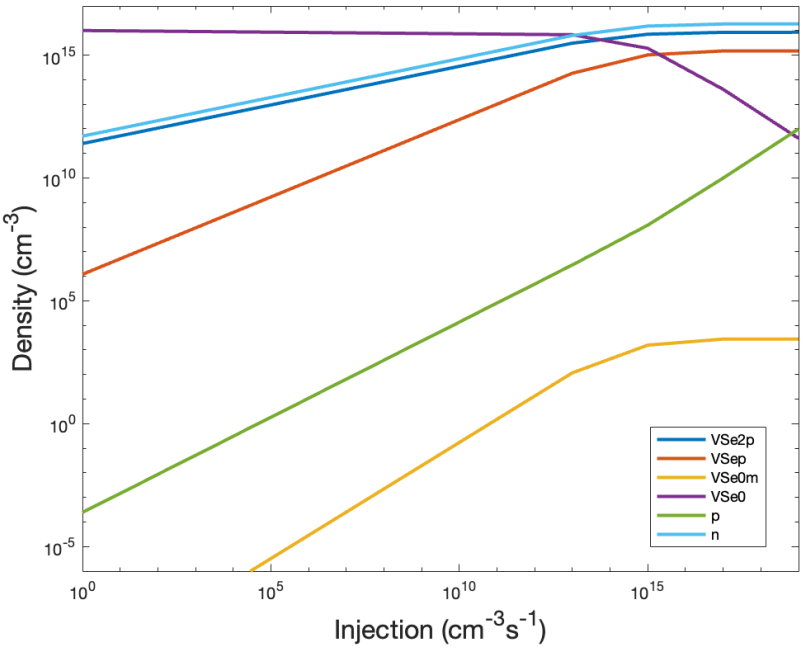

Figure 5.7: Simulated densities of defects and carriers with respect to injection level.

Chapter 6

CONCLUSION AND REFLECTION

This dissertation establishes a comprehensive multiscale modeling framework to elucidate the role of defects in photovoltaic materials and devices, integrating first-principles calculations with high-fidelity device simulations. Specifically, this work presents in-depth investigations of halide perovskites, cadmium telluride, and cadmium selenide systems. A central contribution of this work is the in-depth characterization of defect formation, carrier capture capabilities, and their influence on both radiative and nonradiative recombination processes under illuminated and dark conditions. In Chapter 2, the implementation of the GGA+U approach enables more reliable first-principles simulations and provides deeper insight into defect behavior in inorganic perovskites. The investigation of tin vacancies in the 3D–2D $PEA_{0.2}FA_{0.8}I_3$ further clarifies the mechanism of interface passivation achieved by the PEA network. Chapter 3 presents a detailed study of intrinsic and extrinsic defects in the CdTe/CdSeTe system, addressing long-standing questions in the field, including the identification of compensating defects that limit the effectiveness of group V dopants. The results obtained from DFT calculations are subsequently incorporated into the development of a comprehensive and carefully calibrated TCAD model for CdTe/CdSeTe solar cells. This model is then applied to investigate how various sources of fluctuation contribute to the observed V_{oc} deficiency. Finally, Chapter 4 examines the role of selenium vacancies in impacting the device performance of CdSe solar cells. A comprehensive detailed-balance model incorporating Se vacancies is developed and implemented within a continuum simulation framework to interpret several experimental observations, including trap-induced reductions in carrier mobility. With the help of novel methdologies developed in this thesis, these obtained fundamental understandings guide experimental efforts toward controlling

defect profiles, a capability that is essential for tailoring material properties and enhancing device performance.

It is hard to overstate how much I have learned during this PhD journey. One of the most significant areas of growth has been in understanding both the strengths and the limitations of computational modeling. I have come to realize that the true challenge lies in ensuring that the model accurately represents reality, with all its complexities and imperfections. Furthermore, I have learned that comparison with experimental results is not only necessary but also invaluable for validating the accuracy of theoretical models. This interplay between theory and experiment ensures that computational predictions remain grounded in physical reality, ultimately strengthening their reliability.

In future work, I plan to continue drawing on the benefits of theoretical modeling, maintaining a habit of approaching problems from a first-principles perspective to ensure that my analyses remain rigorous and grounded. More importantly, this way of thinking supports the analysis of complex, multifactor problems by helping to isolate the most critical influences on system behavior. Overall, although this PhD journey has been challenging, it has been an immensely rewarding and enjoyable experience from which I have benefited greatly.

BIBLIOGRAPHY

[1] Audrius Alkauskas, Qimin Yan, and Chris G Van de Walle. First-principles theory of nonradiative carrier capture via multiphonon emission. *Physical Review B*, 90(7):075202, 2014.

[2] Mahisha Amarasinghe, David Albin, Darius Kuciauskas, John Moseley, Craig L Perkins, and Wyatt K Metzger. Mechanisms for long carrier lifetime in Cd (Se) Te double heterostructures. *Applied Physics Letters*, 118(21), 2021.

[3] A Balcioglu, RK Ahrenkiel, and F Hasoon. Deep-level impurities in cdte/cds thin-film solar cells. *Journal of Applied Physics*, 88(12):7175–7178, 2000.

[4] Ebin Bastola, Adam B Phillips, Abasi Abudulium, Vlad Kornienko, Zulkifl Hussain, Manoj K Jamarkattel, Tamanna Mariam, Prabodika N Kalurachchi, Jared Friedl, Dipendra Pokhrel, et al. Cadmium selenide (cdse) as an active absorber layer for solar cells with voc approaching 750 mv. In *2023 IEEE 50th Photovoltaic Specialists Conference (PVSC)*, pages 1–6. IEEE, 2023.

[5] MJS Brasil, P Motisuke, F Decker, and JR Moro. Infrared photoluminescence at deep centres in polycrystalline cdse layers. *Journal of Physics C: Solid State Physics*, 21(16):3141, 1988.

[6] Thomas M Brenner, David A Egger, Leeor Kronik, Gary Hodes, and David Cahen. Hybrid organic—inorganic perovskites: low-cost semiconductors with intriguing charge-transport properties. *Nature Reviews Materials*, 1(1):1–16, 2016.

[7] A Castaldini, A Cavallini, B Fraboni, P Fernandez, and J Piqueras. Deep energy levels in cdte and cdznte. *Journal of applied physics*, 83(4):2121–2126, 1998.

[8] CWM Castleton and Susanne Mirbt. Finite-size scaling as a cure for supercell approximation errors in calculations of neutral native defects in inp. *Physical Review B—Condensed Matter and Materials Physics*, 70(19):195202, 2004.

[9] Yia-Chung Chang, RB James, and JW Davenport. Symmetrized-basis lasto calculations of defects in cdte and znte. *Physical Review B*, 73(3):035211, 2006.

[10] Intuon Chatratin, Baoying Dou, Su-Huai Wei, and Anderson Janotti. Doping limits of phosphorus, arsenic, and antimony in cdte. *The Journal of Physical Chemistry Letters*, 14(1):273–278, 2023.

[11] CH Chia, CT Yuan, JT Ku, SL Yang, Wu-Ching Chou, Jenh-Yih Juang, SY Hsieh, KC Chiu, JS Hsu, and SY Jeng. Temperature dependence of excitonic emission in cubic cdse thin film. *Journal of luminescence*, 128(1):123–128, 2008.

[12] Ioannis Deretzis, Emanuele Smecca, Giovanni Mannino, Antonino La Magna, Tsutomu Miyasaka, and Alessandra Alberti. Stability and degradation in hybrid perovskites: is the glass half-empty or half-full? *The Journal of Physical Chemistry Letters*, 9(11):3000–3007, 2018.

[13] Cyrus E Dreyer, Audrius Alkauskas, John L Lyons, and Chris G Van de Walle. Radiative capture rates at deep defects from electronic structure calculations. *Physical Review B*, 102(8):085305, 2020.

[14] Sergei L Dudarev, Gianluigi A Botton, Sergey Y Savrasov, CJ Humphreys, and Adrian P Sutton. Electron-energy-loss spectra and the structural stability of nickel oxide: An lsda+ u study. *Physical Review B*, 57(3):1505, 1998.

[15] Thomas AM Fiducia, Budhika G Mendis, Kexue Li, Chris RM Grovenor, Amit H Munshi, Kurt Barth, Walajabad S Sampath, Lewis D Wright, Ali Abbas, Jake W Bowers, et al. Understanding the role of selenium in defect passivation for highly efficient selenium-alloyed cadmium telluride solar cells. *Nature Energy*, 4(6):504–511, 2019.

[16] G Fonthal, L Tirado-Mejıa, JI Marın-Hurtado, H Ariza-Calderón, and JG Mendoza-Alvarez. Temperature dependence of the band gap energy of crystalline cdte. *Journal of Physics and Chemistry of Solids*, 61(4):579–583, 2000.

[17] Christoph Freysoldt, Blazej Grabowski, Tilmann Hickel, Jörg Neugebauer, Georg Kresse, Anderson Janotti, and Chris G Van de Walle. First-principles calculations for point defects in solids. *Reviews of modern physics*, 86(1):253, 2014.

[18] Christoph Freysoldt, Jörg Neugebauer, and Chris G Van de Walle. Electrostatic interactions between charged defects in supercells. *physica status solidi (b)*, 248(5):1067–1076, 2011.

[19] Omar Fuentes, Javier Goicoechea, Jesus M Corres, Ignacio Del Villar, Aritz Ozcariz, and Ignacio R Matias. Generation of lossy mode resonances with different nanocoatings deposited on coverslips. *Optics Express*, 28(1):288–301, 2020.

[20] M Gloeckler, I Sankin, and Z Zhao. CdTe solar cells at the threshold to 20% efficiency. *IEEE Journal of Photovoltaics*, 3(4):1389–1393, 2013.

[21] Stefan Grimme, Jens Antony, Stephan Ehrlich, and Helge Krieg. A consistent and accurate ab initio parametrization of density functional dispersion correction (dft-d) for the 94 elements h-pu. *The Journal of chemical physics*, 132(15), 2010.

[22] Graeme Henkelman, Blas P Uberuaga, and Hannes Jónsson. A climbing image nudged elastic band method for finding saddle points and minimum energy paths. *The Journal of chemical physics*, 113(22):9901–9904, 2000.

[23] Jan Herterich, Clemens Baretzky, Moritz Unmüssig, Clément Maheu, Nico Glissmann, Jeremias Gutekunst, Georgios Loukeris, Thomas Mayer, Markus Kohlstädt, Jan P Hofmann, et al. Toward understanding the short-circuit current loss in perovskite solar cells with 2d passivation layers. *Solar RRL*, 6(7):2200195, 2022.

[24] Pierre Hohenberg and Walter Kohn. Inhomogeneous electron gas. *Physical review*, 136(3B):B864, 1964.

[25] Xianyuan Jiang, Hansheng Li, Qilin Zhou, Qi Wei, Mingyang Wei, Luozhen Jiang, Zhen Wang, Zijian Peng, Fei Wang, Zihao Zang, et al. One-step synthesis of sni2·(dmso) x adducts for high-performance tin perovskite solar cells. *Journal of the American Chemical Society*, 143(29):10970–10976, 2021.

[26] Robert O Jones. Density functional theory: Its origins, rise to prominence, and future. *Reviews of modern physics*, 87(3):897–923, 2015.

[27] Z Ju, X Qi, S Schaefer, MR McCartney, DJ Smith, AVG Chizmeshya, T McCarthy, A McMinn, S Grover, and Y-H Zhang. Cdse with mixed zincblende and wurtzite phases grown on lattice-matched inas substrates using molecular beam epitaxy. *IEEE Journal of Photovoltaics*, 14(5):752–757, 2024.

[28] Maxwell M Junda, Corey R Grice, Prakash Koirala, Robert W Collins, Yanfa Yan, and Nikolas J Podraza. Optical properties of $CdSe_{1-x}S_x$ and $CdSe_{1-x}Te_x$ alloys and their application for cdte photovoltaics. In *2017 IEEE 44th Photovoltaic Specialist Conference (PVSC)*, pages 3426–3429. IEEE, 2017.

[29] Evan O Kane. Thomas-fermi approach to impure semiconductor band structure. *Physical Review*, 131(1):79, 1963.

[30] Ana Kanevce, Matthew O Reese, TM Barnes, SA Jensen, and WK Metzger. The roles of carrier concentration and interface, bulk, and grain-boundary recombination for 25% efficient CdTe solar cells. *Journal of Applied Physics*, 121(21), 2017.

[31] Seán R Kavanagh, Aron Walsh, and David O Scanlon. Rapid recombination by cadmium vacancies in cdte. *ACS energy letters*, 6(4):1392–1398, 2021.

[32] Gi-Hwan Kim and Dong Suk Kim. Development of perovskite solar cells with >25% conversion efficiency. *Joule*, 5(5):1033–1035, 2021.

[33] Walter Kohn and Lu Jeu Sham. Self-consistent equations including exchange and correlation effects. *Physical review*, 140(4A):A1133, 1965.

[34] Hannu-Pekka Komsa, Tapio T Rantala, and Alfredo Pasquarello. Finite-size supercell correction schemes for charged defect calculations. *Physical Review B—Condensed Matter and Materials Physics*, 86(4):045112, 2012.

[35] D Krasikov and I Sankin. Beyond thermodynamic defect models: A kinetic simulation of arsenic activation in cdte. *Physical Review Materials*, 2(10):103803, 2018.

[36] Dmitry Krasikov. Selenium lowers bulk recombination. *Nature Energy*, 4(6):442–443, 2019.

[37] Dmitry Krasikov, Da Guo, Samuel Demtsu, and Igor Sankin. Comparative study of as and cu doping stability in cdsete absorbers. *Solar Energy Materials and Solar Cells*, 224:111012, 2021.

[38] Dmitry Krasikov and Igor Sankin. Defect interactions and the role of complexes in the cdte solar cell absorber. *Journal of Materials Chemistry A*, 5(7):3503–3513, 2017.

[39] DN Krasikov, AV Scherbinin, AA Knizhnik, AN Vasiliev, BV Potapkin, and TJ Sommerer. Theoretical analysis of non-radiative multiphonon recombination activity of intrinsic defects in cdte. *Journal of Applied Physics*, 119(8), 2016.

[40] Georg Kresse and Jürgen Furthmüller. Efficient iterative schemes for ab initio total-energy calculations using a plane-wave basis set. *Physical review B*, 54(16):11169, 1996.

[41] Georg Kresse and Jürgen Hafner. Ab initio molecular dynamics for liquid metals. *Physical review B*, 47(1):558, 1993.

[42] Lisa Krückemeier, Uwe Rau, Martin Stolterfoht, and Thomas Kirchartz. How to report record open-circuit voltages in lead-halide perovskite solar cells. *Advanced energy materials*, 10(1):1902573, 2020.

[43] Darius Kuciauskas, Taylor Hill, James R. Sites, Sachit Grover, Yijun Tong, and Scott Dunham. Increased voltage in cdse solar cells by mitigation of charge carrier trapping due to se vacancies. Unpublished manuscript, 2025.

[44] Darius Kuciauskas, Jason M Kephart, John Moseley, Wyatt K Metzger, Walajabad S Sampath, and Pat Dippo. Recombination velocity less than 100 cm/s at polycrystalline Al2O3/CdSeTe interfaces. *Applied Physics Letters*, 112(26), 2018.

[45] Darius Kuciauskas, Siming Li, John Moseley, David Albin, Chungho Lee, Arthur Louis Onno, and Zachary Charles Holman. Voltage loss comparison in CdSe/CdTe solar cells and polycrystalline CdSeTe heterostructures. *IEEE Journal of Photovoltaics*, 12(1):6–10, 2021.

[46] Darius Kuciauskas, Marco Nardone, Alexandra Bothwell, David Albin, Carey Reich, Chungho Lee, and Eric Colegrove. Why increased cdsete charge carrier lifetimes and radiative efficiencies did not result in voltage boost for CdTe solar cells. *Advanced Energy Materials*, 13(35):2301784, 2023.

[47] Yu Kumagai. Finite-size corrections to defect energetics along one-dimensional configuration coordinate. *Physical Review B*, 107(22):L220101, 2023.

[48] Yu Kumagai and Fumiyasu Oba. Electrostatics-based finite-size corrections for first-principles point defect calculations. *Physical Review B*, 89(19):195205, 2014.

[49] Luis Lanzetta, Thomas Webb, Nourdine Zibouche, Xinxing Liang, Dong Ding, Ganghong Min, Robert JE Westbrook, Benedetta Gaggio, Thomas J Macdonald, M Saiful Islam, et al. Degradation mechanism of hybrid tin-based perovskite solar cells and the critical role of tin (iv) iodide. *Nature communications*, 12(1):2853, 2021.

[50] Melvin Lax. The franck-condon principle and its application to crystals. *The Journal of chemical physics*, 20(11):1752–1760, 1952.

[51] Jun Hee Lee, Kris T Delaney, Eric Bousquet, Nicola A Spaldin, and Karin M Rabe. Strong coupling of jahn-teller distortion to oxygen-octahedron rotation and functional properties in epitaxially strained orthorhombic lamno 3. *Physical Review B—Condensed Matter and Materials Physics*, 88(17):174426, 2013.

[52] Kanghua Li, Xuke Yang, Yue Lu, Jiayou Xue, Shuaicheng Lu, Jiajia Zheng, Chao Chen, and Jiang Tang. Fabrication and optimization of cdse solar cells for possible top cell of silicon-based tandem devices. *Advanced Energy Materials*, 12(26):2200725, 2022.

[53] AI Liechtenstein, Vladimir I Anisimov, and Jan Zaanen. Density-functional theory and strong interactions: Orbital ordering in mott-hubbard insulators. *Physical Review B*, 52(8):R5467, 1995.

[54] Nidia Gabaldon Limas and Thomas A Manz. Introducing ddec6 atomic population analysis: part 2. computed results for a wide range of periodic and nonperiodic materials. *RSC advances*, 6(51):45727–45747, 2016.

[55] Kebin Lin, Jun Xing, Li Na Quan, F Pelayo García de Arquer, Xiwen Gong, Jianxun Lu, Liqiang Xie, Weijie Zhao, Di Zhang, Chuanzhong Yan, et al. Perovskite light-emitting diodes with external quantum efficiency exceeding 20 per cent. *Nature*, 562(7726):245–248, 2018.

[56] Ao Liu, Huihui Zhu, Sai Bai, Youjin Reo, Taoyu Zou, Myung-Gil Kim, and Yong-Young Noh. High-performance inorganic metal halide perovskite transistors. *Nature Electronics*, 5(2):78–83, 2022.

[57] Joseph J Loferski. Theoretical considerations governing the choice of the optimum semiconductor for photovoltaic solar energy conversion. *Journal of Applied Physics*, 27(7):777–784, 1956.

[58] Jie Ma, Darius Kuciauskas, David Albin, Raghu Bhattacharya, Matthew Reese, Teresa Barnes, Jian V Li, Timothy Gessert, and Su-Huai Wei. Dependence of the minority-carrier lifetime on the stoichiometry of cdte using time-resolved photoluminescence and first-principles calculations. *Physical review letters*, 111(6):067402, 2013.

[59] Jie Ma, Jihui Yang, Su-Huai Wei, and Juarez LF Da Silva. Correlation between the electronic structures and diffusion paths of interstitial defects in semiconductors: The case of cdte. *Physical Review B*, 90(15):155208, 2014.

[60] R Mallick, X Li, C Reich, X Shan, W Zhang, T Nagle, L Bok, E Bicakci, N Rosenblatt, D Modi, et al. Arsenic-doped cdsete solar cells achieve world record 22.3% efficiency. *IEEE Journal of Photovoltaics*, 2023.

[61] Thomas A Manz and David S Sholl. Improved atoms-in-molecule charge partitioning functional for simultaneously reproducing the electrostatic potential and chemical states in periodic and nonperiodic materials. *Journal of chemical theory and computation*, 8(8):2844–2867, 2012.

[62] W. K. Metzger, S. Grover, D. Lu, E. Colegrove, J. Moseley, C. L. Perkins, X. Li, R. Mallick, W. Zhang, R. Malik, J. Kephart, C.-S. Jiang, D. Kuciauskas, D. S. Albin, M. M. Al-Jassim, G. Xiong, and M. Gloeckler. Exceeding 20% efficiency with in situ group v doping in polycrystalline cdte solar cells. *Nature Energy*, 4:837–845, 2019.

[63] Chen Ming, Han Wang, Damien West, Shengbai Zhang, and Yi-Yang Sun. Defect tolerance in cspbi 3: reconstruction of the potential energy landscape and band degeneracy in spin–orbit coupling. *Journal of Materials Chemistry A*, 10(6):3018–3024, 2022.

[64] John Moseley, Sachit Grover, Dingyuan Lu, Gang Xiong, Harvey L. Guthrey, Mowafak M. Al-Jassim, and Wyatt K. Metzger. Impact of dopant-induced optoelectronic tails on open-circuit voltage in arsenic-doped cd(se)te solar cells. *Journal of Applied Physics*, 128(10):103105, 09 2020.

[65] Amit H Munshi, Jason M Kephart, Ali Abbas, Adam Danielson, Guillaume Glinas, Jean-Nicolas Beaudry, Kurt L Barth, John M Walls, and Walajabad S Sampath. Effect of cdcl2 passivation treatment on microstructure and performance of cdsete/cdte thin-film photovoltaic devices. *Solar Energy Materials and Solar Cells*, 186:259–265, 2018.

[66] Daniel Mutter and Scott T Dunham. Calculation of defect concentrations and phase stability in Cu_2ZnSnS_4 and $Cu_2ZnSnSe_4$ from stoichiometry. *IEEE Journal of Photovoltaics*, 5(4):1188–1196, 2015.

[67] Akira Nagaoka, Kensuke Nishioka, Kenji Yoshino, Ryoji Katsube, Yoshitaro Nose, Taizo Masuda, and Michael A Scarpulla. Comparison of sb, as, and p doping in cd-rich cdte single crystals: Doping properties, persistent photoconductivity, and long-term stability. *Applied Physics Letters*, 116(13), 2020.

[68] Fumiyasu Oba, Atsushi Togo, Isao Tanaka, Joachim Paier, and Georg Kresse. Defect energetics in zno: A hybrid hartree-fock density functional study. *Physical Review B*, 77(24):245202, 2008.

[69] Arthur Onno, Carey Reich, Siming Li, Adam Danielson, William Weigand, Alexandra Bothwell, Sachit Grover, Jeff Bailey, Gang Xiong, Darius Kuciauskas, et al. Understanding what limits the voltage of polycrystalline CdSeTe solar cells. *Nature Energy*, 7(5):400–408, 2022.

[70] Walter Orellana, Eduardo Menéndez-Proupin, and Mauricio A Flores. Self-compensation in chlorine-doped cdte. *Scientific reports*, 9(1):9194, 2019.

[71] Zayani Jaafar Othman and Adel Matoussi. Morphological and optical studies of zinc oxide doped mgo. *Journal of Alloys and Compounds*, 671:366–371, 2016.

[72] Jie Pan, Wyatt K Metzger, and Stephan Lany. Spin-orbit coupling effects on predicting defect properties with hybrid functionals: A case study in cdte. *Physical Review B*, 98(5):054108, 2018.

[73] John P Perdew, Adrienn Ruzsinszky, Gábor I Csonka, Oleg A Vydrov, Gustavo E Scuseria, Lucian A Constantin, Xiaolan Zhou, and Kieron Burke. Restoring the density-gradient expansion for exchange in solids and surfaces. *Physical review letters*, 100(13):136406, 2008.

[74] Germain Rey, G Larramona, S Bourdais, C Choné, B Delatouche, A Jacob, G Dennler, and Susanne Siebentritt. On the origin of band-tails in kesterite. *Solar Energy Materials and Solar Cells*, 179:142–151, 2018.

[75] Ulrich Rössler. New data and updates for ii-vi compounds. *Landolt Börnstein*, 44, 2009.

[76] Chih-Tang Sah and William Shockley. Electron-hole recombination statistics in semiconductors through flaws with many charge conditions. *Physical Review*, 109(4):1103, 1958.

[77] Maria Saladina, Christopher Wöpke, Clemens Göhler, Ivan Ramirez, Olga Gerdes, Chao Liu, Ning Li, Thomas Heumüller, Christoph J Brabec, Karsten Walzer, et al. Power-law density of states in organic solar cells revealed by the open-circuit voltage dependence of the ideality factor. *Physical review letters*, 130(23):236403, 2023.

[78] Andreas Schenk and Ulrich Krumbein. Coupled defect-level recombination: Theory and application to anomalous diode characteristics. *Journal of applied physics*, 78(5):3185–3192, 1995.

[79] Boris Isaakovich Shklovskii and Alex L Efros. *Electronic properties of doped semiconductors*, volume 45. Springer Science & Business Media, 2013.

[80] Susanne Siebentritt, Niklas Papathanasiou, and M Ch Lux-Steiner. Potential fluctuations in compensated chalcopyrites. *Physica B: Condensed Matter*, 376:831–833, 2006.

[81] Arthur Marshall Stoneham. *Theory of defects in solids: electronic structure of defects in insulators and semiconductors*. Oxford University Press, 2001.

[82] Synopsys Inc. Sentaurus device user guide. Version K-2023.12, Synopsys, Inc., Mountain View, 2023.

[83] Yijun Tong, Xiaofeng Xiang, and Scott Dunham. Interstitals as non-radiative recombination centers for all-inorganic halide perovskites. *Computational Materials Science*, 246:113384, 2025.

[84] Antonella Treglia, Francesco Ambrosio, Samuele Martani, Giulia Folpini, Alex J Barker, Munirah D Albaqami, Filippo De Angelis, Isabella Poli, and Annamaria Petrozza. Effect of electronic doping and traps on carrier dynamics in tin halide perovskites. *Materials Horizons*, 9(6):1763–1773, 2022.

[85] CC Vidyasagar, Blanca M Muñoz Flores, and Víctor M Jiménez Pérez. Recent advances in synthesis and properties of hybrid halide perovskites for photovoltaics. *Nano-Micro Letters*, 10:1–34, 2018.

[86] Haiyan Wang, Yu Sun, Jin Chen, Fengchao Wang, Ruiyi Han, Canyun Zhang, Jinfang Kong, Lan Li, and Jing Yang. A review of perovskite-based photodetectors and their applications. *Nanomaterials*, 12(24):4390, 2022.

[87] Jing Wang, Jie Zhang, Yingzhi Zhou, Hongbin Liu, Qifan Xue, Xiaosong Li, Chu-Chen Chueh, Hin-Lap Yip, Zonglong Zhu, and Alex KY Jen. Highly efficient all-inorganic perovskite solar cells with suppressed non-radiative recombination by a lewis base. *Nature communications*, 11(1):177, 2020.

[88] Su-Huai Wei and SB Zhang. Chemical trends of defect formation and doping limit in ii-vi semiconductors: The case of cdte. *Physical Review B*, 66(15):155211, 2002.

[89] Jürgen H Werner, Julian Mattheis, and Uwe Rau. Efficiency limitations of polycrystalline thin film solar cells: case of Cu(In, Ga)Se2. *Thin Solid Films*, 480:399–409, 2005.

[90] Hope M Wikoff, Samantha B Reese, and Matthew O Reese. Embodied energy and carbon from the manufacture of cadmium telluride and silicon photovoltaics. *Joule*, 6(7):1710–1725, 2022.

[91] Max Hilaire Wolter, Romain Carron, Enrico Avancini, Benjamin Bissig, Thomas Paul Weiss, Shiro Nishiwaki, Thomas Feurer, Stephan Buecheler, Philip Jackson, Wolfram Witte, et al. How band tail recombination influences the open-circuit voltage of solar cells. *Progress in Photovoltaics: Research and Applications*, 30(7):702–712, 2022.

[92] Joeson Wong, Stefan T Omelchenko, and Harry A Atwater. Impact of semiconductor band tails and band filling on photovoltaic efficiency limits. *ACS Energy Letters*, 6(1):52–57, 2020.

[93] Xiaowei Wu, Han Zhang, Biao Zeng, Chen Ming, and Yiyang Sun. Comparison of hybrid functionals hse and pbe0 in calculating the defect properties of cspbi3. *Journal of Inorganic Materials*, 38(9), 2023.

[94] Yelong Wu, Guangde Chen, Youzhang Zhu, Wan-Jian Yin, Yanfa Yan, Mowafak Al-Jassim, and Stephen J Pennycook. Lda+ u/gga+ u calculations of structural and electronic properties of cdte: Dependence on the effective u parameter. *Computational Materials Science*, 98:18–23, 2015.

[95] Sisi Xiang, Weiping Li, Ya Wei, Jiaming Liu, Huicong Liu, Liqun Zhu, Shihe Yang, and Haining Chen. Natrium doping pushes the efficiency of carbon-based cspbi3 perovskite solar cells to 10.7%. *Iscience*, 15:156–164, 2019.

[96] Xiaofeng Xiang, Aaron Gehrke, Yijun Tong, and Scott T Dunham. Multiscale modeling and optimization of group v doping and compensation in $CdSe_xTe_{1-x}$. *ACS Applied Energy Materials*, 2025.

[97] Xiaofeng Xiang, Yijun Tong, Aaron Gehrke, and Scott Dunham. Point defects in cdte and cdtese alloy: a first principles investigation with dft+u. *arXiv*, 04 2024.

[98] Hongyao Xie, Shiqiang Hao, Jinke Bao, Tyler J Slade, G Jeffrey Snyder, Christopher Wolverton, and Mercouri G Kanatzidis. All-inorganic halide perovskites as potential thermoelectric materials: dynamic cation off-centering induces ultralow thermal conductivity. *Journal of the American Chemical Society*, 142(20):9553–9563, 2020.

[99] Haibo Xue, Geert Brocks, and Shuxia Tao. First-principles calculations of defects in metal halide perovskites: A performance comparison of density functionals. *Physical Review Materials*, 5(12):125408, 2021.

[100] Haibo Xue, José Manuel Vicent-Luna, Shuxia Tao, and Geert Brocks. Compound defects in halide perovskites: A first-principles study of cspbi3. *The Journal of Physical Chemistry C*, 127(2):1189–1197, 2023.

[101] Jiayou Xue, Xuke Yang, Xiaoqing Bao, Liuchong Fu, Sen Li, Menglin Huang, Jun Wang, Haisheng Song, Shiyou Chen, Chao Chen, et al. Improved carrier lifetimes of cdse thin film via te doping for photovoltaic application. *ACS Applied Materials & Interfaces*, 15(14):17858–17866, 2023.

[102] Ji-Hui Yang, Ji-Sang Park, Joongoo Kang, Wyatt Metzger, Teresa Barnes, and Su-Huai Wei. Tuning the fermi level beyond the equilibrium doping limit through quenching: The case of cdte. *Physical Review B*, 90(24):245202, 2014.

[103] Ji-Hui Yang, Wan-Jian Yin, Ji-Sang Park, James Burst, Wyatt K Metzger, Tim Gessert, Teresa Barnes, and Su-Huai Wei. Enhanced p-type dopability of p and as in cdte using non-equilibrium thermal processing. *Journal of Applied Physics*, 118(2):025102, 2015.

[104] Ji-Hui Yang, Wan-Jian Yin, Ji-Sang Park, Jie Ma, and Su-Huai Wei. Review on first-principles study of defect properties of cdte as a solar cell absorber. *Semiconductor Science and Technology*, 31(8):083002, 2016.

[105] Jiajia Zhang and Yu Zhong. Origins of p-doping and nonradiative recombination in cssni3. *Angewandte Chemie*, 134(44):e202212002, 2022.

[106] Xie Zhang, Mark E Turiansky, Jimmy-Xuan Shen, and Chris G Van de Walle. Iodine interstitials as a cause of nonradiative recombination in hybrid perovskites. *Physical Review B*, 101(14):140101, 2020.

[107] Xie Zhang, Mark E Turiansky, Jimmy-Xuan Shen, and Chris G Van de Walle. Defect tolerance in halide perovskites: A first-principles perspective. *Journal of Applied Physics*, 131(9), 2022.

[108] Xie Zhang, Mark E Turiansky, and Chris G Van de Walle. Correctly assessing defect tolerance in halide perovskites. *The Journal of Physical Chemistry C*, 124(11):6022–6027, 2020.

[109] Xin Zheng, Darius Kuciauskas, John Moseley, E Colegrove, David S Albin, H Moutinho, Joel N Duenow, Tursunjan Ablekim, Steven P Harvey, A Ferguson, et al. Recombination and bandgap engineering in CdSeTe/CdTe solar cells. *Apl Materials*, 7(7), 2019.